Computational methods applied to Superconductivity and Magnetism

By

Alan Kyker
B.S. (University of Tennessee at Knoxville) 1988

DISSERTATION

Submitted in partial satisfaction of the requirements for the degree of

Doctor of Philosophy

in

Physics

in the

OFFICE OF GRADUATE STUDIES

of the

UNIVERSITY OF CALIFORNIA
DAVIS

Approved:

Committee in Charge

2006

To Dale

Abstract

Computational methods applied to Superconductivity and Magnetism

by

Alan Kyker

Superconductivity and magnetism are two phenomena where the microscope quantum world manifests macroscopic visible behavior. The methods of studying these condensates generally follow a quantum mechanical (bottom up) or phenomenological (top down). In principal, bottom up methods are sufficient to describe all behavior, but in practice the calculations become intractable. The effect of electronic structure on the formation of FFLO phases was studied using a modified BCS formalism. Features of the Fermi surfaces which promoted the formation of FFLO phases were identified. Magnetically induced orbital currents, vortex dynamics and multi-order parameter superconductors were studied using the phenomenological formalism of Ginzburg and Landau. A new topological structure was identified in multi-order parameter superconductors with Josephson coupling. The electronic structure tools the were developed for studying FFLO phases were then applied $TiBe_2$. The source of the anomalous temperature dependent susceptibility was identified. Classical magnetism was studied using transfer matrix methods. A method was developed for extracting the density of states for long, narrow, nearest neighbor, 2D Ising and Edwards-Anderson spin systems.

Contents

List of Figures

Chapter 1

Theory of $\vec{q} \neq 0$ Pairing Superconductivity

1.1 Introduction

The work in this chapter is derived from the publication

"Fermiology and Fulde-Ferrell-Larkin-Ovchinnikov Phase Formation"; A. B. Kyker, W. E. Pickett, and F. Gygi, *Phys. Rev. B* **71**, 224517 (2005).

Almost half a century ago Ginzburg addressed the question of possible superconductivity in ferromagnetic material[1], and studied the problems posed by orbital supercurrents within a material with intrinsic magnetic flux. About a decade later, and armed with BCS theory[2], Fulde and Ferrell (FF)[3] and separately Larkin and Ovchinnikov (LO)[4] addressed the separate question with how a BCS superconductor copes with an intrinsic spin splitting, which breaks the degeneracy of spin up and spin down Fermi surfaces. Both FF and LO concluded that (neglecting orbital current effects) that there is a superconducting phase (the "FFLO phase") above the usual upper critical field H_{c2} where superconductivity persists based on $\vec{q} \neq 0$ (non-zero momentum) pairs and the order parameter becomes inhomogeneous.

Since that time there has been a considerable number of papers exploring the competition between, and possible coexistence of, the superconducting and magnetic long range order parameters.[5] Full treatment requires consideration of both orbital and spin effects, and for the most part theories have tended to suppose that one is dominant in a particular system and concentrate on that one. Thus investigations have focused either on the orbital effects such as spontaneous vortex phases, or on the exposition of the FFLO phase without complications from vortex behavior. Much has been accomplished with

this approach, although little in a material specific way that would allow theories to be carefully tested. With regard to the FFLO phase, the move has been in the opposite direction: make the system fit the idealizations of the theorists.

Two dimensional layered organic crystals provide the primary playground. With negligible carrier hopping between layers and the magnetic field can be oriented nearly in-plane, the competition between spin- and orbital-pairbreaking first studied theoretically by Bulaevskii[6] can be probed. If the field lies precisely within the layer, orbital pairbreaking vanishes leaving only a small exchange splitting ($\pm\mu_B B$) to inhibit superconductivity. This setup has led to strong evidence that a distinct high field, low temperature phase in κ-(BEDT-TTF)$_2$Cu(NCS)$_2$ is an excellent candidate for an FFLO phase.[7] The observed new phase seems consistent with theoretical expectations,[8] and is suggested to arise due to a favorable Fermi surface shape.[7]

A less prosaic candidate, still within the quasi-two-dimensional realm, is λ-(BETS)$_2$FeCl$_4$, which contains the conducting layers of BETS molecules and layers of Fe^{3+} magnetic ions. At ambient pressure it undergoes a transition to an antiferromagnetic insulating phase below 10 K. Upon application of a field, it undergoes an insulator-to-metal transition at 11 T and then becomes superconducting above 16-17 T, with T_c increasing with field.[9, 10] The field-induced superconductivity is thought to be due to the Jaccarino-Peter mechanism in which the applied field counteracts the internal exchange field due to the magnetic ions, enabling singlet pairing. At the edges of this field-induced superconducting phase, FFLO phases are expected to arise.[11] Experimental determination of the Fermi surface[12] has become a central part of the understanding of this system.

An FFLO phase has been suggested to account for a second superconducting phase deep within ($H < H_{c2}$) the main superconducting phase in $CeCoIn_5$.[13] This compound is a favorable case for an FFLO phase because it is extremely pure and due to its large Maki parameter (which indicates that orbital pair-breaking is a minor effect). The transition between the suggested FFLO phase and the normal state is first order. It has also been found that the phase boundaries depend strongly on the direction of the applied field.[14] Observation of a possible FFLO phase has also been argued for UBe_{13}[15], based on a strong upturn in the upper critical field at low temperature.

Underlying the criteria for a specific superconducting phase is not only the coupling strength and character (anisotropy, for example), but also the characteristics of the Fermi surface where superconductivity "lives." It is vaguely expected , of course, that FFLO pairing is favored by "nesting" in some sense of the exchange-split Fermi surfaces. Specifically, however, little has been established quantitatively about the importance of the shape of the FS, and the value and the anisotropy of the Fermi velocity of the quasiparticles. These aspects can be very important for superconducting properties, for example, the symmetry of the vortex lattice can change depending on the degree of anisotropy of the Fermi velocity around the FS,[16] and the quasiparticle spectrum within a vortex is sensitive to the Fermi surface topology.[17]

FFLO phases are traditionally studied in the context of exchange splitting due to applied fields, but the same situations arise for superconductivity in weak ferromagnets (which was what FF and LO had in mind). The recent identification of several examples of superconductivity coexisting with weak ferromagnetism ($RuSr_2GdCu_2O_8$, UGe_2, URhGe,

ZrZn2) and in close proximity to the magnetic quantum critical point (QCP), broadens the interest in the effects of exchange splitting on pairing and superconducting phenomenology. Certainly near the QCP where the exchange splitting goes to zero, the action depends strongly on the Fermiology, and Sandeman *et al.* have modeled the metametamagnetic behavior of UGe_2 in terms of changing Fermi surface topology.[18] The spectrum of critical fluctuations near the QCP are also sensitive to the Fermiology, specifically the magnitude and anisotropy of the Fermi velocity.[19] In $ZrZn_2$ additional phases (differing at least in magnetic properties) have recently been observed.[20]

1.2 Cooper Pair

With several decades between the discovery of superconductivity and a successful microscopic description one can appreciate that it was a difficult problem. This is especially true when one considers that the dramatic nature of the superconducting phenomena attracted a great many of the best minds of the day.

In an important development in 1956, L.N. Cooper [21] was able to show that an arbitrarily small attractive potential between two electrons added to a non-interacting Fermi sea was sufficient to produce a bound state. This was a somewhat surprising result since it was well known that in three dimensions a minimum attractive potential was required to produce a bound state.

Taking $\epsilon_F \equiv 0$ and using operator notation, the Hamiltonian Cooper considered is

$$H_C = H_0 + H_P = \sum_{\vec{k},\sigma} \epsilon_{\vec{k}} c^\dagger_{\vec{k},\sigma} c_{\vec{k},\sigma} + \sum_{\vec{k},\vec{k'}} c^\dagger_{\vec{k'},\uparrow} c^\dagger_{-\vec{k'},\downarrow} V_{\vec{k'},\vec{k}}\, c_{-\vec{k},\downarrow} c_{\vec{k},\uparrow} \tag{1.1}$$

where the sums are over all states above the Fermi level and $c_{\vec{k},\sigma}$ is a destruction operator for an eigenstates of H_0. The potential $V_{\vec{k},\vec{k'}}$ acts on spin zero pairs of eigenstates of H_0 which form a complete set of zero momentum states. The creation field operator for an eigenstate of H_C and eigenstates of H_C and H_0 can be written as

$$\begin{aligned} \psi^\dagger &= \sum_{\vec{k}} a_{\vec{k}} c^\dagger_{\vec{k},\uparrow} c^\dagger_{-\vec{k},\downarrow} \\ |\psi_{\vec{k}}> &= \psi^\dagger |G> \\ |\theta_{\vec{k}}> &= c^\dagger_{\vec{k},\uparrow} c^\dagger_{-\vec{k},\downarrow} |G> \end{aligned} \tag{1.2}$$

where the ground state $|G>$ is taken ot be the filled Fermi sea. The eigenvalue problem is solved by first projecting out a single $\theta_{\vec{k}}$:

$$\begin{aligned} < \theta_{\vec{k}}|H_C|\psi > &= < \theta_{\vec{k}}|H_0 + H_P|\psi > \\ a_{\vec{k}}W &= a_{\vec{k}}2\epsilon_{\vec{k}} + \sum_{\vec{k'}} a_{\vec{k'}}V_{\vec{k'},\vec{k}} \end{aligned} \tag{1.3}$$

where W is the eigen energy. Then solving for $a_{\vec{k}}$ gives

$$a_{\vec{k}} = \frac{\sum_{\vec{k'}} a_{\vec{k'}}V_{\vec{k},\vec{k'}}}{W - 2\epsilon_{\vec{k}}} \tag{1.4}$$

In general this integral equation is not solvable, so it is customary to make the approximation that $V_{\vec{k},\vec{k'}} = -V$ for all $\vec{k}$ and $\vec{k'}$ in a thin energy shell $\hbar\omega_D$ above the Fermi energy and zero otherwise. Then summing over all $\vec{k}$ within the energy limits gives:

$$\sum_{\vec{k}} a_{\vec{k}} = \left(\sum_{\vec{k'}} a_{\vec{k'}}\right) \sum_{\vec{k}} \frac{-V}{W - 2\epsilon_{\vec{k}}} \tag{1.5}$$

Dividing by $\sum_{\vec{k}} a_{\vec{k}}$ and performing the integration

$$1 = \sum_{\vec{k}} \frac{-V}{W - 2\epsilon_{\vec{k}}} = -V \int_0^{\hbar\omega_D} \frac{N(\epsilon)}{W - 2\epsilon} d\epsilon \approx \frac{VN(0)}{2} log\left(1 - \frac{2\hbar\omega_D}{W}\right) \tag{1.6}$$

where the density of states is assumed to be nearly constant over the energy range of integration. Here one can see how the Pauli exclusion of occupied states in the Fermi sea creates a extensive degeneracy of the lowest available states and thereby enables the low lying bound state. The binding energy is found by solving for W

$$W = \frac{2\hbar\omega_D}{1 - e^{2/VN(0)}} \approx -2\hbar\omega_D e^{-2/N(0)V} \tag{1.7}$$

where the approximation is valid for weak coupling, $N(0)V << 1$.

Pairing of non-localized electrons in momentum space (suggested by F. London[22]) is attractive because it suggests that screening of the strong Coulomb repulsion allows a weak attractive potential to dominate. The resulting Cooper pair are non-local, but the average real space electron separation has been estimated for reasonable parameters to be $\approx 1\mu$m[23]. This is more than sufficient for screening to occur.

The assumption that $V_{\vec{k}',\vec{k}}$ is even in $\vec{k}$ forces the pairing to spin singlets. Singlet is not the only possible pairing. The Fermonic super fluid Helium forms triplet states [24] and some "unconventional" superconductors such as Sr_2RuO_4 are thought to also to form triplets [25]. A spin zero triplet pair will have the form

$$\psi_{T0} = \sum_{\vec{k}} a_{\vec{k}} \left(\frac{c^\dagger_{\vec{k},\uparrow} c^\dagger_{-\vec{k},\downarrow} + c^\dagger_{\vec{k},\downarrow} c^\dagger_{-\vec{k},\uparrow}}{\sqrt{2}} \right) \tag{1.8}$$

while there are two possible spin one triplets of the form

$$\psi_{T\sigma} = \sum_{\vec{k}} a_{\vec{k}} c^\dagger_{\vec{k},\sigma} c^\dagger_{-\vec{k},\sigma}. \tag{1.9}$$

1.3 BCS

Using the electron pairing model, J. Bardeen, L. N. Cooper, and J. R. Schrieffer (BCS) developed a model for superconductivity in 1957 [2] earning them the 1972 Nobel prize in physics. The model they developed assumes non-interacting normal electrons and non-interacting Cooper pairs and correctly predicted much of the experimental observations.

The BCS (Bardeen-Cooper-Schrieffer) reduced Hamiltonian with exchange splitting $\pm\mu_B B$, in units in which $\mu_B = 1$, is

$$\begin{aligned} H &= \sum_{\vec{k}} \epsilon_{\vec{k}} (n_{\vec{k}\uparrow} + n_{-\vec{k}\downarrow}) \\ &- B \sum_{\vec{k}} (n_{\vec{k}\uparrow} - n_{-\vec{k}\downarrow}) \\ &- g \sum_{\vec{k}\vec{k}'} c^{\dagger}_{\vec{k}'\uparrow} c^{\dagger}_{-\vec{k}'\downarrow} c_{-\vec{k}\downarrow} c_{\vec{k}\uparrow} \end{aligned} \tag{1.10}$$

Here $c^{\dagger}_{\vec{k}\sigma}$ ($c_{\vec{k}\sigma}$) is the creation (destruction) operator for single electron states, $n_{\vec{k}\sigma} \equiv c^{\dagger}_{\vec{k}\sigma} c_{\vec{k}\sigma}$, and the single particle dispersion is referenced to the Fermi energy ϵ_F=0. The attractive pairing strength g is positive for single particle energies $|\epsilon_{\vec{k}}|$ within a cutoff energy ϵ_c, and zero otherwise. Use is made of the symmetry $\epsilon_{-\vec{k}} = \epsilon_{\vec{k}}$ to write the first two terms in an unconventional manner (involving $n_{-\vec{k}\downarrow}$ rather than $n_{\vec{k}\downarrow}$).

To accommodate the formalism to pairing with momentum $\vec{q}$, the interaction

term of the Hamiltonian is rewritten for pairing of states $(\vec{k}+\frac{\vec{q}}{2})\uparrow$ with $(-\vec{k}+\frac{\vec{q}}{2})\downarrow$,

$$\begin{aligned} H &= \sum_{\vec{k}} \epsilon_{\vec{k}}(n_{\vec{k}\uparrow} + n_{-\vec{k}\downarrow}) \\ &- B\sum_{\vec{k}}(n_{\vec{k}\uparrow} - n_{-\vec{k}\downarrow}) \\ &- g\sum_{\vec{k}\vec{k}'} c^{\dagger}_{\vec{k}'+\frac{\vec{q}}{2},\uparrow} c^{\dagger}_{-\vec{k}'+\frac{\vec{q}}{2},\downarrow} c_{-\vec{k}+\frac{\vec{q}}{2},\downarrow} c_{\vec{k}+\frac{\vec{q}}{2},\uparrow} \end{aligned} \tag{1.11}$$

The $\vec{k}+\frac{\vec{q}}{2},\uparrow$ and $-\vec{k}+\frac{\vec{q}}{2},\downarrow$ indices appearing in the pairing potential can be simplified in preparation for the Bogoliubov-de Gennes (BdG) transformation:

$$\tilde{c}^{\dagger}_{\vec{k}\sigma} \equiv c^{\dagger}_{\vec{k}+\frac{\vec{q}}{2},\sigma}, \quad \tilde{c}^{\dagger}_{-\vec{k}\sigma} \equiv c^{\dagger}_{-\vec{k}+\frac{\vec{q}}{2},\sigma}, \tag{1.12}$$

$$\tilde{n}_{\vec{k}\sigma} \equiv \tilde{c}^{\dagger}_{\vec{k},\sigma}\tilde{c}_{\vec{k},\sigma} \tag{1.13}$$

A further simplification is made by making a small $\vec{q}$ approximation:

$$\epsilon_{\vec{k}+\frac{\vec{q}}{2}} \approx \epsilon_{\vec{k}} + \frac{\vec{q}}{2}\cdot\vec{v}_{\vec{k}}, \quad \vec{v}_{\vec{k}} \equiv \vec{\nabla}\epsilon_{\vec{k}} \tag{1.14}$$

The Fermi surface that defines $\vec{v}_{\vec{k}}$ at $\vec{k} = \vec{k}_F$ is the non-spin polarized normal state Fermi surface. With the linear approximation, the normal state Fermi surface marks the superconducting state's chemical potential.

After collecting operators with common $\vec{k}$, the Hamiltonian for non-zero momentum becomes:

$$\begin{aligned} H &= \sum_{\vec{k}} \epsilon_{\vec{k}}(\tilde{n}_{\vec{k}\uparrow} + \tilde{n}_{-\vec{k}\downarrow}) \\ &+ \sum_{\vec{k}}(\frac{\vec{q}}{2}\cdot\vec{v}_{\vec{k}_F} - B)(\tilde{n}_{\vec{k}\uparrow} - \tilde{n}_{-\vec{k}\downarrow}) \\ &- g\sum_{\vec{k}\vec{k}'} \tilde{c}^{\dagger}_{\vec{k}'\uparrow}\tilde{c}^{\dagger}_{-\vec{k}'\downarrow}\tilde{c}_{-\vec{k}\downarrow}\tilde{c}_{\vec{k}\uparrow} \\ &= \sum_{\vec{k}\sigma} \xi_{k\sigma}\tilde{n}_{\vec{k}\sigma} - g\sum_{\vec{k}\vec{k}'} \tilde{c}^{\dagger}_{\vec{k}'\uparrow}\tilde{c}^{\dagger}_{-\vec{k}'\downarrow}\tilde{c}_{-\vec{k}\downarrow}\tilde{c}_{\vec{k}\uparrow}, \end{aligned} \tag{1.15}$$

where the spin-dependent dispersion is given by

$$\xi_{s_\sigma \vec{k}\sigma} = \epsilon_{\vec{k}} + s_\sigma w_{\vec{k}}; \quad w_k \equiv \frac{\vec{q}}{2} \cdot \vec{v}_{\vec{k}_F} - B.$$
$$s_\uparrow \equiv 1; \quad s_\downarrow \equiv -1 \tag{1.16}$$

In this form several new features can be understood. First, because of the convention of associating $\vec{k}$ with up spin and $-\vec{k}$ with down spin and assuming inversion symmetry of the Fermi surface, the pair momentum $\vec{q} \neq 0$ acts so as to add another *effective* Zeeman splitting term to the Hamiltonian. Second, the new Zeeman splitting term is a peculiar one that varies over the Fermi surface. A central feature in the physics and in the understanding of the resulting phenomena is that for one half of the Fermi surface these splittings (from B, and from $\vec{q}$) tend to cancel, which enables FFLO superconducting states to arise.

1.4 Bogoliubov-Valatin transformation

The mean field approximation for the superconducting state consists of presuming the appearance of an order parameter

$$b_k = < \tilde{c}_{-k\downarrow} \tilde{c}_{k\uparrow} >, \tag{1.17}$$

introducing the tautology

$$\tilde{c}_{-k\downarrow} \tilde{c}_{k\uparrow} = b_k + (\tilde{c}_{-k\downarrow} \tilde{c}_{k\uparrow} - b_k), \tag{1.18}$$

and neglecting the product of the fluctuations (terms in parentheses) in the interaction term. In the case we consider b_k gives the amplitude for finding a pair with momentum $\vec{q}$

and zero spin in the superconducting state. The "energy gap" (see below for clarification) is given by

$$\Delta = g \sum_k b_k, \tag{1.19}$$

from which it is seen that the assumption of an isotropic coupling matrix elements g leads to an isotropic gap. The Hamiltonian becomes:

$$H = \sum_{\vec{k}\sigma} \xi_{k\sigma} \tilde{n}_{\vec{k}\sigma} - \sum_{\vec{k}} \left[\Delta \tilde{c}^{\dagger}_{\vec{k}'\uparrow} \tilde{c}^{\dagger}_{-\vec{k}'\downarrow} + h.c. \right]. \tag{1.20}$$

The resulting mean field Hamiltonian is diagonalized by a Bogoliubov-Valatin (BV) transformation, leading to the Bogoliubov-de Gennes equations. In general, the BV transformation leads to quasiparticles that are superpositions of electrons and holes with both up and down spin. The Hamiltonian matrix which defines the quasiparticle eigen amplitudes and eigenenergies is

$$\begin{pmatrix} \epsilon_{\vec{k}} + w_k & 0 & 0 & \Delta \\ 0 & \epsilon_{\vec{k}} - w_k & -\Delta & 0 \\ 0 & -\Delta^* & -\epsilon_{-\vec{k}} - w_k & 0 \\ \Delta^* & 0 & 0 & -\epsilon_{\vec{k}} + w_k \end{pmatrix} \times \begin{pmatrix} C_{\tau,\vec{k}\uparrow} \\ C_{\tau,-\vec{k}\downarrow} \\ D_{\tau,\vec{k}\uparrow} \\ D_{\tau,-\vec{k}\downarrow} \end{pmatrix} = E_{\tau,\vec{k}} \begin{pmatrix} C_{\tau,\vec{k}\uparrow} \\ C_{\tau,-\vec{k}\downarrow} \\ D_{\tau,\vec{k}\uparrow} \\ D_{\tau,-\vec{k}\downarrow} \end{pmatrix} \tag{1.21}$$

where τ is an index for the 4 possible quasiparticle states and C and D are the coefficients for the single particle creation and destruction operators respectively.

The expression of Powell, Annett, and Gyorffy [26] for more general types of pairing (albeit only $\vec{q}$=0) reduces to this form for singlet pairing. Diagonalizing the matrix, which reduces to a pair of 2×2 matrices, produces four branches of quasiparticles states with definite spin and eigenenergies

$$E^{\pm}_{s_\sigma \vec{k}\sigma} = s_\sigma w_{\vec{k}} \pm \sqrt{\epsilon^2_{\vec{k}} + \Delta^2} \tag{1.22}$$

and which obey the Fermion anti-commutator relations.

In the superconducting ground state with $w_{\vec{k}} = 0$, (i.e. $\vec{q} = 0$ and $B = 0$), all of the negative energy states will be occupied. The positive energy states can then be considered quasiparticle excitations. The rest of the analysis will be in terms of these excitations. The quasiparticle operators are:

$$\begin{aligned}
\gamma^\dagger_{\vec{k}\uparrow} &= u_{\vec{k}}\tilde{c}^\dagger_{\vec{k}\uparrow} \quad +0 \quad +0 \quad -v_{\vec{k}}\tilde{c}_{-\vec{k}\downarrow} \\
\gamma^\dagger_{-\vec{k}\downarrow} &= 0 \quad +u_{\vec{k}}\tilde{c}^\dagger_{-k\downarrow} \quad +v_{\vec{k}}\tilde{c}_{k\uparrow} \quad +0 \\
\gamma_{\vec{k}\uparrow} &= 0 \quad -v_{\vec{k}}\tilde{c}^\dagger_{-k\downarrow} \quad +u_{\vec{k}}\tilde{c}_{k\uparrow} \quad +0 \\
\gamma_{-\vec{k}\downarrow} &= v_{\vec{k}}\tilde{c}^\dagger_{\vec{k}\uparrow} \quad +0 \quad +0 \quad +u_{\vec{k}}\tilde{c}_{-\vec{k}\downarrow}
\end{aligned} \tag{1.23}$$

where $u_{\vec{k}}$ and $v_{\vec{k}}$ are given by

$$\begin{aligned}
\sqrt{2}\ u_{\vec{k}} &= \sqrt{1 + \frac{\epsilon_{\vec{k}}}{\sqrt{\epsilon^2_{\vec{k}} + \Delta^2}}} \\
\sqrt{2}\ v_{\vec{k}} &= \sqrt{1 - \frac{\epsilon_{\vec{k}}}{\sqrt{\epsilon^2_{\vec{k}} + \Delta^2}}}.
\end{aligned} \tag{1.24}$$

The BCS results are recovered when $w_k = 0$ and $\vec{q} = 0$. It is interesting that the quasiparticle amplitudes $u_{\vec{k}}$ and $v_{\vec{k}}$ are independent of the Zeeman splitting. This can be understood by noting that w_k in each 2×2 submatrix enters proportional to the identity matrix.

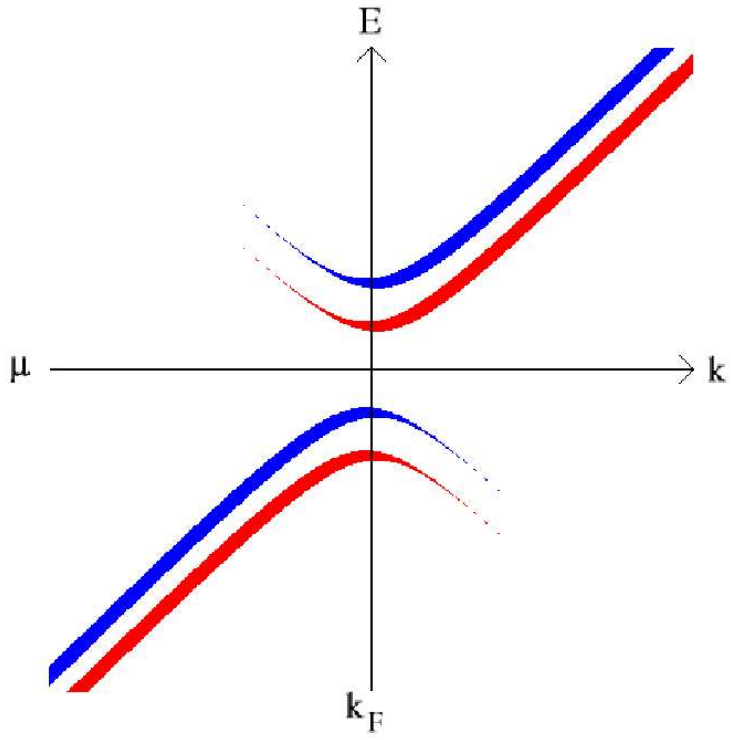

Figure 1.1. Sketch of the four branches of the quasiparticle dispersion in a magnetic superconductor. An energy gap of 2Δ opens at the Fermi surface between quasiparticles with common spin direction. The exchange splitting will reduce the opposite-spin gap, but does not directly effect the superconducting parameter Δ. The thickness of the line represents the electron character of the quasiparticles.

1.5 The Gap equation

The quantity 2Δ becomes the gap between the quasiparticle eigenenergies with common spin label. The actual *opposite-spin gap*, $2\Delta - 2|w_{\vec{k}}|$, does not enter the gap equation directly, and the quasiparticle energies enter only through the Fermi occupation functions. See Fig. 1.1. The gap equation is given by:

$$\Delta = g\sum_{\vec{k}} u_{\vec{k}} v_{\vec{k}} (1 - f(E^{+}_{\vec{k}\uparrow}) - f(E^{+}_{-\vec{k}\downarrow})) \tag{1.25}$$

Since the index $\vec{k}$ now enters through the energy term $s_\sigma \frac{\vec{q}}{2} \cdot \vec{v}_{\vec{k}}$ as well as through $\epsilon_{\vec{k}}$, it is no longer possible to simply change the $\vec{k}$ summation to a one dimensional energy integral scaled by the density of states at the Fermi surface, which is the technique typically applied when the Zeeman term is not $\vec{k}$ dependent.

Introducing the integral over δ-function $1 = \int \delta(\hat{q} \cdot \vec{v}_{\vec{k}_F} - V) dV$ in addition to the usual one $1 = \int \delta(\epsilon - \epsilon_k) d\epsilon$ leads to the form of the gap equation that we focus on:

$$\begin{aligned} \Delta &= N_0 g \int dV N(V, \hat{q}) \int_{-\epsilon_c}^{\epsilon_c} d\epsilon \frac{\Delta}{2\sqrt{\epsilon^2 + \Delta^2}} \\ &\quad \times (1 - f(E^{+}_{\uparrow}) - f(E^{+}_{\downarrow})) \\ &= \lambda \int dV N(V, \hat{q})\ K(\Delta, T, \frac{1}{2} qV - B). \end{aligned} \tag{1.26}$$

N_0 is the density of states evaluated at E_F and we introduce the usual coupling strength $\lambda = N_0 g$, $E^{(+)}_\sigma$ is given by Eq. 1.22 with $\epsilon_{\vec{k}} \to \epsilon$, and the variation in $N(E)$ within ϵ_c of the Fermi level has been neglected. This expression reduces to BCS when $|\vec{q}| = 0$. The dependence on exchange splitting enters only through the quasiparticle eigenenergies. In the second expression the kernel K already includes the energy integral.

The new function that has been introduced is the Fermi surface projected-velocity distribution that depends on the direction of $\vec{q}$

$$\begin{aligned} N(V,\hat{q}) &= \frac{1}{N_0}\sum_{\vec{k}} \delta(\epsilon_F - \epsilon_{\vec{k}})\delta(\hat{q}\cdot\vec{v}_{\vec{k}_F} - V) \\ &= \frac{1}{N_0}\frac{\Omega_c}{(2\pi)^3}\oint_{fs}\frac{\delta(\hat{q}\cdot\vec{v}_{\vec{k}_F} - V)}{|\vec{v}_{\vec{k}_F}|}ds, \end{aligned} \tag{1.27}$$

which is normalized as

$$\int N(V,\hat{q})dV = 1. \tag{1.28}$$

$N(V,\hat{q})$ will be called the *nesting density* for reasons related to FFLO phase formation. The Fermi surface geometry and the variation of the velocity get folded into $N(V,\hat{q})$, which incorporates the local density of states factor $1/|\vec{v}_{\vec{k}_F}|$. The energy integral, $K(\Delta, T, \frac{1}{2}qV - B)$, remains independent of the details of the Fermi surface.

We will explore the solutions to the gap equation while varying the parameters T, B, Δ, and q for a given dispersion relation $\epsilon_{\vec{k}}$ and coupling strength λ. It will also be of interest to consider variations in the direction of the pair momentum, however we will restrict ourselves to directions of high symmetry since these directions will provide extrema of the functions by symmetry considerations.

1.6 BCS Phase

We first mention the BCS phase diagram in the T-B plane. Ignoring magnetically induced supercurrents, any applied field will induce some magnetization by due to thermal excitations when $T > 0$. Band crossing induced magnetization and $\vec{q} = 0$ (BCS) pairing

coexist in the region S' in Fig. 1.2 between $T \approx T_c/2$ and $T = T_c$. In this region where $|B| > \Delta > 0$, the gap between opposite-spin quasiparticles closes giving rise to field induced pair breaking at the Fermi surface while pairing occurs away from the Fermi surface. When $|B| < \Delta$, an opposite-spin gap exists over the entire Fermi surface.

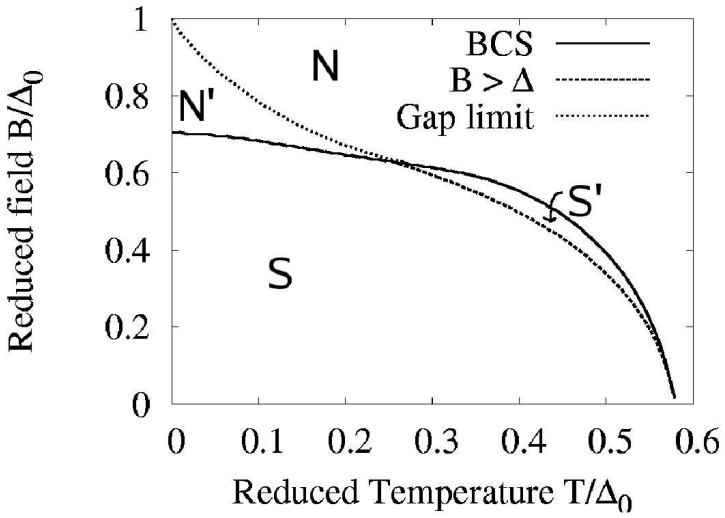

Figure 1.2. The phase diagram in the T-B plane. The solid line marks the BCS to normal phase transition. The BSC region S' between the "$B > \Delta$" and "BCS" lines has no opposite-spin excitation gap but superconducting pairing still exist. Solutions to the gap equation exist for B under the "Gap limit" region N', but the free energy of the normal phase is lower than the BCS phase.

1.7 FFLO Phase

The FFLO phase takes advantage of the Zeeman energy due to magnetization that arises when $B > \Delta$, but then uses a finite pair momentum to enhance pairing. A graphical way of understanding this enhanced pairing through the quasiparticle Fermi surface is shown in Fig. 1.3. The closing of the opposite-spin gap shrinks the minority spin Fermi surface while expanding the majority spin. The coupling of the pair momentum to the quasiparticle eigenenergy is then used to reopen an opposite-spin gap on part of the Fermi surface. Due to inversion symmetry of the dispersion relationship $\epsilon_{\vec{k}}$, spin splitting on the opposite side of the Fermi surface is increased. This trade-off can be energetically favorable because pairing is strongest near the Fermi surface. Nesting can be said to occur on the portions of the Fermi surface where an opposite-spin gap is closed by a given $\vec{q}$.

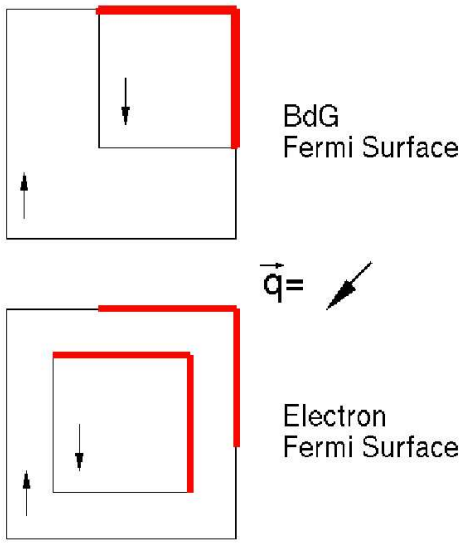

Figure 1.3. The top graph represents occupied BdG quasiparticle states in $\vec{k}$ and $-\vec{k}$ space for spin up and spin down respectively for 2D square Fermi surfaces. This non-standard representation highlights how the pairing momentum nests the Fermi surfaces by canceling the magnetic induced splitting to enable pairing. The bottom graph is the electron Fermi surfaces. In the electron picture states are not shifted by the pair momentum as in the quasipartical picture.

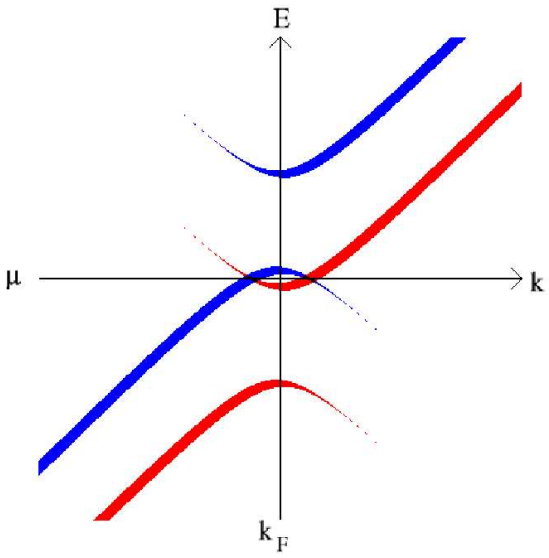

Figure 1.4. BdG quasiparticles excitations occur when the combination of the magnetic exchange splitting and pair momentum induced splitting are greater than Δ. This graph corresponds to the separated part of the BdG Fermi surfaces in Fig. 1.3. The fact that the quasiparticles are a superposition of holes and electrons results in the spin separation appearing more uniformly in the electron Fermi surfaces in Fig. 1.3.

FFLO phases are favored when (1) enough of the Fermi surface can be paired (nesting is strong enough) to allow for a superconducting ($\Delta \neq 0$) solution to the gap equation, (2) the FFLO free energy is less than the BCS free energy and normal paramagnetic free energy. Using the form of the gap equation that includes the nesting density, we want to understand what features of the Fermi surface favor the FFLO state. For a given splitting and direction of $\hat{q}$, the lowest FFLO free energy occurs when pairing is maximized. Pairing is enhanced when $\frac{1}{2}qV = \frac{\vec{q}}{2} \cdot \vec{v}_{\vec{k}_F}$ is chosen to cancel the magnetic splitting on some part of the Fermi surface. The value of q selects the range of V where $|\frac{1}{2}qV - B| < \Delta$ (e.g. where nesting occurs).

The effective width of nesting in V space can be found by noting when the quasiparticle eigenenergies are greater than zero at the Fermi surface. Rewriting the inequality as $|\frac{1}{2}q(V_0 + \delta V) - B| < \Delta$, we find

$$\delta V \approx \frac{2\Delta}{q} \approx \left|\frac{V_0 \Delta}{B}\right| \tag{1.29}$$

where V_0 solves the equation $|\frac{1}{2}qV_0 - B| = 0$. In general, V_0 will be optimal near a peak in the nesting density and as large as possible to maximize δV.

Figure 1.5 illustrates the behavior of the energy integral $K(\Delta, T, \frac{1}{2}qV - B)$ for two possible choices of q which solve the equation $|\frac{1}{2}qV_0 - B| = 0$ at different values of V_0, $T = 0$, and fixed $\Delta < B$. As long as $\Delta > B - qV$, the integral will be a constant (≈ 0.4 in this case). For the $q = 0$ case, $\Delta < B - 0V$ over the entire range causing pair breaking over the entire Fermi surface. The figure also shows two possible values of pair momentum. Plateaus occur when $\Delta < B - qV$ causes both Fermi functions to be zero at

the Fermi surface.

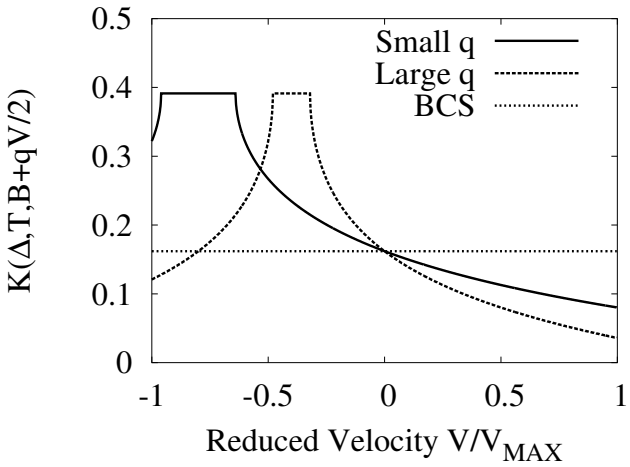

Figure 1.5. Graph of the energy integral part of the gap equation ($K(\Delta, T, \frac{1}{2}qV - B)$) as a function of V for two values of q, fixed Δ and $T = 0$. The plateau occur where the magnitude of the exchange splitting energy is less than Δ since this is where both Fermi functions are zero at the Fermi surface. The sharp drop at the edge of the plateau reflects the breaking of pairs at the Fermi surface. Note how low values of q produce wider plateaus at higher values of V.

1.8 Applications of Nesting Density to FFLO calculations

For the calculations, we normalize $\Delta(B = 0, T = 0) = \Delta_0 = 1$ to specify the energy scale for the problem. The energy cutoff for the gap equation is a parameter that is set to $\epsilon_c = 50\Delta_0$. In a real material the energy cutoff would be determined by the pairing boson (phonon, spin fluctuation, etc.). With the above parameters set, the coupling strength λ now becomes a function of ϵ_c and Δ_0 , given by

$$\frac{1}{\lambda} = sinh^{-1}\left(\frac{\epsilon_c}{\Delta_0}\right) \tag{1.30}$$

In the weak coupling regime ($\lambda \equiv N_o g << 1$) this reduces to the well known BCS relation $\Delta_0 = 2\epsilon_c e^{-1/\lambda}$. This coupling strength $\lambda \approx 0.2$ for $\epsilon_c/\delta_0 = 50$ is well within the weak coupling regime for which the equations were derived.

The free energy competition between BCS and FFLO is a crucial factor in determining whether an FFLO state will exist. Even in the best case, at $T = 0$ the free energy driven transition from BCS to FFLO occurs very near the BCS critical field which is proportional to the density of states at the Fermi surface. The FFLO critical field calculation is more complex. A higher proportion of FFLO pairs occur in electron states away from the Fermi surface and on average pay a higher kinetic energy cost. However to first order the FFLO critical field is determined by the fraction of nesting density where pairing occurs at the Fermi surface. If the FFLO critical field is less than the BCS critical field for a material, no FFLO states will exist.

1.9 1D Fermi Surface

The simplest case is the 1D Fermi surface. The nesting density consists of δ functions at $\pm v_F$. The resulting phase diagram is given in Fig. 1.6. At $T = 0$, solutions to the gap equation extend to arbitrarily large B with a correspondingly large $q = 2B/v_F$. Free energy constraints however limit the FFLO phase to finite B.

At the higher applied fields, the pairing on one half of the Fermi surface will be almost completely suppressed and not contribute to the condensate. It may be possible that a second condensate form that has opposite pair momentum.

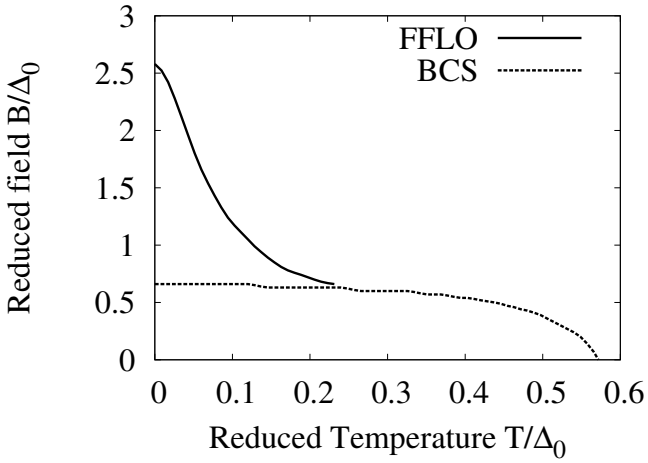

Figure 1.6. The phase diagram of a 1D system. The presence of a δ function in the nesting density guarantees that half the density of states at the Fermi surface can always be paired.

1.10 2D Fermi Surface

The nesting density of states for 2D Fermi surfaces will tend to have van Hove like singularities, as observed by Shimahara [27], that produce strong peaks in $N(V, q)$ that go as $1/\sqrt{|V_{peak} - V|}$. These peaks arise whenever $V = \hat{q} \cdot \vec{v}_F$ is at a local extremum. A simple example is the circular Fermi surface. The projected velocity is $V = |v_F| cos(\phi)$ where ϕ is the angle between $\vec{v}_F$ and $\hat{q}$. Figure 1.7 is the nesting density for positive V and shows the peak caused by the extrema that occurs when $\hat{q}$ is normal to the Fermi surface. Figure 1.8 shows the phase diagram for the circular Fermi surface. From Eq. 1.29, we know that as B is raised, the width of pairing (δV) will go down. This happens directly through the increase of q necessary to maintain V_0 near the peak, and indirectly through the reduction in Δ caused by the decrease in pairing. This reduction in pairing as B is raised causes the FFLO phase to be quenched much earlier than the 1D case.

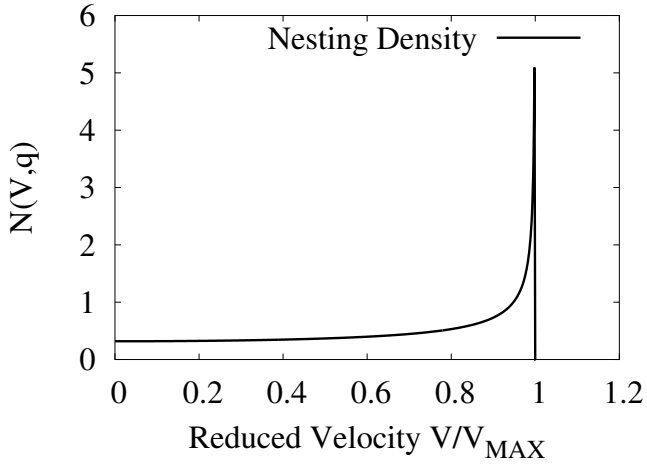

Figure 1.7. The nesting density of a 2D circular Fermi Surface for positive V showing peak at $V = |v_F|$. The optimal FFLO solution will chose a value for q such that this peak has enhanced pairing. The nesting density is symmetric around $V = 0$ due to inversion symmetry of the Fermi surface.

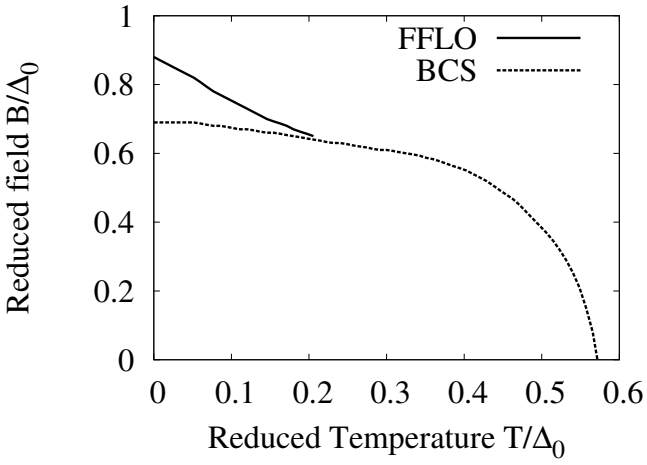

Figure 1.8. The phase diagram of a 2D circular Fermi Surface. The FFLO region is reduced from the 1D case due to a lower percentage of states benefiting from the enhanced pairing.

1.11 3D Fermi Surface

While the nesting density for 3D material may have peaks, in most cases these peaks will not be caused by van Hove singularities. This can be understood by noting that any extrema in the projected velocity will usually occur at isolated points on the Fermi surface. For example on the spherical Fermi surface, the extrema of V occur at the two points where $\hat{q}$ is normal to the Fermi surface. The nesting density for a spherical Fermi surface is constant between $\pm|v_F|$, and consequently our calculations have shown a very small FFLO region in the phase diagram.

A 3D example with a strong peak in the nesting density at V_{max} is simple cubic nearest neighbor tight binding model at half filling. With q taken in the 100 direction, the projected velocity as a function of the position on the Fermi surface is given by

$$V = V_{max} sin(k_x) \tag{1.31}$$

where that lattice constant is assumed to be 1. V has extrema at $k_x = \pm\pi/2$ which occurs along a curve defined by $cos(k_y) + cos(k_z) = 0$. Since extrema occur along a curve rather than a point, $N(V, \hat{q})$ will have integrable divergences that go as $(|V_{peak} - V|)^{-1/2}$. Figure 1.9 is the tight binding Fermi surface with the enhanced pairing region highlighted. The nesting density is similar to that shown in Fig. 1.7 with slightly more weight in the peak. Because of the increased weight, the resulting phase diagram seen in Fig. 1.10 shows an increased FFLO region relative to the circular Fermi surface case. Any deviation from the 100 direction will cause the extrema in V to occur at a few isolated points.

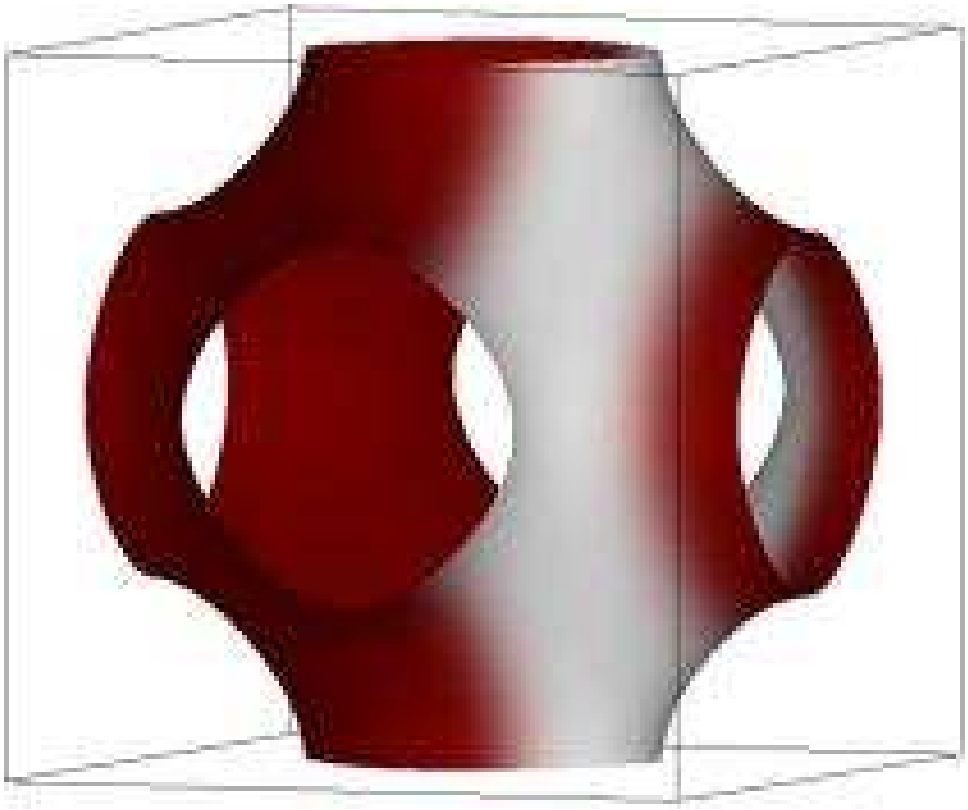

Figure 1.9. Tight binding Fermi surface at half filling. The white region corresponds to the part of the Fermi surface where enhanced pairing occurs for $T = 0$, $B \approx 0.9$, and $\hat{q}$ along the 100 direction. Because the pairing is suppressed on the opposite side of the Fermi surface, it conceivable that a separate condensate could form with $\hat{q}$ along the -100 direction.

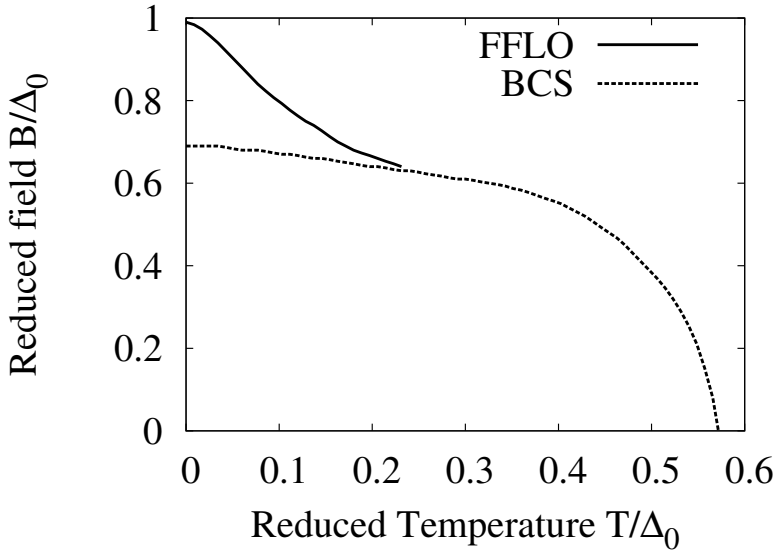

Figure 1.10. Phase diagram for the 3D nearest neighbor tight binding system shows a larger FFLO region than the circular phase diagram 1.8. This reflects the fact that the nesting density for the tight binding case has more weight near V_{max}.

1.12 $ZrZn_2$

We chose to apply our methods to $ZrZn_2$ since it has a relatively simple cubic structure, and as a weak ferromagnet it is a possible candidate to show an FFLO phase. A non-spin-polarized electronic structure calculation was performed using the FPLO [28] electronic structure code. The resulting four conduction bands and Fermi surfaces have been presented by Singh and Mazin[29]. The nesting density for the four bands that cross the Fermi surface were combined into a single $N(V, \hat{q})$ function. This represents the case of equal pairing on all bands, consistent with out constant Δ model. The preferred direction of $\hat{q}$ was found to be in the 111 direction after considering nesting properties for the three high symmetry directions. The nesting density is shown in Fig. 1.11. Most of the contribution to the density of states comes from the "cubic" shaped Fermi surface shown in Fig. 1.12 that Singh and Mazin call band 3. The large peak in the nesting density does not come from the nesting of the faces of the cube as one might expect but instead comes from the nesting of the grooves along the edges of the cube. The Fermi velocity of the faces is at least twice as large as the Fermi velocity of the grooves. The high value of the Fermi velocity of the faces reduces the contribution to the density of states, and variations of the Fermi velocity spread out the contribution to the nesting density over a range of V values.

The position of the largest peak gives the optimum value of V_0 which in conjunction with B can be used to calculate the pair momentum $q = 2B/V_0$. While this is a substantial peak, it occurs at a low value of $|V|$ which will require a high pair momentum.

As was illustrated in Fig. 1.5, high pair momentum reduces the the amount of total density available for pairing. While FFLO solutions exist for the gap equation, at no point was the free energy of these solutions below both the free energy for the BCS phase and the normal phase.

By allowing a non-uniform Δ, it may be possible for FFLO solutions to exist in a small region above the BCS phase, however other considerations make this unlikely. In the Hamiltonian we have assumed, the Zeeman splitting term B for ferromagnets includes the applied field as well as the ferromagnetic exchange energy. The average B for $ZrZn_2$ can be calculated as

$$B = \frac{M}{2N_0} \approx 30\ meV \tag{1.32}$$

where $M \approx 0.15\mu_B$ and using the Singh and Mazin calculated value $N_0 = 2.43$ states/eV-spin-unit cell). Since the Curie temperature is greater than the observed superconducting temperature, we are not able to determine $\Delta_0 = \Delta(T = 0, B = 0)$ for $ZrZn_2$. We can however place a lower bound on Δ_0 for singlet pairing by noting that even allowing for FFLO solutions, the maximum B will be on the order of $\Delta_0/\sqrt{2}$. The resulting Δ_0 is orders of magnitude to large as it would correspond to a $T_c \approx 2\Delta_0/3.52k_B = 280K$ From this we conclude that singlet pairing of either BCS or FFLO states is highly unlikely.

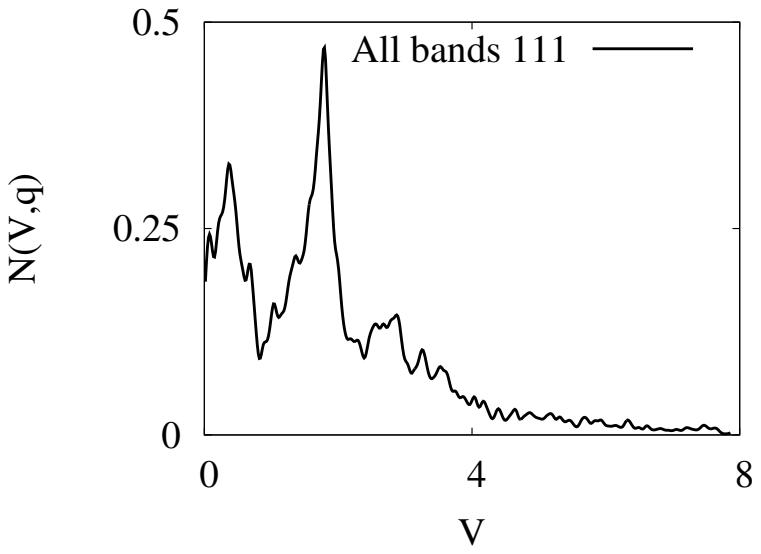

Figure 1.11. $ZrZn_2$ nesting density. The units of V are 10^7 cm/sec. A small non-zero density extends to higher values of V. The noise is a function of both the finite sampling of the Fermi surface and the complexity of the electronic structure.

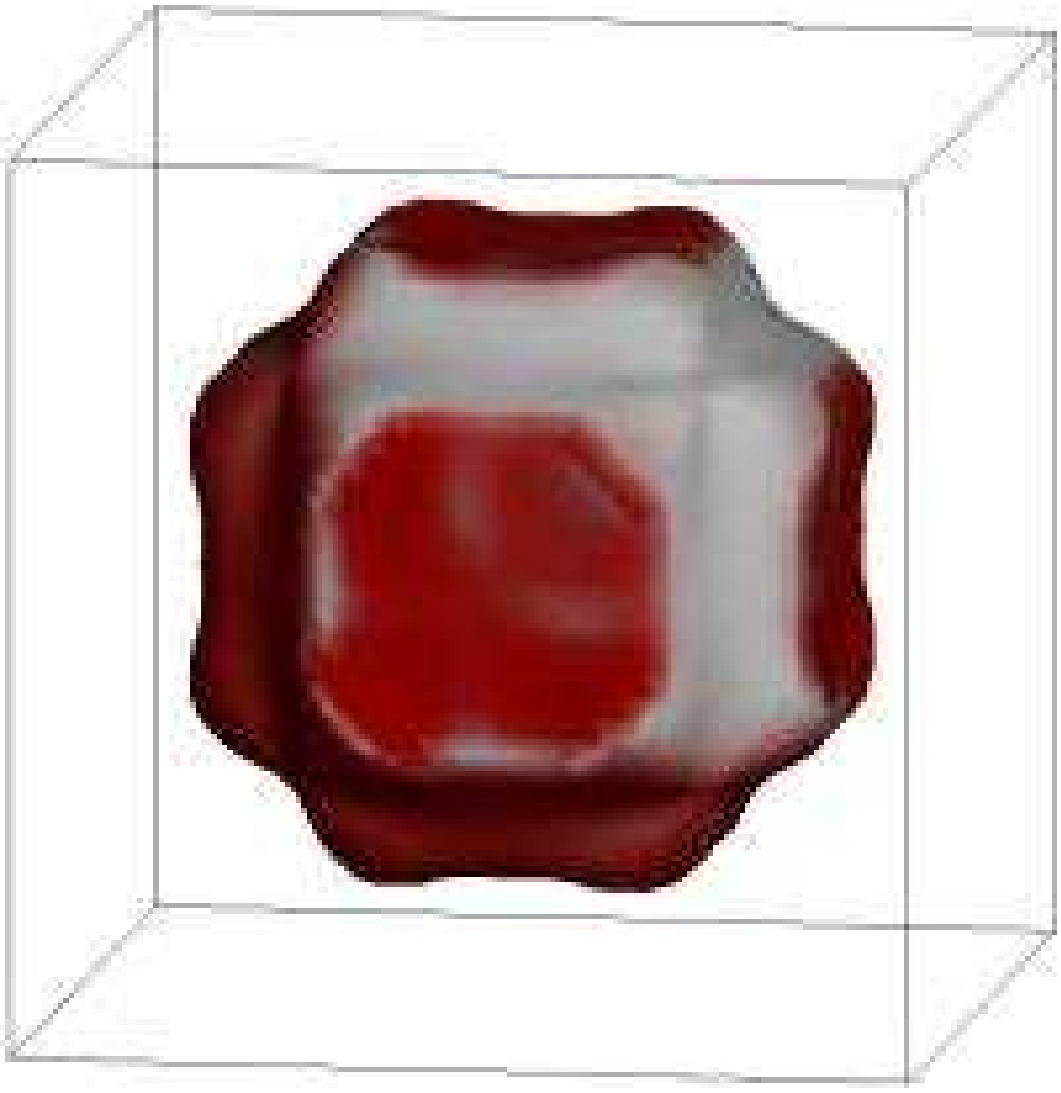

Figure 1.12. Fermi surface for the cube shaped band that is responsible for the peak in the nesting density 1.11. The white region corresponds to the part of the Fermi surface where enhanced pairing occurs for $T = 0$, $B \approx o.6$, and $\hat{q}$ in the 111 direction. It is interesting that the pairing is not favored on the relatively flat faces of the cube as one might expect. These faces however have a non-uniform velocity distribution which makes them less suitable for non-zero momentum pairing.

Recent evidence has been presented that the superconductivity observed in samples of $ZrZn_2$ is a surface phenomenon [30], consistent with the lack of any signal in the heat capacity. The superconductive surface seems to be a product of sample manufacturing and is eliminated by etching to produce a clean surface.

1.13 Conclusion

We have presented the formalism for the specific case of the quasiparticle states and eigenenergies for non-zero momentum BdG quasiparticles in an exchange field. These quasiparticles were then used to solve the superconducting gap equation within the mean field approximation. The spin polarized BdG formalism was then applied to study FFLO states which have magnetically induced spin splitting leading to pair momentum enhanced superconducting pairing on a subset of the Fermi surface. The *nesting density*, which is derived from the Fermi surface of the material being studied, was separated out and calculated to facilitate solving the gap equation and calculating free energies and other observables. In addition to providing an efficient means of performing calculations, the nesting density also proved to be a useful tool for understanding what features of a Fermi surface contribute to the formation of FFLO states.

The features of a Fermi surface which promote FFLO states are low dimensionality, specific nesting topographies, (not necessarily like those that drive charge-and spin-density waves) and relatively simple Fermi surfaces with uniform magnitude of the Fermi velocity. The benefits of low dimensionality is demonstrated by circular vs. spher-

ical Fermi surfaces. The tight binding Fermi surface illustrates the benefits of nesting topographies. It is important to recognize that the nesting topography in this case is not a "flat sheet" which we intuitively associate with nesting. The fact that FFLO states are enhanced by peaks in the nesting density at high values of V is in conflict with the reduced density of states associated with high Fermi velocities. Variations in the magnitude of the Fermi velocity will tend to place larger weights at small V which are less likely to participate in FFLO pairing.

To simplify the calculations and analysis, we chose to consider only a uniform exchange splitting which could arise from uniform ferromagnetic exchange field or from an applied field. The BdG formalism does not depend on these assumptions and could be applied to more complex situations that do not make use of a constant exchange splitting and linearized Fermi surface approximation.

1.14 Free energy calculations

In all cases, the total energy of the system was taken to be relative to the ground state of the normal metal at $T = B = 0$

$$E_g = 2 \sum_{\vec{k}<\vec{k}_F} \epsilon_{\vec{k}} \tag{1.33}$$

With $\epsilon_c = 50$ and $[B, T, \Delta] \sim 1$ in units where $\Delta_0 \equiv 1$, excitations outside the cutoff can be ignored. The free energy of the superconducting state when measured relative to the

ground state becomes

$$\begin{aligned} E_s \quad - \quad & E_g = \sum_{|\epsilon_{\vec{k}}|<\epsilon_c} \\ \{ \quad & (\epsilon_{\vec{k}} + w_{\vec{k}})(v_{\vec{k}}^2 f(E_{\vec{k}\uparrow}^-) + u_{\vec{k}}^2 f(E_{\vec{k}\uparrow}^+)) \\ + \quad & (\epsilon_{\vec{k}} - w_{\vec{k}})(v_{\vec{k}}^2 f(E_{\vec{k}\downarrow}^-) + u_{\vec{k}}^2 f(E_{\vec{k}\downarrow}^+)) \\ + \quad & (\epsilon_{\vec{k}} + \frac{q}{2} V_{\vec{k}})(\Theta(\epsilon_{\vec{k}} + \frac{q}{2} V_{\vec{k}}) - 1) \\ + \quad & (\epsilon_{\vec{k}} - \frac{q}{2} V_{\vec{k}})(\Theta(\epsilon_{\vec{k}} - \frac{q}{2} V_{\vec{k}}) - 1)\} \\ - \quad & TS - \frac{\Delta^2}{g} \end{aligned} \tag{1.34}$$

The first two terms account for the kinetic energy of the electron part of the quasi particles. The next two terms remove the kinetic energy for the ground state E_g. The last two terms are respectively the entropy and pairing potential energy. In doing the calculation this way, we have ignored the affect of the pairing energy $\frac{q}{2} V_{\vec{k}}$ on the energy cutoff which bounds the sum. With $\epsilon_c = 50$ the impact is negligible, but for smaller cutoff energies it becomes important.

1.15 Numerical methods

The first step in performing these calculations is to produce the nesting density of states. This is accomplished by extracting a triangulation of the Fermi surface with Fermi velocities from a dispersion relationship expressed on a grid. The nesting density of states integral is converted to a sum and stored in a discrete histogram indexed by $V = \hat{q} \cdot \vec{v}_{\vec{k}_F}$

$$\begin{aligned} N(V,\hat{q}) &= \frac{\Omega_c}{(2\pi)^3}\sum_i \frac{Area_i}{\vec{v}_{Fi}} \\ &\times \Theta(\frac{1}{2}V_\delta - |V - \hat{q}\cdot\vec{v}_{\vec{k}_F i}|) \end{aligned} \tag{1.35}$$

where V_δ is the projected velocity bin width, and i goes over all triangles. The preferred direction for $\hat{q}$ can be found by looking for largest peaks at high V in the nesting density calculated for each of the high symmetry directions.

There is a subtle danger associated with using discrete bins for the nesting density for low temperatures and low Δ. The discrete bins will act like δ functions that will always give a FFLO solution to the gap equation at high fields (see 1D Fermi surface section). However, the temperature and Δ of the possible solutions will go as $exp(-1/N(V_\delta))$ which will typically be on the order of e^{-10}.

To determine the preferred state at a given temperature and applied field, it is necessary to calculate the free energy for each possible state. Furthermore, the possible superconducting states have Δ and q degrees of freedom. Fortunately, the constraint set by holding g constant means that we only need to search 1D isocontours in Δ-q space, which we evaluate on a discrete grid. Finding this isocontour requires that that we perform the integral in Eq. 1.26 many times.

Since we have already discretized $N(V,\hat{q})$, the integral over V becomes a sum. This leaves the energy integral

$$\int_{-\epsilon_c}^{\epsilon_c} \frac{1}{2\sqrt{\epsilon^2+\Delta^2}}(1 - f(E_\uparrow^+) - f(E_\downarrow^+))d\epsilon. \tag{1.36}$$

This is a difficult integral to do numerically since it is highly peaked around $\epsilon = 0$ and the behavior of the Fermi functions is highly temperature dependent. We chose to take advantage of the fact that we know how to do part of the integral analytically.

$$\int \frac{1}{2\sqrt{\epsilon^2 + \Delta^2}} d\epsilon = \frac{1}{2} sinh^{-1}(\frac{\epsilon_b}{\Delta}) \tag{1.37}$$

This allows one to write formally

$$\int_{-\epsilon_c}^{\epsilon_c} \frac{1}{2}(1 - f(E_\uparrow^+) - f(E_\downarrow^+)) d[sinh^{-1}(\frac{\epsilon}{\Delta})] \tag{1.38}$$

This integral was discretized in a manner that allowed dealing with variations in the Fermi functions. The numeric integral becomes

$$\sum_{\epsilon_i} \quad (1 - f(E_\uparrow^+) - f(E_\downarrow^+)) \times \tag{1.39}$$

$$[sinh^{-1}(\frac{\epsilon_i + \epsilon_{step}}{\Delta}) - sinh^{-1}(\frac{\epsilon_i}{\Delta})] \tag{1.40}$$

with the variable step size

$$\epsilon_{step} \propto \left[\frac{\partial}{\partial \epsilon}(f(E_\uparrow^+) + f(E_\downarrow^+)) + \delta\right]^{-1}. \tag{1.41}$$

The constant δ is needed to maintain a minimum step size. This variable step integration is used in calculating contributions to the free energies and other observables of interest.

Chapter 2

Fermi Velocity and Incipient Magnetism in $TiBe_2$

2.1 Introduction

The work in this chapter is derived from the publication

"Fermi velocity spectrum and incipient magnetism in $TiBe_2$"; T. Jeong, A. B. Kyker, W. E. Pickett, *Phys. Rev. B* **73**, 115106 (2006).

The cubic Laves compound $TiBe_2$ was already shown forty years ago to have quite unusual behavior of the magnetic susceptibility $\chi(T)$ and the Knight shift.[31] χ^{-1} showed a strong increase with lowering temperature but a clear deviation from Curie-Weiss form, while the Knight shift was temperature dependent and negative. The magnetic properties of $TiBe_2$ have been controversial since Matthias *et al.*[32] interpreted the susceptibility peak at 10 K in $TiBe_2$ as itinerant antiferromagnetism (AFM) with an associated magnetic moment of $1.64\mu_B$, and Stewart *et al.* reported a transition at 2 K that seemed characteristic of magnetic ordering.

However, a clear picture has emerged gradually after the idea of weak itinerant antiferromagnetism had been abandoned because of the subsequent lack of experimental evidence[33, 34]. Many experiments have shown that $TiBe_2$ is instead a strongly enhanced paramagnet [35, 36, 37] and undergoes a metamagnetic transition[38, 39, 40] (field-driven ferromagnetism) around 5.5 T. Also one can see similarity to the magnetic behavior of Ni_3Ga by comparing the values of the low temperature susceptibility, $\chi = 1.65 \times 10^{-2}$ emu/mole for Ni_3Ga[41] and $\chi = 0.90 \times 10^{-2}$ emu/mole for $TiBe_2$[32]. Based on the magnetization data of Monod *et al*[36] Wohlfarth[39] suggested the transition at 5.5 T should be first order. Wohlfarth's considerations received at least partial support from

theoretical band-structure considerations coupled with the de Haas-van Alphen data of van Deursen *et al*[42].

Clarity began to arise with the extensive experiments of Acker *et al.* who interpreted their magnetization data[35] in fields to 21T and the magnetization data of Monod *et al.* [36] as evidence for exchange-enhanced paramagnetism or spin fluctuations in $TiBe_2$. They found the system $TiBe_{2-x}Cu_x$ to become FM at a critical concentration $x_{cr} = 0.155$. Stewart *et al.*[43] measured the specific heat of $TiBe_2$ ($\gamma = 42$ mJ/mole K^2) at low temperature in 0 and 7T and interpreted the behavior as evidence of spin fluctuations.

The isoelectronic isostructural material $ZrZn_2$ is considered a classic example of an weak itinerant ferromagnet. Magnetic measurements find very small magnetic moments (values from 0.12 to 0.23 μ_B)[44, 45], hence the characterization as a weak ferromagnet. The magnetization of $ZrZn_2$ increases substantially with field, but unlike $TiBe_2$ with its metamagnetic transition, the increase continues smoothly to fields as high as 35 T. The Curie temperature T_C drops approximately linearly with pressure, from 29 K at $P = 0$ to 4K at $P = 16$ kbar, which extrapolates to a quantum critical point (QCP) at $P = 18 - 20$ kbar. The report of superconductivity coexisting with ferromagnetism in $ZrZn_2$ near this QCP[46] enlivened both theoretical and experimental attention, but more recently it has been shown[30] there is no bulk superconductivity. $TiBe_2$, on the other hand, has been nearly addressed only rarely for the past twenty years.

The complex temperature-field behavior of $TiBe_2$ has led to many speculations about the microscopic mechanisms. Of course spin fluctuations play a central part, and

the highly enhanced susceptibility suggests this system is near a quantum critical point (at slightly enlarged lattice constant, say, as well as for the Cu alloying). If FM fluctuations dominate, then a metamagnetic transition (field-driven FM state) around 5 T would make sense. If AFM fluctuations dominate, application of a field suppresses the fluctuations, providing another way to interpret specific heat under applied field.[47] The anomalies in the conduction electron spin resonance (CESR) linewidth[48] around 2 K have been interpreted in terms of a thermal spontaneous magnetism,[49] and a decrease in the resistivity is also seen at that temperature.[35] All of these scenarios are sensitive to the Fermi surface shape, velocity spectrum, and possibly the energy dependence of the density of states near the Fermi energy, and it is these questions that we address in this paper.

Band structure intricacies by themselves also can come into play. Shimizu showed[49] that an independent electron system with magnetic coupling can undergo a first-order transition to a "spontaneous thermal magnetism" state (within a range $T_1 < T < T_2$) if it is highly enhanced and if the Fermi level lies within a local minimum in the density of states. The effects of magnetic fluctuations should of course be added[50] to the free energy of both the ordered and disordered phases to make this treatment more realistic.

Local density approximation (LDA) energy band studies of $TiBe_2$ have been reported previously [51, 52, 53]. Those studies revealed a split narrow peak in in the density of states (DOS) N(E) near the Fermi energy (E_F), with calculated Stoner factors $IN(E_F)$ greater than unity, giving the Stoner instability to FM. Here I is the Stoner

exchange interaction averaged over the Fermi surface. Thus, as for a few cases that have come to light more recently,[54, 55] ferromagnetism is incorrectly predicted, indicating the need to account for magnetic fluctuations not included in LDA that will suppress magnetic ordering. By comparing the calculated value of $N(E_F)$ with the measured susceptibility, a Stoner enhancement $S = [1 - IN(E_F)]^{-1} \approx 60$ was obtained, making $TiBe_2$ a more strongly exchange enhanced metal than Pd.

All of these calculations, carried out 25 years ago, used shape approximations for the density and potential, and for a detailed investigation of the weak ferromagnetism precise electronic structure methods are required. In this work, the precise self-consistent full potential linearized-augmented-plane-wave (FLAPW) method and full potential local orbital minimum basis band structure scheme (FPLO) are employed to investigate thoroughly the electronic and magnetic properties of $TiBe_2$ based on the density functional theory. We compared and checked the calculation results of the both methods. We consider the effect of magnetism on the band structure and Fermi surface, Fermi velocity and compare with experiment and previous band calculations.

2.2 Crystal Structure

$TiBe_2$ crystallizes into a cubic Laves phase C15 crystal structure. The C15 (AB_2) structure is a close packed structure and the site symmetry is high for the two constituents. Ti atoms occupy the positions of a diamond sublattice while the Be atoms form a network of interconnected tetrahedra, with two formula units per cell. Since the major

contributions to $N(E_F)$ come from Ti, the local environment of Ti atoms is particularly important to keep in mind. Each Ti is surrounded by 12 Be neighbors at a distance of 2.66 $\mathring{A}$ and tetrahedrally by four Ti neighbors a distance 2.78 $\mathring{A}$ away. The $TiBe_2$ structure belongs to the Fd3m space group with Ti occupying the $8a$ site, and Be the $16d$ site. The site symmetry of Ti is $\bar{4}3m$(tetrahedral) and Be has $\bar{3}m$ site symmetry. The atomic positions are symmetry determined, and we used experimental lattice constant 6.426 $\mathring{A}$ for all calculations.

2.3 Method of Calculations

We have applied the full-potential nonorthogonal local-orbital minimum-basis (FPLO) scheme within the local density approximation (LDA).[56] In these scalar relativistic calculations we used the exchange and correlation potential of Perdew and Wang.[57] Ti $3s, 3p, 4s, 4p, 3d$ states and Be $2s, 2p, 3d$ were included as valence states. All lower states were treated as core states. We included the relatively extended semicore $3s, 3p$ states of Ti as band states because of the considerable overlap of these states on nearest neighbors. This overlap would be otherwise neglected in our FPLO scheme. Be 3d states were added to increase the quality of the basis set. The spatial extension Of the basis orbitals, controlled by a confining potential $(r/r_0)^4$, was optimized to minimize the total energy.

The self-consistent potentials were carried out on a mesh of 50 k points in each direction of the Brillouin zone, which corresponds to 3107 k points in the irreducible zone.

A careful sampling of the Brillouin zone is necessary to account carefully for the fine structures in the density of states near Fermi level E_F. For the more delicate numerical integrations, band energies were extracted from FPLO in an effective mesh of 360 k points in each direction. A separate tool was developed to extract energy isosurfaces with gradients from the scaler energy grid. The isosurfaces were then used to calculate density of states and velocity moments.

To check carefully the fine structure that we will discuss, we also repeated several calculations with the general potential linearized augmented plane wave (LAPW) method,[29] as implemented in the WIEN2K code.[58] Relativistic effects were included at the scalar relativistic level. However, we verified that the magnetic moment with the experimental structure is not sensitive to the inclusion of the spin-orbit interaction. For the generalized gradient approximation (GGA) calculations, we used the exchange-correlation functional of Perdew, Burke, and Ernzerhof. [59] We choose the muffin-tin spheres $R_{MT} = 2.6$ a.u. for Ti, $R_{MT} = 2.1$ a.u. for Be and a basis set determined by a plane-wave cutoff of $R_{MT}K_{max} = 7.0$, which gives good convergence. The Brillouin zone samplings were done using the special k point method with 1280 points in the irreducible zone.

2.4 Results and Discussions

For orientation we first show the full nonmagnetic band structure of $TiBe_2$ in Fig. 2.1, which is consistent with earlier calculations of [51, 52, 53]. The Be $2s$ bands

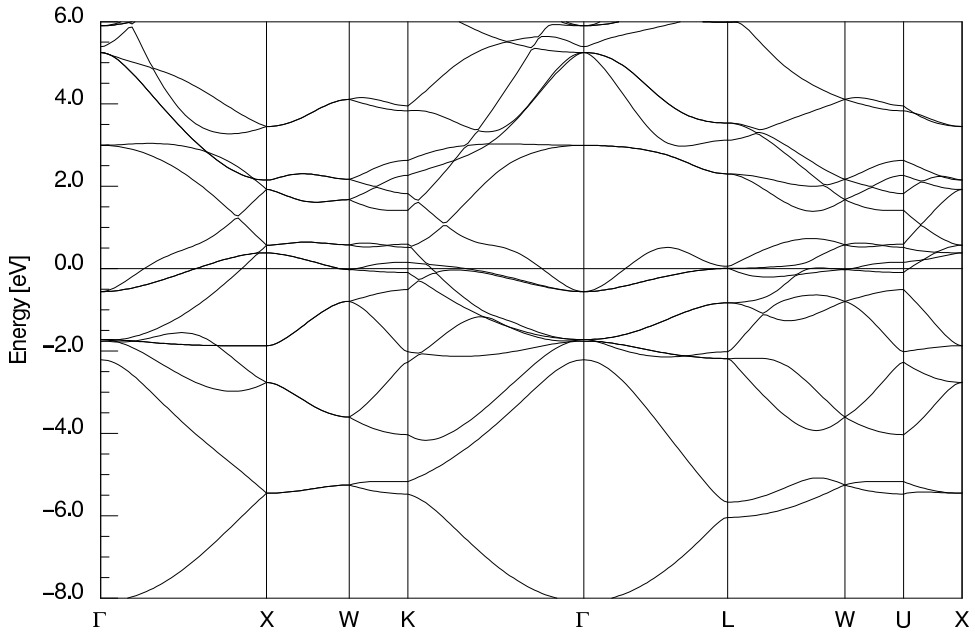

Figure 2.1. The full LDA band structure of non-magnetic $TiBe_2$ along symmetry lines showing that there are several bands near the Fermi level (taken as the zero of energy) with weak dispersion; they are primarily Ti $3d$ in character.

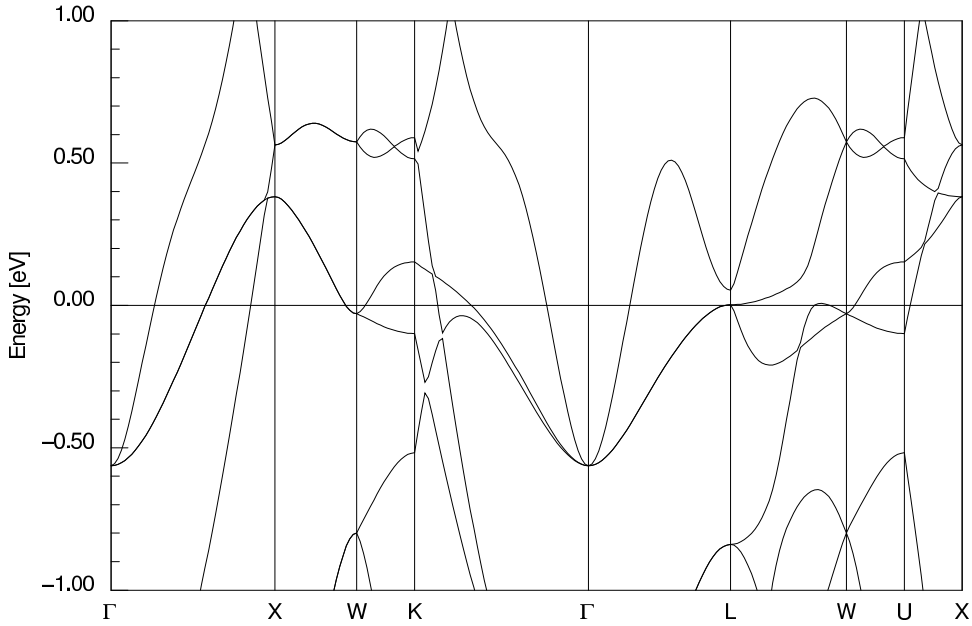

Figure 2.2. Band structure of non-magnetic $TiBe_2$ of Fig. 2.1 on an expanded scale near Fermi level. The flat bands along L-W-U/K-L lines (the hexagonal face of the fcc Brillouin zone) give rise to the density of states structure discussed in the text.

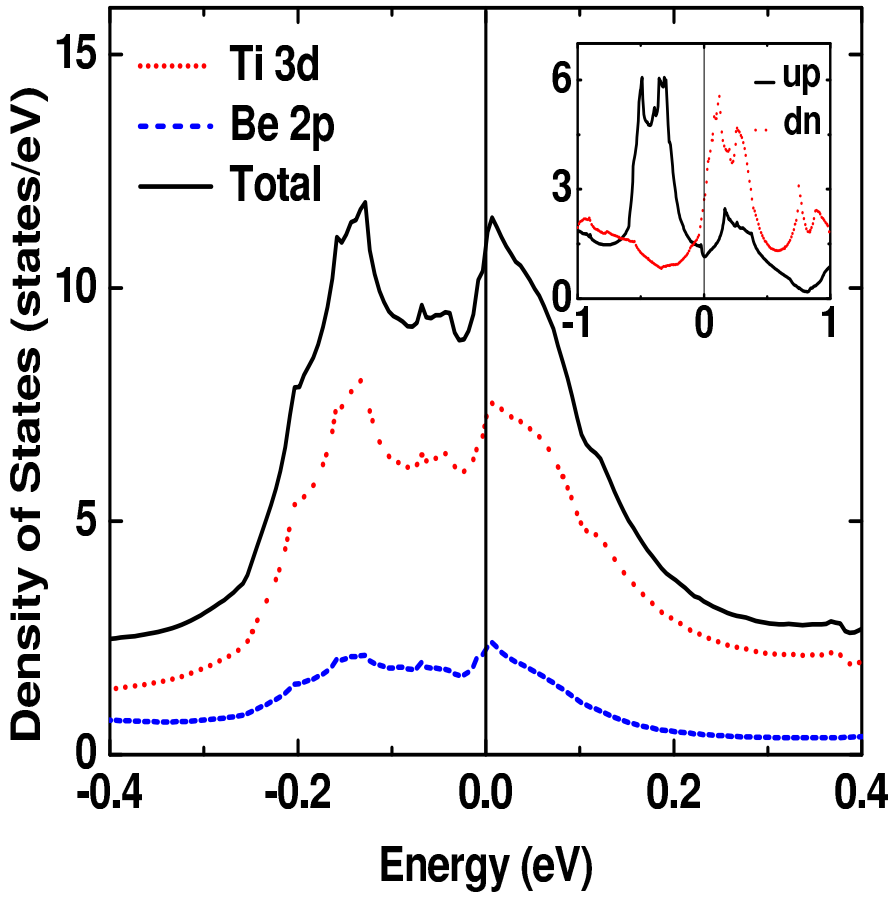

Figure 2.3. The total and atom-projected density of states (Ti, short dashed line; Be, the lower, long dashed line) for non-magnetic $TiBe_2$ per primitive cell. The inset gives the density of states for the ferromagnetic $TiBe_2$ showing the exchange splitting 0.6 eV. The peak of the DOS for the majority spin is entirely below the Fermi level while that of the minority spin is above the Fermi level.

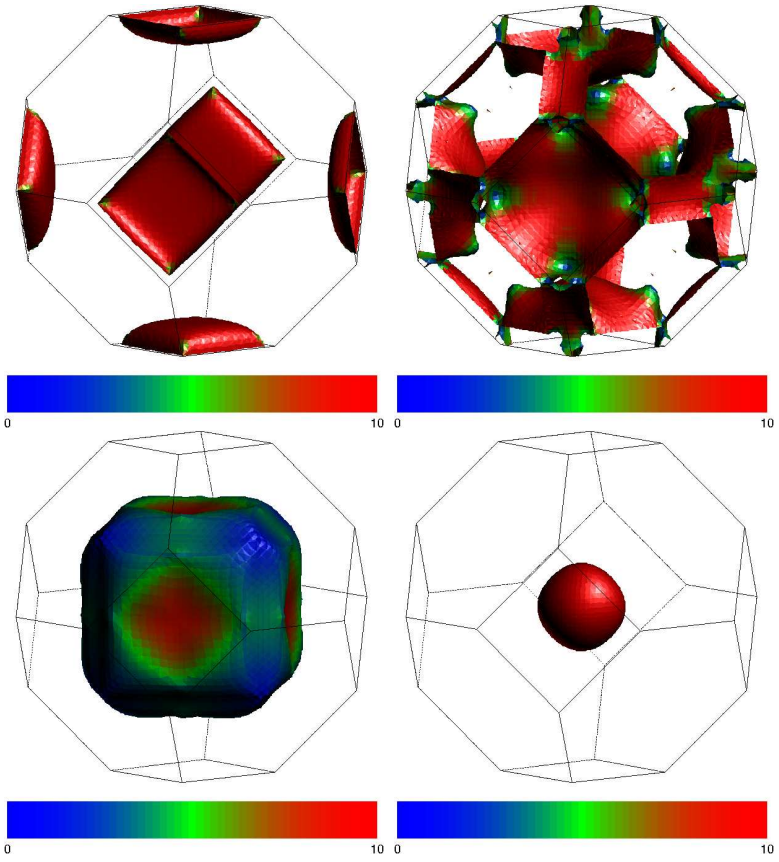

Figure 2.4. Fermi surfaces, top left: band 14, X-centered pillows; top right: band 15, primarily X-centered jungle gym; bottom left: band 16, Γ-centered pseudocube; bottom right: band 17, Γ-centered sphere. Fermi velocities colored dark (red) for lowest to lighter (blue) for highest. Magnitudes of velocities are discussed in Sec. IV.A.

lie between -8 eV and -2 eV. Above them the bands are of mixed s, p character, centered on the Be as well as the Ti site. Near the Fermi level there are several bands with weak dispersion, being of primarily Ti $3d$ character. The bands at K and L are hybridized strongly, while at X the s, p character is the main character. As noted also by Jarlborg and Freeman,[51, 52] one band at L falls extremely close to E_F (3 meV below). This band is doubly degenerate along Γ-L, and the L point forms the maximum of band 15 and a saddle point for band 16. As the Fermi energy rises (for added electrons, say) the Fermi surface sweeps through the L point saddle, where the band has a vanishing velocity by symmetry. This vanishing velocity is discussed below. There is another doubly degenerate band very near E_f at the W point.

The density of states (DOS) is shown near E_F in Fig. 2.3. The Fermi energy E_F falls extremely close to the edge of a very narrow peak in the DOS. The DOS peak arises from Ti d bands hybridized with Be p states. Flat bands close to Fermi level centered mostly in regions near the L-W-U and W-K directions, *i.e.* the hexagonal faces of the Brillouin zone, cause the sharp peak. Stewart *et al.*[43] measured the linear specific heat coefficient for $TiBe_2$ of γ=42 mJ/K^2 mole-formula unit. The calculated value of $N(E_F)$=5.33 states/eV/f.u. for $TiBe_2$ corresponds to a bare value γ_o=12.6 mJ/K^2 mole(formula unit), leading to a thermal mass enhancement $1+\lambda$=3.3, or λ=2.3 arising from phonons, magnetic fluctuations, and Coulomb interactions.

Density functional calculations are usually reliable in calculating the instability

to ferromagnetism. The enhanced susceptibility[60] is given by

$$\chi(T) = \frac{\chi_0}{1 - N(E_F)I} \equiv S\chi_0. \tag{2.1}$$

where $\chi_0 = \mu_B^2 N(E_F)$ is the bare susceptibility obtained directly from the band structure and I is the Stoner exchange interaction constant. Here $N(E_F)$ refers to both spins, and hence forward we quote susceptibility in units where $\mu_B \equiv 1$. The calculation of I is from fixed spin moment calculations[61], in which the energy $E(m)$ is calculated subject to the moment being constrained to be m. The behavior at small m is $E(m) = (1/2)\chi^{-1}m^2$ from which $I = 0.22$ eV can be extracted from Eq. 2.1. This value of I gives $IN(E_F) = 1.2$, larger than unity and very close to that calculated earlier,[52] corresponding to a Stoner ferromagnetic instability.

As for a few other compounds, $TiBe_2$ is incorrectly predicted by LDA to be ferromagnetic. Since spin-orbit coupling is small in $3d$ magnets, we neglect it, so the direction of magnetic polarization is not coupled to the lattice. We have calculated a consistent magnetic moment for $TiBe_2$: $0.97\mu_B$/f.u.(FPLO, LDA), $1.00\mu_B$/f.u.(LAPW, LDA), $1.10\mu_B$/f.u.(LAPW, GGA). This value is considerably larger than an earlier calculation[51] (which also reported a much smaller value for $ZrZn_2$ than obtained from more recent calculations[62]). We address the overestimate of the tendency to magnetism below.

2.4.1 Fermi Surface and Fermi Velocity

In Fig. 2.4 we show the nonmagnetic Fermi surfaces shaded by the Fermi velocities. The position of E_F near L and W points sensitively determine the exact shape of

some Fermi surfaces. The shapes can be characterized as (a) small Γ-centered electron sphere from band 17, (b) large Γ-centered electron pseudocube from band 16, (c) multiply connected surface mostly enclosing holes around the X point from band 15, which we refer to as the jungle gym, and (d) flat hole pillows centered at each of the three X points. The doubly degenerate bands crossing E_F along Γ-X and X-W guarantee touching of certain surfaces along these lines.

The DOS peak at and above E_F is due to the band near the L point where the cube-shaped surfaces are about to form bridging necks. Figure 2.5 shows how the Fermi velocity spectrum ($N(V;E)$) changes with energy at the peak just above E_F, at E_F, and at the first minimum below E_F. The Fermi velocity spectrum is defined as

$$\begin{aligned} N(V;E) &= \sum_{\vec{k}} \delta(E_{\vec{k}} - E)\delta(V_{\vec{k}} - V) \\ &= \int_{\mathbf{L}(V;E)} \frac{d\mathbf{L}_k}{|\vec{v}_k \times \nabla_k |\vec{v}_k||}, \end{aligned} \tag{2.2}$$

with normalization $\int N(V;E)dV = N(E)$. Here $\mathbf{L}(V;E)$ is the line of intersection of the constant energy $E_k = E$ surface with the constant velocity surface $|\vec{v}_k| = V$. The gradient of the velocity in the denominator makes this distribution delicate to calculate accurately. $N(E,V)$ was calculated numerically by extracting a triangulated energy isosurface from the band structure, then obtaining a velocity histogram of the states associated with the isosurface.

The spectrum in Fig. 2.5 shows, at E_F, velocities extending down to the very low value of 2×10^6 cm/s, and up to 5×10^7 cm/s, a variation of a factor of 25. Roughly half of the weight lies below 10^7 cm/s. At the van Hove singularity at +3 meV, the only

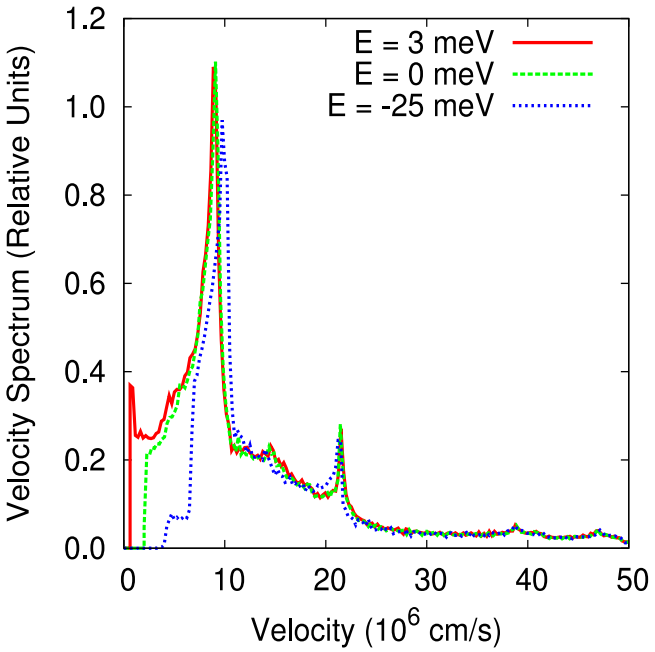

Figure 2.5. Fermi velocity spectrum of $TiBe_2$. The low Fermi velocity states are the primary source of changes to the density of states.

noticeable difference is additional velocities extending down to zero due to the vanishing velocity at L (we have not worried about reproducing the $V \to 0$ behavior precisely). At -25 meV, which is just below the narrow peak at E_F, the strong weight in the spectrum appears only at 7×10^6 cm/s. Note that there is very little change in the high velocity spectrum over small changes in energy.

2.5 Analysis of Velocity Distribution and Susceptibility

2.5.1 Renormalization due to Spin Fluctuations

Following the work of Larson, Mazin, and Singh[63] for Pd which builds on Moriya theory, we first attempted to identify the relevant band characteristics in order to

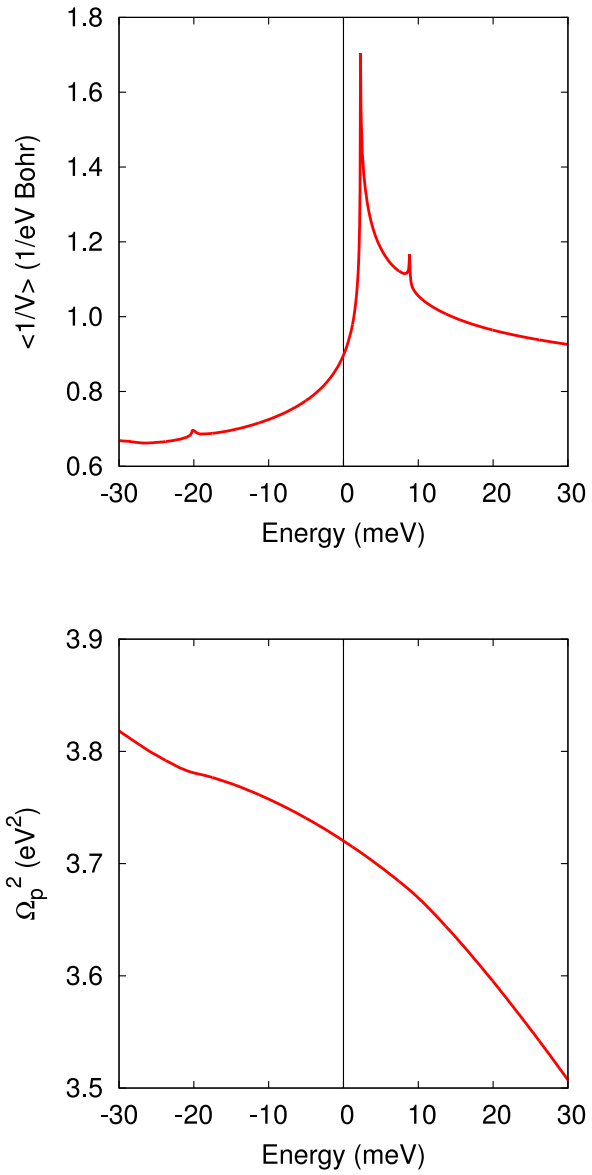

Figure 2.6. Top panel: $< \frac{1}{v(E)} >$ plotted versus energy, showing the square root divergence of the inverse moment of velocity near the Fermi energy. Unit conversion is: 1 eV Bohr = $8{\times}10^6$ cm/s. Bottom panel: the graph of the second moment of velocity (with constants included to show it as the square of the Drude plasma energy) is concave downward, which gives rise to the negative value of the Moriya A parameter. This sign of A is verified by the calculation of $\chi(q)$ at small q (see text).

evaluate the spin fluctuation reduction of χ in $TiBe_2$. For this, one begins with the bare susceptibility in the small q and small ω limit, given by

$$\chi_0(\vec{q},\omega) = N(E_F)[1 - A(\frac{qa}{2\pi})^2 + i\frac{1}{2} < \frac{1}{v} >_F \frac{\omega}{q}], \tag{2.3}$$

while the screened susceptibility using the RPA approximation is given by

$$\chi^{-1}(\vec{q},\omega) = \chi_0^{-1}(\vec{q},\omega) - I. \tag{2.4}$$

The Moriya parameter $A = -1.8$, expressed in dimensionless form here, and mean inverse Fermi velocity $< 1/v >_F \equiv v_F^{-1}$ (the second Moriya parameter, discussed below) are derived from velocity moments and DOS of the band structure, and like the density of states, they are greatly influenced by the Fermi surface topology and its velocity spectrum. Specifically, changes in topology which give rise to points of zero velocity in the band structure near the Fermi surface become an important factor. The mean inverse Fermi velocity which governs the imaginary part of $\chi_0(\vec{q},\omega)$ is given by

$$< \frac{1}{v(E)} > \equiv v^{-1}(E) = \sum_k \frac{\delta(\varepsilon_k - E)}{|\vec{v}_k|} / \sum_k \delta(\varepsilon_k - E) \tag{2.5}$$

evaluated at E_F. The difference between $< v^{-1} >_F$ and $1/< v >_F$ is one measure of the velocity variation of the Fermi surface. The bottom or top of a three-dimensional band (corresponding to the appearance or vanishing of a Fermi surface) gives only a discontinuity proportional to the square of the band mass. At a saddle point, such as the merging of the corners of the pseudocube Fermi surfaces, $v^{-1}(E)$ undergoes a $1/\sqrt{E - E_{cr}}$ divergence because the associated Fermi surface area does not vanish. This "van Hove singularity" in $v^{-1}(E)$ is evident for the band edge 3 meV from E_F in $TiBe_2$ in Fig. 2.6. We calculated $1/v_F^{-1} = 5 \times 10^6$ cm/s for $TiBe_2$.

For cubic structures, the parameter A in Eq. 2.3 is given by

$$\begin{aligned} A &= \frac{1}{48\pi e^2}(\frac{2\pi}{a})^2 \frac{d^2\Omega_p^2(E_F)}{dE_F^2} \\ \Omega_p^2(E_F) &= \frac{4\pi e^2}{3}\sum_k \vec{v}_k^2 \delta(\varepsilon_k - E_F) \\ &\equiv \frac{4\pi e^2}{3} N(E_F) v_F^2. \end{aligned} \tag{2.6}$$

Thus A it is proportional to the second derivative of the square of the Drude plasma energy Ω_p (*i.e.* $\hbar$ is absorbed into Ω_p, so Ω_p here explicitly has energy units; k sums are understood to be normalized over the zone). The second moment of velocity is finite everywhere, but its second derivative is not (for example, for free electrons this diverges as the band edge). Derivatives have the unfortunate property of amplifying noise in numerical evaluations. We have addressed the noise issue by using a large number of k points in the numerical integration (360× 360× 360). By fitting $\Omega_p(E)^2$ with a polynomial near the Fermi energy, we obtain the above-mentioned value $A = -1.8$. The Fermi velocity was calculated to be $v_F = 2.3$ eV bohr = 1.8 $\times 10^7$ cm/s.

2.5.2 q-dependent Susceptibility

The negative value of the A parameter indicates, from Eq. 2.3, that the primary magnetic instability in $TiBe_2$ does *not* lie at q=0 but rather at finite q, so it is more susceptible to AF instability (including possibly a spin spiral) rather than ferromagnetic. The sign of A has been verified independently by explicit calculation of the real part of $\chi(\vec{q})$, with results shown in Fig. 2.7.

The calculation of $\chi_{\alpha,\beta}(\vec{q})$ between bands α and β was performed by an isosurface

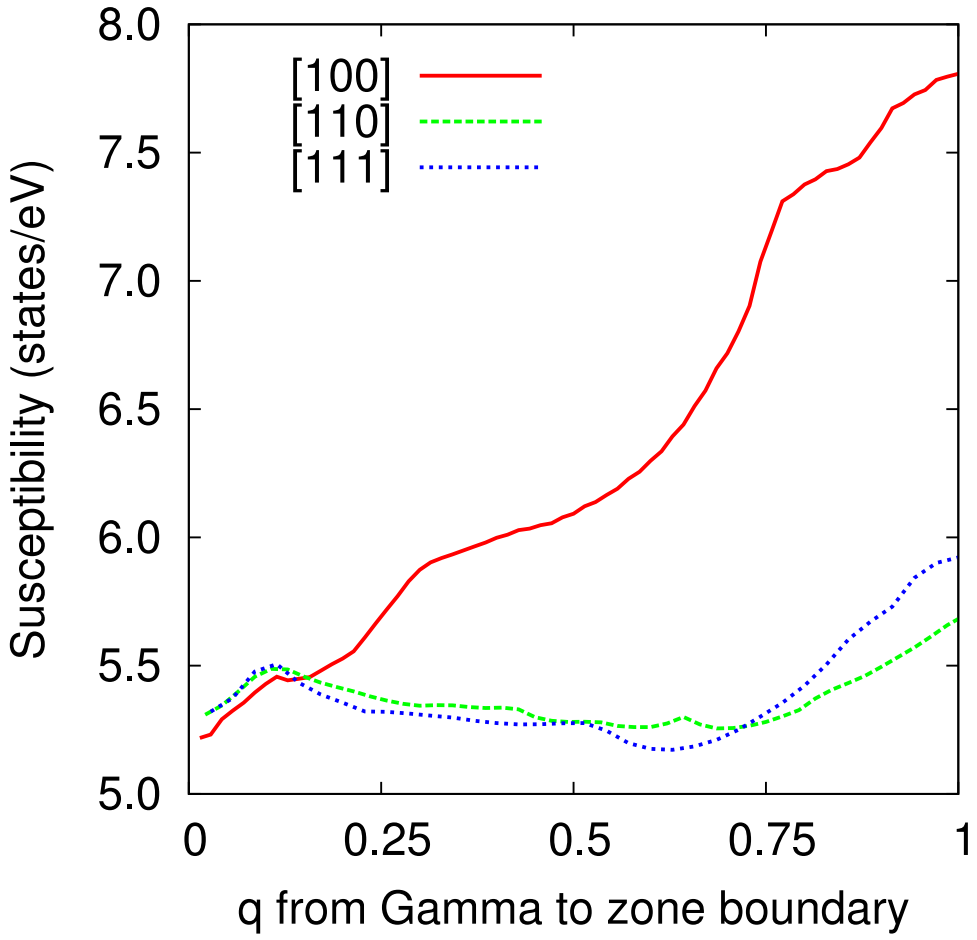

Figure 2.7. Intraband contribution to the real part of $\chi(\vec{q})$. The increase at small q confirms the sign of Moriya A coefficient (see text). Although both [110] and [111] directions have a maximum at the zone boundary, the peak along [100] (X point of the zone) dominates the instability.

slicing method. The susceptibility can be written, after inserting a factor $1 \equiv \int d\Delta\ \delta(\Delta - \epsilon_{\beta,\vec{k}+\vec{q}} + \epsilon_{\alpha,\vec{k}})$, as

$$\begin{aligned} \chi_{\alpha\beta}(\vec{q}) &= \int d\Delta \frac{N^{\chi}_{\alpha\beta}(\Delta)}{\Delta}, \\ N^{\chi}_{\alpha\beta}(\Delta) &= \sum_{k} [f(\epsilon_{\alpha,\vec{k}}) - f(\epsilon_{\beta,\vec{k}+\vec{q}})]\delta(\Delta - \epsilon_{\beta,\vec{k}+\vec{q}} + \epsilon_{\alpha,\vec{k}}), \end{aligned} \tag{2.7}$$

where $N^{\chi}_{\alpha\beta}(\Delta)$ is a susceptibility density calculated from the isosurface defined by the Fermi functions and the energy δ function. The Brillouin zone was divided into a $140 \times 140 \times 140$ grid of cubes. Within each cube the Δ integral is calculated as a discrete sum, using variable step sizes in Δ corresponding to 1/30 of the maximum difference in energies $\epsilon_{\beta,\vec{k}+\vec{q}} + \epsilon_{\alpha,\vec{k}}$ within the cube.

The susceptibility rises equally along all three symmetry directions (as required by cubic symmetry), but only for $\hat{q}$ along the cubic axis does $\chi(\vec{q})$ continue to increase strongly beyond the small-q region. The maximum of $\chi_o(\vec{q})$ occurs at the X point, where the intraband part has increased by nearly 50% over its q=0 value. In such cases where q=0 is not the maximum, it is necessary to apply the extension of weak ferromagnets to the AF case.[64]

The band-by-band contributions to $\chi_o(q)$ have been evaluated both to verify the code and to identify the source of the important contributions and structures. The sphere FS gives rise to a Lindhard type form with $2k_F \approx \pi/a$ (but is not perfectly round). The pillows lead to a cusp for $(q_x, 0, 0)$ for $q_x \approx 0.28\pi/a$, and along all three directions decreases for $q \geq \pi/a$. For the jungle gym and the pseudocube,χ increases by a factor of two at the zone boundary along $(q_x, 0, 0)$, with much less variation in the other two directions. The

contributions to N(E_F) from each of the bands is: sphere, 1.4%; pillows, 7%; jungle gym, 33%; pseudocube, 58%.

Away from q=0 the interband contributions to $\chi(q)$ contribute, and it is known in other transition metals and their compounds that the $\vec{q}$-dependence of matrix elements can be important. We have calculated also the interband $\chi(\vec{q})$ for several bands around the Fermi level, finding that they contribute a broad maximum at intermediate $|q|$. It seems unlikely, however, that interband contributions will move the maximum away from the X point.

Peaking of $\chi(\vec{q})$ at the zone boundary implies a short wavelength $\lambda = a$ AF instability (incipient, since no AF phase is observed). With the fcc lattice and two Ti atoms in the primitive cell, there several possibilities for the most unstable mode, which will involve antialignment of spins or charge density wave variation, but also may involve noncollinear alignment of the spins. We have tried to obtain a $q = 0$ AF state within LDA, with atomic moments antialigned on the bipartite Ti lattice, but the moment vanished when this was tried. We have not investigated possible $\vec{q} =$ X point AF states.

2.5.3 Temperature Dependence of Susceptibility

The high narrow peak in the DOS near E_F suggests an explanation of the T-dependence of χ mentioned in the Introduction, or at least part of it. To understand what part arises from simple thermal smearing, we have evaluated

$$N(E,T) \equiv \int_{-\infty}^{\infty} [-\frac{\partial f(E-\mu(T))}{\partial E}] N(E) dE, \tag{2.8}$$

where the chemical potential $\mu(T)$ is adjusted at each temperature to keep the number of electrons (occupied states) constant. The result is shown as a series of curves for T ranging from zero to 300 K. It is necessary to include the variation in μ, and the value of $N(\mu(T), T)$ decreases by 8%.

The resulting change in the physical, enhanced susceptibility is given by

$$\chi(T) = \frac{N(\mu(T); T)}{1 - IN(\mu(T); T)}. \tag{2.9}$$

Adjusting I to reproduce the peak height (at 10 K, experimentally), which requires I=0.183 eV (S=56 at the maximum of $N(\mu)$), the resulting enhanced $\chi(T)$ is compared with the data in the lower panel of Fig. 2.8. It is evident that this simple temperature smearing accounts for much of the observed temperature dependence. Additional indirect temperature smearing will come from phonons and from electronic and magnetic interactions as these excitations are increasingly excited upon raising the temperature. We conclude that $TiBe_2$ contains no appreciable contribution to the susceptibility from local moments.

2.5.4 Field Dependence of Susceptibility

For an energy-dependent DOS and a highly enhanced susceptibility, a field-dependent susceptibility $\chi(H, T = 0) \equiv \chi(H)$ is expected. In $TiBe_2$ a strong effect of this kind has been seen, which can be characterized as field-driven ferromagnetism. The differential susceptibility $\chi_d(\mathbf{H}) = \mathbf{dM}(\mathbf{H})/\mathbf{dH}$ where M is given by the difference in electron occupations $n_\sigma(H)$. A many-body treatment shows that the spin imbalance can be expressed[66] in terms of the spin-dependent thermal (energy E surface averaged) Green's

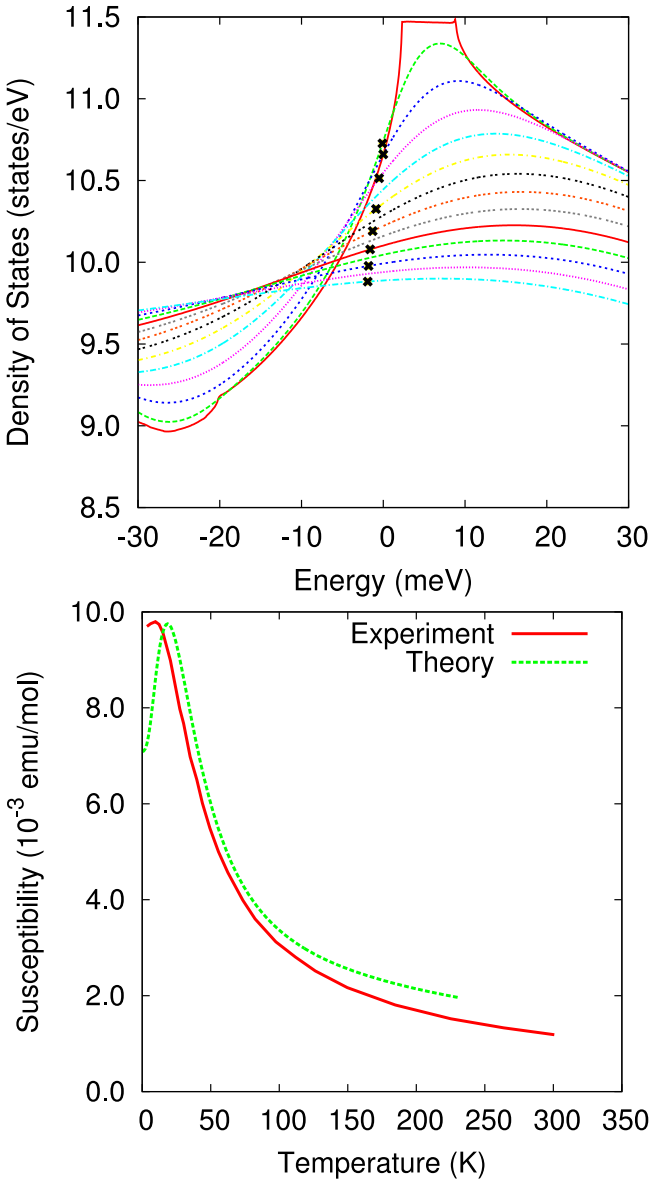

Figure 2.8. The upper graph shows how the density of states near the Fermi energy changes from T=0 to T=300K. The lower graph shows the experimental susceptibility[65] compared to theory. The Stoner I has been adjusted slightly from the calculated value to match the susceptibility maximum.

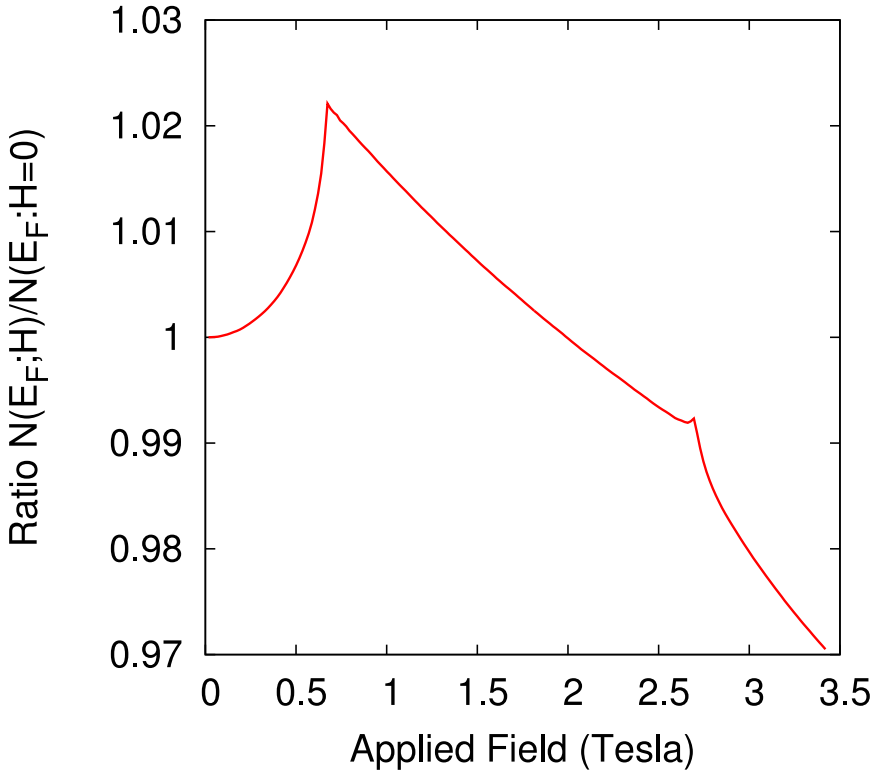

Figure 2.9. Magnetic field (H) dependence of the Fermi level density of states for $TiBe_2$, referred to its H=0 value, as defined in the text. The initial increase with field indicates an increasing instability towards ferromagnetic order.

function

$$\begin{aligned} G_\sigma(E, i\omega_n; H) &= \frac{1}{i\omega_n - (E - \mu - \sigma\mu_B H) - \Sigma_\sigma(H)}, \\ n_\sigma(H) &= \int dE N(E) T \sum_i G_\sigma(E, i\omega_n; H) e^{i\omega_n \eta}, \end{aligned} \tag{2.10}$$

here ω_n is the fermionic Matsubara discrete energy variable and η is a positive infinitesimal. The simplest form of (Stoner) self-energy $\Sigma_\sigma = \sigma K \mu_B H$ should be appropriate ($1 + K = S$).

Taking the field derivative of $\mathbf{M}(H)$ but keeping H finite, and using (in this approximation)

$$G_\sigma(E, i\omega_n; H) = G_\circ(E - \sigma\mu_B(1 + K)H, i\omega_n; H = 0) \tag{2.11}$$

we obtain the result at zero temperature

$$\begin{aligned} \chi_d(H) &= \frac{d\mathbf{M}(H)}{d(\mu_B H)} \\ &= S\big[N(E_F - S\mu_B H) + N(E_F + S\mu_B H)\big]. \end{aligned} \tag{2.12}$$

This clearly reduces to the usual T=0 result at H=0. A slightly better treatment would have also some H-dependence of S due to the structure in $N(E)$ and the delicate situation here that $IN(E_F)$ is approaching unity, but at this point we neglect such details.

The result for the relative correction

$$\mathbf{R} = \frac{N(E_F - S\mu_B H) + N(E_F + S\mu_B H)}{2N(E_F)} \tag{2.13}$$

is shown in Fig. 2.9. The effect on the ratio (thus on the differential susceptibility) is clear, however even with the factor of S=60 enhancement of the energy scale ($\mu_B H \to S\mu_B H$)

the peak occurs at a field one order of magnitude smaller than seen in experiment. This difference seems to indicate that the field influence on the spin fluctuations dominates; however the variation in N(E) will need to be accounted for in any quantitative explanation.

2.6 Summary

The complex and sometimes confusing data on the enhanced paramagnet were discussed in the Introduction. It seems clear that magnetic fluctuations will be required to understand the underlying mechanisms. Here we have presented a precise calculation and analysis of the electronic structure, especially focusing on the Fermi surfaces and velocity spectrum at and near the Fermi level that underlies not only the single particle excitations but also the spectrum of magnetic fluctuation in the itinerant limit, which clearly seems to be the case in $TiBe_2$.

Our calculations have confirmed the sharp structure in the density of states around the Fermi level that had been noted earlier, and quantified the tiny energy scale that is involved: the Fermi level lies in a region of steep DOS, just 3 meV from an abrupt van Hove singularity. This singularity is derived from a doubly degenerate band at the L point of the zone. We have shown how to calculated the spectrum of velocities (speeds) over the Fermi surface, and find the spectrum to be peaked at (the low value of) 10^7 cm/s, with much of the weight below that value. Moriya theory for weak ferromagnets requires, for the imaginary part of the inverse susceptibility, the moment $< 1/v_F >$; we have

illustrated that $1/v(E)$ diverges at the van Hove singularity signaling possible problems with applying Moriya theory to $TiBe_2$.

Moriya theory for weak ferromagnets also requires the dimensionless quantity $A \propto d^2\Omega_p(E)/dE^2$ at the Fermi energy, where Ω_p is the conventional transport Drude energy. We find that this quantity is not positive, as it must be for an incipient ferromagnet; rather it is negative indicating the dominating (nearby) magnetic instability is finite q: antiferromagnetic, spin wave, spin spiral, etc. Direct calculation of the generalized susceptibility $\chi_o(q)$ confirms the sign of A, and reveals the dominant instability to lie at the X point of the Brillouin zone, making $TiBe_2$ an incipient antiferromagnet.

We have shown that the sharp structure in $N(E)$ has other consequences. First, it leads to a T-dependent chemical potential. Together with the temperature broadening of $N(E)$ and the Stoner enhancement $S \approx 60$, this simple temperature broadening can account for most if not all of the temperature dependence of the susceptibility, which some investigators had interpreted as Curie-Weiss-like. As a result, the occurrence of local moments in $TiBe_2$ can be ruled out. Similarly, we have shown that this sharp structure in $N(E)$, again together with the large Stoner enhancement, has a substantial effect on the field-dependence of the differential susceptibility. There is still the question of how much of the measured field dependence is due to this induced exchange splitting, and how much is due to the effect of the field on the magnetic fluctuations.

Many of the results we have obtained here are strongly dependent on details of the band structure and the position of the Fermi level. That these results reflect realistically the mechanisms underlying the many fascinating observations obviously requires that the

band structure formalism is applicable in detail to such systems and that the calculations are accurate. Another requirement is that of high sample quality, that the stoichiometry is precise and that defect concentration must be very low (simple impurity broadening will affect behavior). These questions must be addressed in deciding whether to press onward to a more complete and more challenging explanation that includes effects of both magnetic fluctuations and the energy dependence of the density of states.

Chapter 3

Macroscopic Theory of Multi Order Parameter Pairing in Superconductiity

3.1 Multi Order Parameter Landau Theory

The Ginzburg-Landau theory has been a very successful phenomenological model for describing orbital effects of superconductors. The theory correctly captures many of the observed phenomena associated with the superconducting state including zero-resistance, the Meissner effect, the Abrikosov vortex and vortex lattice arrangement, penetration depth, coherence length, etc.

The Ginzburg-Landau generic theory is based on Landau's generic theory of second order phase transitions. Landau assumed that the free energy of a system is an analytic function which shares the symmetry of the Hamiltonian, and a second order phase transition occurs when a symmetry of the system is spontaneously broken. The free energy density is written as

$$F = F_N + F_L(m) \tag{3.1}$$

where F_N is the normal free energy density and F_L is the condensate free energy density. An order parameter is introduced which is usually indicates the condensate density and how the condensate breaks the symmetry. F_L is Taylor expanded in terms of the order parameter. In general, the order parameter has the dimension and field of the broken symmetry, for brevity however I will only considering the breaking of a one dimensional real symmetry such as a classical Ising model with no applied field. Taking the first two non-zero terms, the Taylor expansion of F_L becomes

$$F_L(m) = \alpha m^2 + \frac{1}{2}\beta m^4 \tag{3.2}$$

where m is the order parameter representing the magnetization. Since the sign of m is a symmetry of the Hamiltonian, only even powers are included in the Taylor expansion. As long as $m = 0$ the system state also has inversion symmetry. As soon as m takes on a finite value, it will have a definite sign and the inversion symmetry of the state will be broken.

Assuming the axiom that the system will assume the state that minimizes the free energy and that the order parameter is bounded, one must assume that β is greater than zero. If α is also greater than zero, $m = 0$ minimizes $F_L(m)$. If α is less than zero, the optimal value of m is found to be

$$m = \pm\sqrt{\frac{-\alpha}{\beta}} \tag{3.3}$$

by minimizing $F_L(m)$ with respect to m^2. Thus the phase transition occurs when α changes sign. α is normally taken to be a function of temperature expanded around the critical temperature

$$\alpha = C(T - T_c) \tag{3.4}$$

where $C = d\alpha/dT$ evaluated at T_c.

In general, a system may have many order parameters which may be coupled by the Hamiltonian. For example consider two coupled Ising systems with order parameters m_1 and m_2 which might be used to model two magnetic domains with some interaction. The free energy density is

$$F = F_N + F_L \tag{3.5}$$

$$F_L = F_{L1}(m_1) + F_{L2}(m_2) + F_{L12}(m_1, m_2) \tag{3.6}$$

The $F_{L1}(m_1)$ and $F_{L2}(m_2)$ contributions are still restricted to even powers. The $F_{L12}(m_1, m_2)$ may have odd powers as long as all terms are zero when m_1 and m_2 are zero. I will only consider two terms: bi-quadratic and bi-linear. The Taylor expansion becomes

$$\begin{aligned} F_L &= \alpha_1 m_1^2 + \frac{1}{2}\beta_1 m_1^4 + \alpha_2 m_2^2 + \frac{1}{2}\beta_2 m_2^4 \\ &+ D m_1^2 m_2^2 + J m_1 m_2 \end{aligned} \tag{3.7}$$

Initially at high temperatures when both order parameters are zero, there are two symmetries of the Hamiltonian to be broken. The breaking of these symmetries could result in one phase transition, or two phase transitions.

Assuming that $T_{c1} \neq T_{c2}$ and $J = 0$, the bi-quadratic coefficient D will not change the upper critical temperature. The lower critical temperature will be raised or lowered depending depending on the sign of D. To maintain the finite values of the order parameters at the energy minimum, D must be bounded in the negative direction by

$$D > -\sqrt{\beta_1 \beta_2} \tag{3.8}$$

A sufficiently large positive value of D will reduce the lower critical temperature to zero, eliminating the second phase transition entirely.

Assuming that $T_{c1} \neq T_{c2}$ and $D = 0$, the bilinear coefficient J will always raise the upper critical temperature. The new upper critical temperature occurs when the following equality is satisfied

$$J^2 = \alpha_1 \alpha_2 \tag{3.9}$$

with both α_1 and α_2 positive. Below the new upper critical temperature, both symmetries

are broken in a single phase transition.

3.2 Ginzburg-Landau Theory

An early attempt at a phenomenological description of the interaction of magnetism and superconductivity was developed by F. London. The London equation [22]

$$\vec{J_s} = -\frac{m^*}{n_s^* e^{*2}} \vec{A} \tag{3.10}$$

can be derived by applying the quantum mechanical current operator to a condensate with a fixed phase and magnitude over a macroscopic region. This fixed phase can be thought of as breaking a phase symmetry of the Hamiltonian. This differs from the non-condensate where the electron phases are uncorrelated. By assuming a specific gauge for $\vec{A}$, the equation captures the observed phenomena of the Meissner effect including a finite penetration depth. It however does not address the upper critical field. Even more disturbing, it only works for one choice of the $\vec{A}$ gauge.

The Ginzburg-Landau theory of superfluid condensates [67] assumes a complex condensate wave function

$$\Psi(\vec{r}) = |\Psi(\vec{r})| e^{i\theta(\vec{r})} \tag{3.11}$$

to be used as the order parameter in a Landau second order treatment. Assuming a complex field for the order parameter allowed for a quantum mechanical kinetic energy term to be added to the free energy density. This kinetic energy term has the property of coupling the supercurrents to the $\vec{A}$ field, as in the London equation, and placing an energy cost on the supercurrents that must be balanced by the energy lowering of the condensate.

Assuming that carriers are pairs and including a term for the magnetic energy, the Ginzburg-Landau free energy density is

$$F = F_N + \alpha|\Psi|^2 + \frac{1}{2}\beta|\Psi|^4 + \frac{1}{4m}|(-i\hbar\nabla + 2z\vec{A})\Psi|^2 + \frac{B^2}{2\mu_0} \tag{3.12}$$

where m and z are the mass and charge of an unpaired carrier. The condensate density is given by $|\Psi^2|$. The order parameter Ψ, the magnetic field and the condensate coefficients may be spatially dependent. Even though the phase of $\theta(\vec{r})$ is not fixed, $\theta(\vec{r})$ for a connected condensate is completely defined by the density and current up to a global phase factor.

The Ginzburg-Landau non-linear partial differential equations are derived by minimizing the free energy using the Euler-Lagrange method. Minimizing with respect to the vector potential gives the differential equation

$$\frac{\delta F}{\delta \vec{A}(\vec{r})} = \vec{R}_A = \frac{iz\hbar}{2m}(\Psi^*\nabla\Psi - \Psi\nabla\Psi^*) + \frac{2z^2}{m}|\Psi|^2\vec{A} + \frac{\nabla^2\vec{A} - \nabla\cdot\vec{A}}{\mu_0} \tag{3.13}$$

Minimizing with respect to the order parameters gives

$$\frac{\delta F}{\delta \psi(\vec{r})} = R_\Psi = \alpha\Psi + \beta|\Psi|^2\Psi + \frac{1}{4m}(-i\hbar\nabla + 2z\vec{A})^2\Psi \tag{3.14}$$

It is customary to assume a gauge where $\nabla\cdot\vec{A} = 0$, but numerically this can be inconvenient to maintain. In the absence of applied currents or electric potentials, $\vec{R}_A$ and R_Ψ will be zero at a local maximum or minimum of the energy. In time dependant Ginzburg Landau theory [68][69], $\vec{R}_A$ and R_Ψ will be proportional to the time derivative of $\vec{A}$ and Ψ respectively. Because the Ginzburg-Landau equations are non-linear, solutions are not guaranteed to be unique. This can easily be demonstrated by noting that $\Psi = 0$ and

$\nabla \times \nabla \times \vec{A} = 0$ will always be a solution even when the energy can be lowered by forming a condensate. The number of stationary points is greatly increased when the possibility of vortex trapping and pinning is considered. In the numerical simulations, $\vec{R}_A$ and R_Ψ will be used as a residue and and may be modified to enforce boundary conditions.

Because the Ginsburg-Landau equations are a phenomenological theory, the coefficients α and β are used as material fitting parameters to match the penetration depth (ξ_{GL}) and coherence length (λ_{GL}).

A magnetic field experiences an exponential decay as it penetrates into a superconducting half space. If one assumes a fixed condensate density defined by the equilibrium value $n_s = -\beta/\alpha$ when $\alpha < 0$, the penetration depth is found from the vector GL equation to be

$$\lambda_{GL} = \sqrt{\frac{m}{2\mu_0 e^2 n_s}} = \sqrt{\frac{-\beta m}{2\mu_0 e^2 \alpha}} \tag{3.15}$$

which matches the London result.

The coherence length is characterized by a competition between the kinetic energy and potential energy as defined by the complex GL equation. Due to the cubic Ψ term, the order parameter does not rise as an exponential. In the small Ψ limit where it can be treated as an exponential, the coherence length is found to be

$$\xi_{GL} = \sqrt{\frac{\hbar^2}{-\alpha 4m}} \tag{3.16}$$

The Ginzburg-Landau parameter, κ, is the ratio of penetration depth to coher-

ence length

$$\kappa = \sqrt{\frac{2\beta m^2}{\hbar^2 \mu_0 e^2}} \tag{3.17}$$

Type I superconductors have a $\kappa < \sqrt{2}$. Most of the low T_c superconductors such the mono-atomic superconductors fall into this category. Type II superconductors have a large κ and include the more complex higher T_c superconductors. The Abrikosov vortex lattice[70] occurs in type II superconductors.

The Ginzburg-Landau theory is intended to describe second order phase transitions. It has been noted that field induced quenching of type I superconductors is a first order phase transition [71]. This first order transition occurs when the applied field is strong enough to cause the normal to superconducting domain wall to retreat. Ginzburg-Landau captures this critical field behavior.

3.3 Multi-Order Parameter Ginzburg-Landau Theory

Multi-order parameter Ginzburg-Landau theories have arisen in recent years to address multi-gap superconductors such as MgB_2 [72] [73] and the theoretical of superconductivity and superfluidity in highly compressed Hydrogen [74].

The modified Ginzburg-Landau free energy density consists of a sum of kinetic energy and uncoupled potential energy terms that are directly from the original Ginzburg-Landau free energy plus cross coupling potential energy terms[75] .

$$\begin{aligned} F &= F_N + \sum_\nu \left(\alpha_\nu |\Psi_\nu|^2 + \frac{1}{2}\beta_\nu |\Psi_\nu|^4 \right) + \sum_\nu \left(\frac{1}{4m_\nu} |(-i\hbar\nabla + 2z_\nu \vec{A})\Psi_\nu|^2 \right) + \frac{B^2}{2\mu_0} \\ &+ \frac{1}{2}\sum_{\nu\neq\mu} \left(\gamma_{\nu\mu} |\Psi_\nu|^2 |\Psi_\mu|^2 + \sigma_{\nu\mu}\Psi_\nu \Psi_\mu^* \right) \end{aligned} \tag{3.18}$$

A superconducting pair is assumed to have a mass of $2m_\nu$ and a charge of $2z_\nu$. The cross coupling potential includes the density-density ($\gamma_{\nu\mu}$) and complex Josephson ($\sigma_{\nu\mu} = \sigma_{\mu\nu}^*$) coupling terms. The Josephson term must be equal to its complex conjugate on exchange of indices to guarantee a real energy. Higher order terms are possible but do not add significant new behavior in a small order parameter expansion.

The Ginzburg-Landau equations are derived by minimizing the free energy using the Euler-Lagrange method again. Minimizing with respect to $\vec{A}$ gives

$$\vec{R}_A = \sum_\nu \left(\frac{iz_\nu \hbar}{2m_\nu} (\Psi_\nu^* \nabla \Psi_\nu - \Psi_\nu \nabla \Psi_\nu^*) + \frac{2z_\nu^2}{m_\nu} |\Psi_\nu|^2 \vec{A} \right) + \frac{\nabla^2 \vec{A} - \nabla \cdot \vec{A}}{\mu_0} \tag{3.19}$$

Minimizing with respect to the order parameters gives

$$\begin{aligned} R_\nu &= \alpha_\nu \Psi_\nu + \beta_\nu |\Psi_\nu|^2 \Psi_\nu + \frac{1}{4m_\nu}(-i\hbar\nabla + 2z_\nu \vec{A})^2 \Psi_\nu \\ &+ \sum_\mu \left(\gamma_{\nu\mu} |\Psi_\mu|^2 \Psi_\nu + \sigma_{\mu\nu} \Psi_\mu \right) \end{aligned} \tag{3.20}$$

Unlike the multi-order parameter Landau equations which become two independent condensates when the cross coupling potential terms are zero, the electromagnetic vector potential, $\vec{A}$, will couple the two condensates in the presence of any currents or B fields.

A possible rationale for the Josephson term is pair hopping between condensates. The phase of the Josephson term will only have physical significance if a method exists to couple to both order parameters through a Josephson junction or other phase sensitive probe. The density-density term may arise due to competition between condensates for available carriers.

3.4 Solving the Ginzburg-Landau Model

The Ginzburg-Landau equations are non-linear partial differential equations that can only be solved analytically for special cases. It is therefore common to consider numerical solving methods [76][77][78]. Qiang Du has written a good review article of these methods [79]. I have chosen a finite element grid method and a finite difference scheme for evaluating the derivatives. The order parameter is stored in Cartesian components for ease of update and to avoid the multiple value problems that arise with a polar representation. The $\vec{A}$ field is stored as a two or three element vector depending on the spatial dimension of the model being considered. A local applied current vector and applied scalar potential will also be included.

As pointed out earlier, the residues $\vec{R}_A$ and R_Ψ from equations 3.13 and 3.14 are proportional to the time derivative of the $\vec{A}$ field and order parameters. This suggests a simple recursive method for finding a stationary point by making small corrections to the state variables proportional to the residues. Using the notation where $|X)_n$ refers to the state of X at step n evaluated at all points on the grid, this method can be written as

$$\begin{aligned} |\vec{A})_{n+1} &= |\vec{A})_n + \eta_A |\vec{R}_A)_n \\ |\Psi)_{n+1} &= |\Psi)_n + \eta_\Psi |R_\psi)_n \end{aligned} \tag{3.21}$$

The update parameters η_A and η_Ψ must be small enough to maintain stability. If correct time dependent behavior is desired, the ratio η_A/η_Ψ must be a constant set by the relative stiffness of the $\vec{A}$ field and the order parameters. Individual update parameters may be needed when multiple condensates are considered.

Choosing the update parameters can be difficult. If the values are to low, the solution takes longer than necessary to find. If they are to large, the system becomes unstable. To minimize the time it take to find a solution and maintain stability, I use an approximate Newton's method. The non-time dependent Newton's method can be written as

$$|A,\Psi)_{n+1} = |A,\Psi)_n - \eta J_n^{-1}|R_A, R_\Psi)_n \tag{3.22}$$

where J_n^{-1} is the inverse of the Jacobian of the residues.

The size of the Jacobian makes producing its inverse impractical, however for small $|A|$ the coupling between R_A and R_Ψ is reduced and the Jacobian becomes diagonally dominate allowing the Jacobian to be approximated by its diagonal elements. The simplified Newton's method becomes:

$$\begin{aligned} |A)_{n+1} &= |A)_n - \eta \tilde{J}_A^{-1}|R_A)_n \\ |\Psi_{n+1}) &= |\Psi)_n - \eta \tilde{J}_\Psi^{-1}|R_\Psi)_n \\ \tilde{J}_A(\vec{r}) &= \left(\frac{\partial R_A(\vec{r})}{\partial A(\vec{r})}\right) \\ \tilde{J}_\Psi(\vec{r}) &= \left(\frac{\partial R_\Psi(\vec{r})}{\partial \Psi(\vec{r})}\right) \end{aligned} \tag{3.23}$$

The value of η must be less than one for stability, and the optimal value was found to be around 0.9. In theory, instability should not occur until $\eta > 1$, but finite sampling adds systematic noise which can increase the gain for high frequencies making a lower value necessary.

In any fixed gauge the maximum of $|\vec{A}|$ grows linearly with the size of the system. In order to keep the off diagonal elements of the Jacobian minimal, I use a local gauge

transformation $-2z\delta\vec{A} = \hbar\delta\nabla\Psi$ at each point on the grid to force $\vec{A} = 0$ [77]. It is still necessary to maintain a global gauge to guarantee a single value of the A field.

3.5 Boundary Conditions and Simulation Controls.

The external B field is assumed to always be applied in the $\hat{z}$ direction. In the two dimensional simulations, this is perpendicular to the plane. In the three dimensional simulations, this is along an axis of the grid. The field could either be applied as a constant flux or as a constant intensity around the border of the simulation.

In the constant flux case, a line integral around the edge of the simulation in a plane perpendicular to the $\hat{z}$ direction is held constant. In this case, when the superconductor expels the magnetic field the flux gets concentrated at the edges of the simulation. This is a useful property for determining the critical field needed to quench superconductivity or insert vortices.

External currents are imposed directly on the vector residue R_A. R_A is in units and one of its terms is equilivent to Ampre's law relating the $\vec{A}$ field to the total current.

$$J_{total} = -\frac{\nabla^2\vec{A} - \nabla\cdot\vec{A}}{\mu_0} \tag{3.24}$$

This is not the same as driving a current into the superconductor, but instead is a way to apply non-uniform magnetic fields. See Fig. 3.1 for an example. Inhomogeneity such as pinning sites or Josephson junctions were modeled by making spatially dependent adjustments to the linear Taylor coefficient α. Applied voltage differences is modeled by imposing a small differential phase shift at every simulation update step. This was generally applied

to a subset of the simulation to investigate Josephson junction behavior.

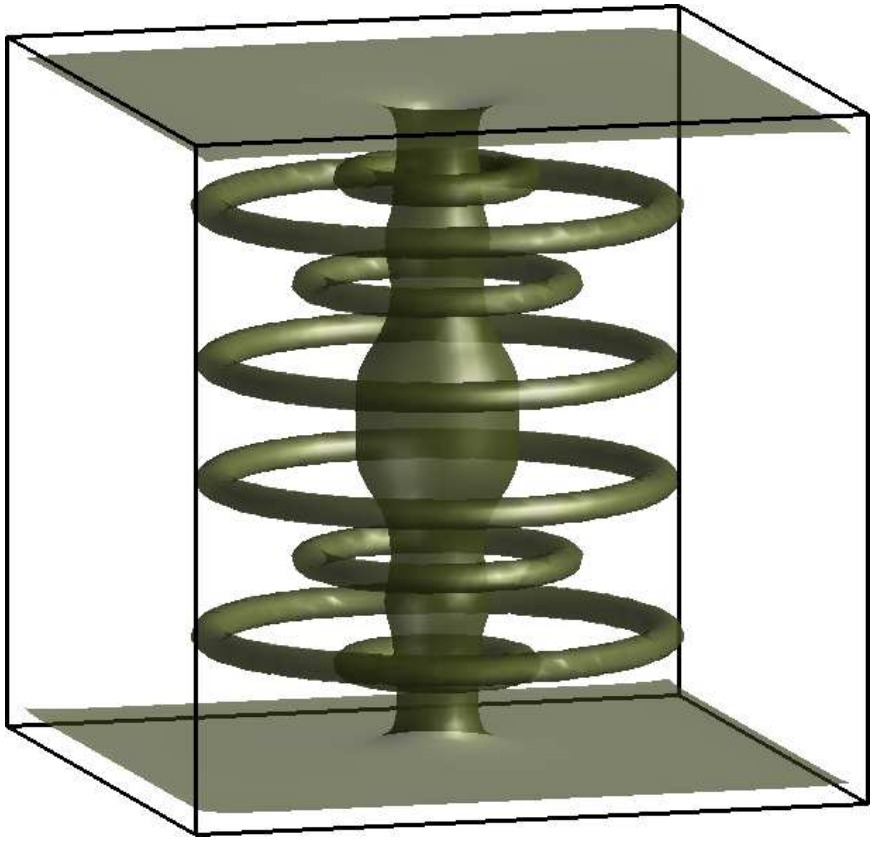

Figure 3.1. This is an image from a three dimensional simulation where the iso-surface value is taken to be 1/2 the maximum value. A large current is applied in the $\hat{z}$ direction through the center of the simulated cube. This current induces a circular magnetic field that would go as $1/r$ in the absence of the superconductor. The magnetic field near the current is greater than H_{c2} driving the order parameter to zero (indicated by the central column). When the magnetic field reaches H_{c1}, vortex rings are induced into the superconductor. The rings will attempt to form a tight packing arrangement.

3.6 The Vortex

The Abrikosov vortex[70] is a topological excitation that is associated with multi-valuedness of the complex order parameter. Consider any closed directed path. If one considers the complex order parameter to be represented by real and imaginary parts, then the following equality must hold

$$\Psi_{stop} = \Psi_{start} + \oint d\vec{l} \cdot \nabla\Psi \tag{3.25}$$

since a closed path must start and stop at the same point. If one considers a polar notation where $\Psi = \psi e^{(i\theta)}$, then one finds a weaker requirement on the phase θ of Ψ

$$\theta_{stop} = \theta_{start} + \oint d\vec{l} \cdot \nabla\theta + n_v 2\pi \tag{3.26}$$

where the vortex or winding number n_v can be any integer. Assuming the underlying superconductor is simply connected and $n_v = 1$, the closed path can be shrunk through a continuous transformation without changing the vortex number. This implies that $\nabla\theta$ is going up and correspondingly the contribution to the kinetic energy from $\nabla\theta$ will also be going up. To balance this, magnitude of the order parameter, ψ, must go down. Figure 3.2 is from a simulation of a single vortex in a long prism shaped superconductor that is isotropic in the long direction. The order parameter goes to zero at the center of the vortex and becomes non-analytic. The finite size grid and finite difference methods cannot completely capture the behavior of the exact center of the vortex.

The reduction of the order parameter in the center of a vortex costs energy. If a vortex exists in a part of the superconductor where the magnitude of the order parameter

has a gradient, the vortex will experience a force in the opposite direction of the gradient. This effect is responsible for vortex pinning by defects in superconductors.

Since a vortex is a topological excitation, it can exist in both type I and type II superconductors. In type II superconductors, the penetration depth is greater than the coherence length. This causes the interactions between vortices and between a vortex and the superconductor boundary to be dominated by the magnetic field and kinetic energy of the currents. The energy density of the magnetic field is

$$E_B \propto (\vec{B}_1 + \vec{B}_2)^2 = \vec{B}_1^2 + \vec{B}_2^2 + 2\vec{B}_1 \cdot \vec{B}_2 \tag{3.27}$$

The force pushing the vortices apart will come from the dot product. The kinetic energy from the currents is more complex since current interactions will increase the energy density on one side of the vortex and decrease it on the other, but the resulting force is proportional to the same dot product. In the Abrikosov vortex lattice, the field associated with each vortex points in the same direction causing them to repel each other. The interactions will be short range due to the finite penetration depth. If vortices are in a disordered state, the cosine associated with the dot product causes the interactions to range from repulsion to attraction.

In type I superconductors, the penetration depth is less than the coherence length. This causes the interactions to be dominated by the magnitude of the order parameter. In this case, the energy is minimized by overlapping the areas where the order parameter is suppressed. The resulting force between vortices is attractive which makes vortex arrays unstable in type I superconductors.

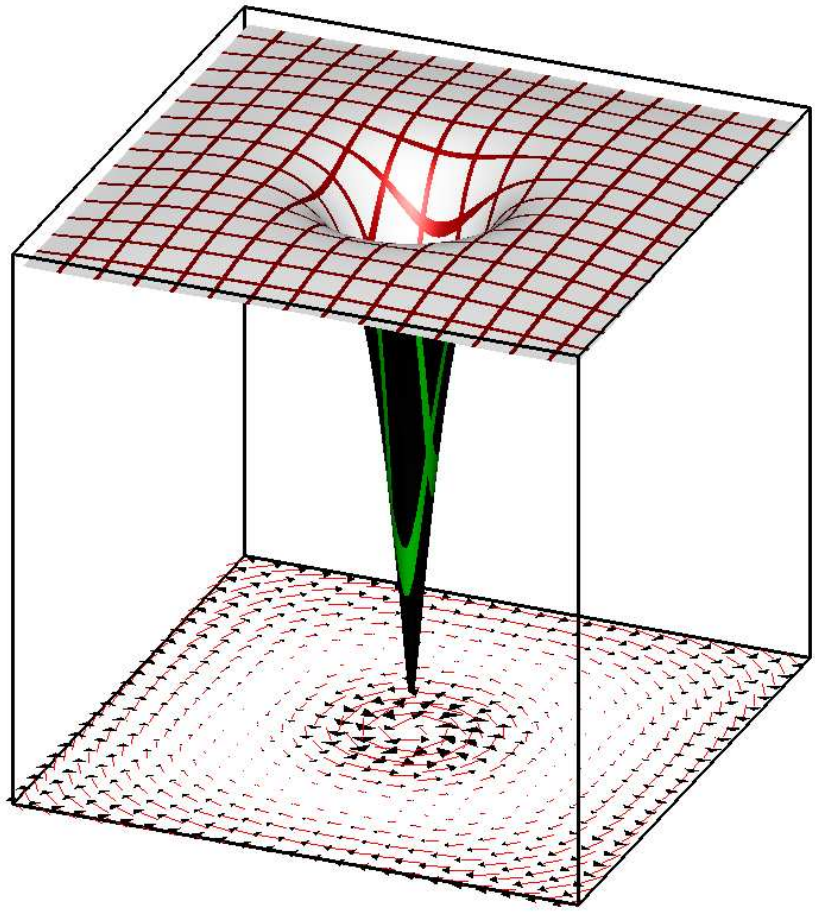

Figure 3.2. A long prism shaped superconductor that is isotropic in the long direction can be simulated as a two dimensional cross section (grid = 120x120). The magnitude of the order parameter in the cross section is represented by the height of the surface from the bottom of the bounding cube. The level at the top of the cube corresponds to the equilibrium value $\Psi_0 = \sqrt{-\alpha/\beta}$. A single vortex has been placed in the center to illustrate the suppression of the order parameter toward the center of the vortex. The supercurrent is represented by arrows at the bottom of the cube. An external applied field induces a Meissner current that travels in the opposite direction of the vortex current. The counter rotating currents produce a path around the vortex where no current is flowing.

3.7 Flux quantization of one order parameter

One important feature of the superconducting vortex, the quantization of the magnetic field, was predicted by F. London. Referring to Fig. 3.2 again, one can see a region around the vortex where the net current is zero. Using the quantum mechanical current operator, the zero current condition can be written

$$J_s = \frac{z\hbar}{m}\nabla\theta|\Psi|^2 - \frac{2z^2}{m}|\Psi|^2\vec{A} = 0 \tag{3.28}$$

Solving for $\vec{A}$ the performing a closed line integral around the vortex gives

$$\oint d\vec{l}\cdot\vec{A} = \frac{\hbar}{2z}\times\oint d\vec{l}\cdot\nabla\theta = \frac{\hbar}{2z}\times 2n\pi \tag{3.29}$$

where n is an integer. The line integral of $\vec{A}$ gives the enclosed flux resulting in a flux quantum defined by $\Phi_0 = \hbar\pi/z$.

In three dimensions, it is not always possible to find a path where the current goes to zero even though the flux per vortex is still quantized. For example, Fig. 3.3 contains two vortices which are not running parallel but are within a penetration depth of each other. Because the vortices are not parallel, the currents will not exactly cancel between them. Many penetration depths away, the current is effectively zero, therefore a line integral in circling both vortices but far removed will enclose two flux quanta. Isolating a single flux quanta requires relaxing the path requirement such that $d\vec{l}\cdot\vec{J}_s = 0$. Thus the original current equation 3.28 can be rewritten

$$d\vec{l}\cdot J_s = d\vec{l}\cdot\frac{z\hbar}{m}\nabla\theta|\Psi|^2 - d\vec{l}\cdot\frac{2z^2}{m}|\Psi|^2\vec{A} = 0 \tag{3.30}$$

which gives the same result as the $\vec{J}_s = 0$ condition for flux quantization.

In some situations this relaxed condition cannot be satisfied. In the case of a vortex ring whose radius is on the order of the penetration depth, there is no path through the center of the ring that satisfies the relaxed condition $d\vec{l}\cdot\vec{J}_s = 0$. For another example of failed flux quantization, consider again Fig. 3.2. If there were no externally applied field, and the penetration depth is on the order of the size of the superconductor, the vortex induced supercurrents would extend all the way to the edge. When the order parameter goes to zero outside the superconductor, $\vec{J}_s$ goes to zero, however the requirement that $\oint d\vec{l}\cdot\nabla\theta = \frac{\hbar}{2z}\times 2\pi$ no longer applies. In the presence of a current, the calculation for the enclosed flux includes a line integral of the current

$$B_{flux} = n\Phi_0 - \frac{m}{z\hbar}\oint d\vec{l}\cdot J_s \tag{3.31}$$

where n is the vortex number.

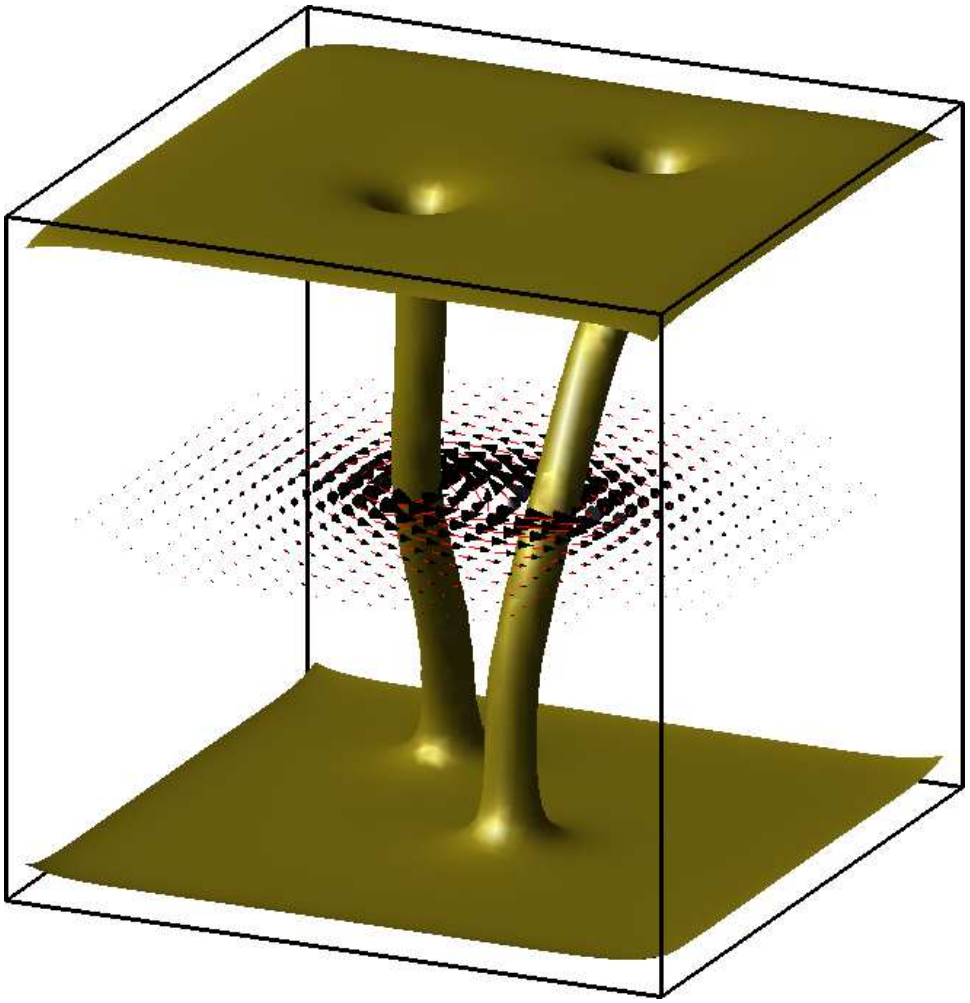

Figure 3.3. A section from a three dimensional simulation containing two vortices in a non-equilibrium configuration (grid = 60x60x60). The surface is an iso-surface of the order parameter at the value $\Psi_0/2$. Each tubes encloses a vortex core where the order parameter vanishes. The current vector in a plane is represented with cones. The current quickly goes to zero away from the vortices but does not go to zero between them. Because they are not parallel, the current will have a vertical component when the X and Y components cancel.

3.8 Fractional flux quantization with two order parameters

Even without the explicit cross coupling terms, the order parameters are coupled through the $\vec{A}$ field. The easiest way to understand the order parameter interactions is by considering the topology of vortices in two dimensional systems. In the single order parameter case with a single isolated vortex, the magnetic field is maximum at the center of the vortex and exponentially decays going away from the vortex center. Outside the vortex core where the magnetic field is zero, the current is also zero. See Fig. 3.4.

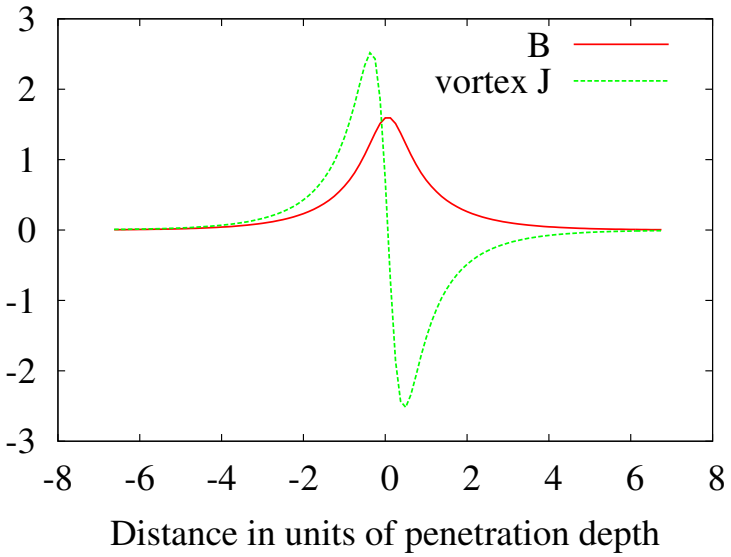

Figure 3.4. The B field and supercurrent along a line perpendicular to a vortex in a single order parameter superconductor simulation The vortex core is located at the zero of the graph, and the sign of the current indicates a current flowing into the page (positive) or out of the page (negative). The current and the field both go to zero exponentially quickly.

The total supercurrent for a two order parameter superconductor is

$$J_s = \frac{2z_1^2}{m_1}|\Psi_1|^2(\frac{\hbar}{2z_1}\nabla\theta_1 - \vec{A}) \tag{3.32}$$

$$+ \frac{2z_2^2}{m_2}|\Psi_2|^2(\frac{\hbar}{2z_2}\nabla\theta_2 - \vec{A}) \tag{3.33}$$

where it is assumed that $J_s = 0$ in the interior of the superconductor well away from any vortices. If both order parameters form pairs of co-axial vortices, and z_1 and z_2 have equal magnitudes, both contributions to the supercurrent will be zero well outside of the vortices. The flux quanta for each co-axial pair will be the same as the single order parameter case.

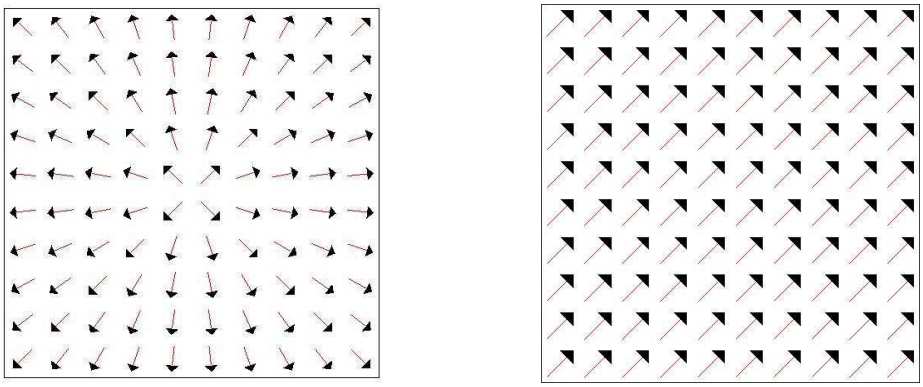

Ψ_1 with one vortex Ψ_2 with no vortex

Figure 3.5. Order parameter phase graphs for a patch of superconductor. The arrows represent the phase of the order parameter as an angle in the plane, and do not represent any real space directions. Well outside the vortex core, the $\vec{A}$ field will a value that cancels the total current.

If the vortex only exists in one of the order parameters, a kind of gauge frustrations results. See Fig. 3.5. The magnetic field and net current both experience the

exponential decay when moving outside the vortex core, but the individual currents asymptotically approach complementary values that decrease as $1/r$. See Fig. 3.6.

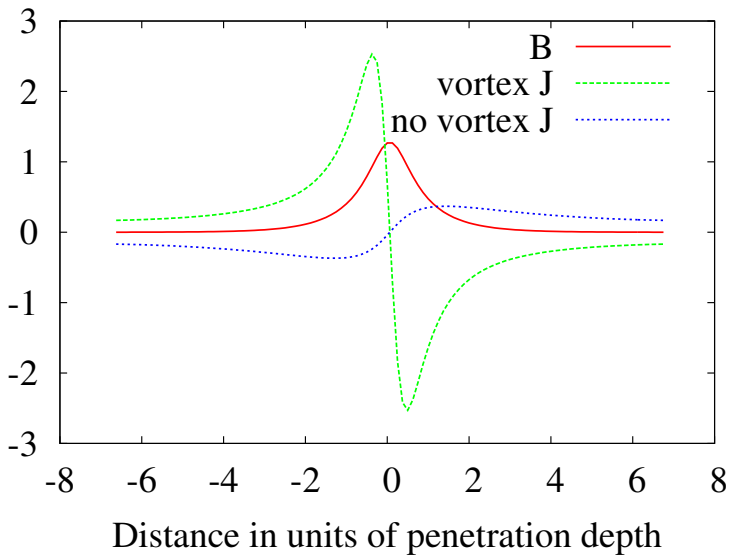

Figure 3.6. The B field and supercurrent components along a line perpendicular to a vortex in a two order parameter superconductor simulation. The vortex core is located at the zero of the graph, and the sign of the current indicates a current flowing into the page (positive) or out of the page (negative). While the net current and the field both go to zero exponentially, the components of the individual currents decrease as $1/r$.

This can be understood by considering the two order parameter current operator when the net current is zero, and assume a gauge where $\vec{A} = 0$ at the center of the vortex. If the vortex exists in order parameter 1 then $\nabla\theta_1 \propto 1/r$. Since order parameter 2 does not have a vortex $\nabla\theta_2 = 0$. The non-zero flux contained in the vortex implies a radially directed $\vec{A}$ that also goes as $1/r$. However no single $\vec{A}$ can individually zero out both the contributions to the current. The total flux contained in the vortex is

$$\Phi_1 = \frac{\frac{2z_1\hbar\pi}{m_1}|\Psi_1|^2}{\frac{2z_1^2}{m_1}|\Psi_1|^2 + \frac{2z_2^2}{m_2}|\Psi_2|^2}. \tag{3.34}$$

Due to the $1/r$ current density, the energy associated with a unpaired vortex grows logarithmically with the size of the system. If the system contains a vortex pair that have been separated due to thermal fluctuations or other mechanism, the energy will grow logarithmically with the separation. This will produce a long range attractive force that goes as $1/r$. There will also be an angle dependence that goes as

$$\vec{F} \propto -\hat{B}_1 \cdot \hat{B}_2 \tag{3.35}$$

where $\hat{B}_x$ is a convenient way to indicate the direction the vortex, but it is not intended to indicate that this force is from the magnetic energy..

3.9 The bi-quadratic term

A rationalization for the bi-quadratic term, $\gamma_{\nu\mu}|\Psi_\nu|^2|\Psi_\mu|^2$, is a competition between the two condensates for carriers. One example could be two FFLO phases with different pair momentum.

It is possible for the bi-quadratic term to be large enough that it prevents the coexistence of both phases. In this case the superconductor will phase separate. If one of the condensates is energetically favorable, it will completely dominate. Since the dominant order parameter would be suppressed in the center of a vortex, it is possible for the subordinate phase to exist in the core of a vortex. See Fig. 3.7

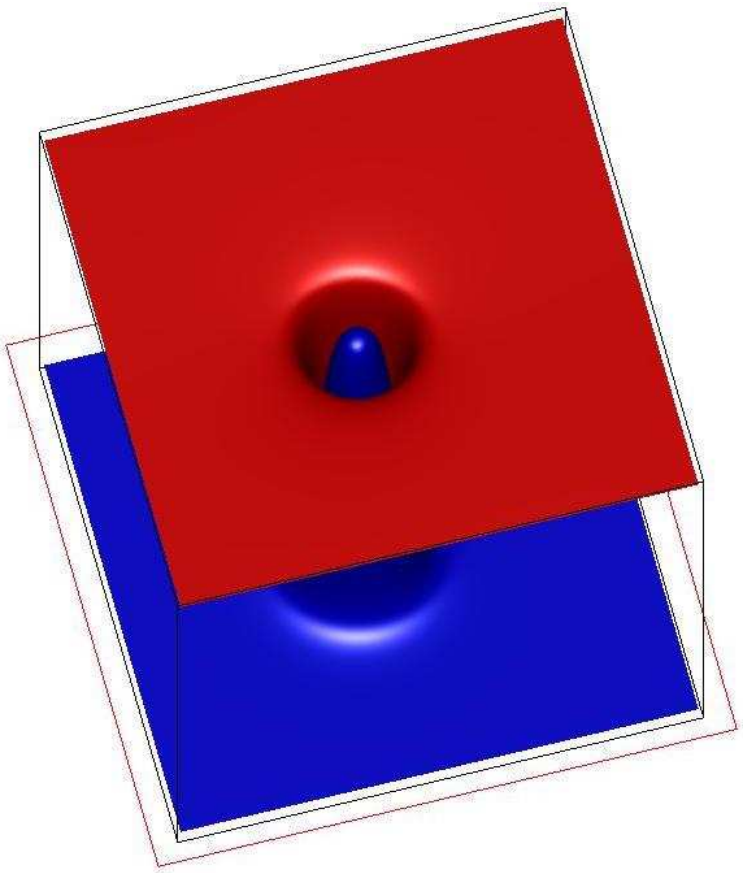

Figure 3.7. From a simulation of a long prism shaped superconductor as described in Fig. 3.2. A vortex in the energetically favorable condensate (red) suppresses the order parameter enabling the less favored condensate (blue) to exist in the vortex core.

In the case where multiple order parameters coexist, the bi-quadratic term will provide either a local attractive or repulsive force between vortices in different condensates depending on the sign of the term.

3.10 The Josephson term

A possible rationalization for the bi-linear Josephson term, $\sigma_{\nu\mu}\Psi_\nu\Psi_\mu^*$, could be hopping between condensates. The two gap superconductors such as MgB_2 may be possible candidates. The complex phase of the coefficient $\sigma_{\nu\mu}$ will only effect the preferred relative phase of the order parameters, so I will assume that $\sigma_{\nu\mu} \leq 0$ and real, such that matching phases minimize the energy.

The Josephson term causes the symmetry for all bi-linear coupled condensates to be broken with the formation of the first condensate. Also, the Josephson term produces a much stronger coupling between condensates than either the $\vec{A}$ field or the bi-quadratic term. For this reason, it is difficult to determine if a superconductor actually has two condensates, or one condensate with two gaps. For clarity, I will define a two order parameter superconductor to be one where both condensates can exist when the Josephson term is frustrated.

The strength of the coupling of the Josephson term can be illustrated by considering the case were each order parameter contains a single vortex which are separated by many coherence lengths. See Fig. 3.8. All Josephson energy iso-curves pass through the center of the vortices. The shape of each iso-curve is fixed, but the overall scale grows

linearly with the separation, r, of the vortices. The energy will increase as r^2 since it is proportional to the area, and will quickly exceed the short range bi-quadratic energies and long range logarithmic $\vec{A}$ field coupling.

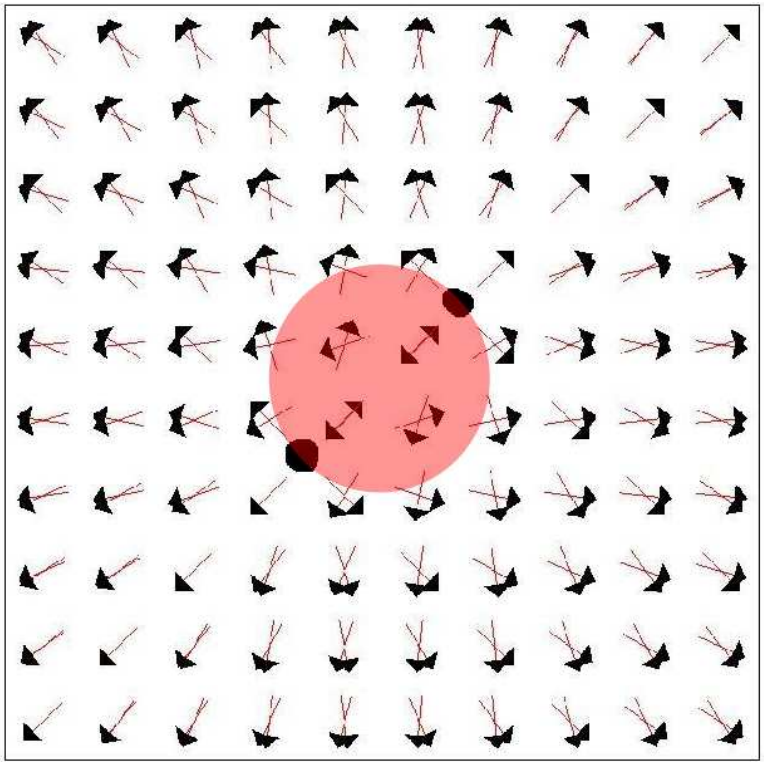

Figure 3.8. The arrows represent the phase of two condensates, each with a single vortex. The vortices are off set from each other to illustrate the effect of relative order parameter phases. The energy associated with the Josephson coupling is proportional to minus the cosine of the difference in the phases. The line between the vortices shows the maximum phase difference and therefore the highest energy density. The curve where the energy contribution is zero forms a circle with the vortex centers on the perimeter.

The preceding argument assumed no charge transfer between condensates. This would certainly be true for the theoretical electron and proton condensates of hydrogen. If it is assumed that some charge transfer does occur, such as a Josephson hopping current

$$J_{hopping} \propto |\Psi_1||\Psi_2| sin(\theta_2 - \theta_1) \tag{3.36}$$

the situation changes considerably. The flow of current between condensates will provide a mechanism by which the phase frustration can be reduced. Figure 3.9 is a three dimensional simulation of a two order parameter block of superconductor. The phase of both condensates is roughly equal throughout the simulation except in the space between the vortices indicated by the thin red "J-wall". Following a path around the blue vortex but not the gold one, one expects the phase of the blue condensate to go through 2π, while the gold condensate will have a phase change of zero. When the phase integration is performed, one finds that both condensates collect a phase change of approximately π in the region that excludes area near the J-wall. In the region between the vortices, the blue condensate will pick up an additional phase of π while the gold condensate will pick up an canceling phase of $-\pi$. The energy associated with the Josephson term is now confined to the J-wall (whose area is proportional to r). The energy associated with the separation of the vortices will be proportional to r.

Well outside the vortex cores and the J-wall, the net current is zero. Since the phases of the condensates are equal, the individual components of the current must also be zero. Well outside the vortex cores but within the J-wall, the net current is still zero, but the components will have equal and opposite currents.

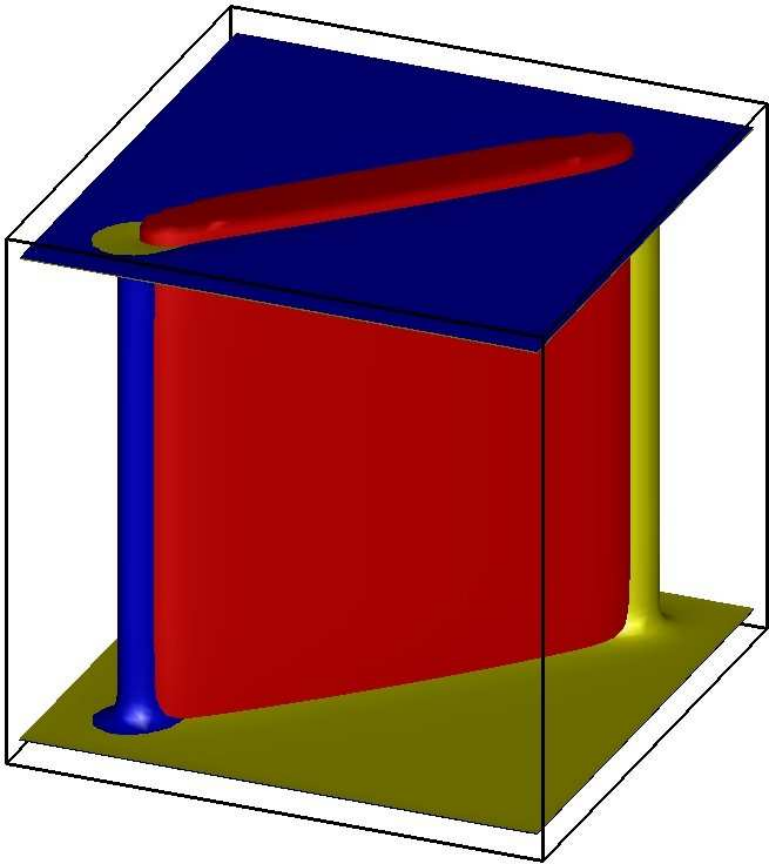

Figure 3.9. This figure is from a 3 dimensional simulation of a two order parameter superconductor with a Josephson coupling term. The iso-surface of the order parameters in gold and blue show a single vortex each. The thin red wall of phase frustration or "J-wall" is an iso-surface of the Josephson energy corresponding to a value of zero. Without inter-condensate currents, this iso-surface would have a circular cross section. See Fig. 3.8.

3.11 J-wall excitations

In the previous section, the J-wall was bordered by either a vortex or the edge of the superconductor. It is also topologically possible for J-wall excitations to exist as closed surfaces. For example consider a spherically symmetric case where both condensates order parameters are real and positive at the origin. At some distance which is several coherence lengths from the origin, one order parameter goes through a phase change of π while the other goes through a phase change of $-\pi$. Outside the region where the phases are changing, each order parameter has a phase that is real and negative. This J-wall forms a sphere with energy proportional to its surface area.

The surface of a J-wall is directed since each condensate flows in definite direction. For convention, assume that the positive direction for a J-wall is the direction that adds π to θ_1. Two oppositely oriented J-walls will experience a short range attraction and will annihilate each other. Two J-walls oriented in same direction will experience a short range repulsion.

Since the J-walls do not couple to the magnetic field, they will be difficult to induce or detect in any material in which multiple condensates are suspected. One possibility for inducing J-walls would be to preferentially drive a tunneling current into only one condensate causing a phase slip between the condensates. It is not clear how to detect when this occurs however.

It may be possible to detect a phase transition where thermally induced J-walls freeze out. The lowest J-Wall excitations would have a finite energy since the length scale

of the smallest J-wall excitation must be on the order of the coherence length. Below this length scale, the order parameters could not make a full rotation of $|\pi|$. Excitations on this scale are not disallowed, but they would tend to be spherical and have an energy that is proportional to their volume. Above this minimum energy, the number of configurations (states) per energy level becomes large since it is not longer limited to being spherical and the energy is proportional to the area. If the low energy excitations are ignored, the sudden rise in density of states at a finite energy and domain wall like behavior gives rise to the Potts model like behavior[80][81].

3.12 Not any knots

There has been interest in knots in multi component Bose Einstein models [82] [83]. The structures considered in these papers were beyond what my numerical model could simulate. Small vortex knot components were considered and found to be unstable. See Fig. 3.10 for a couple of attempts. The knot components were intended to use the repulsion of vortices to overcome the tendency of a vortex to minimize its length. Vortex tension was found to be stronger than repulsion causing the vortices to pass through one another.

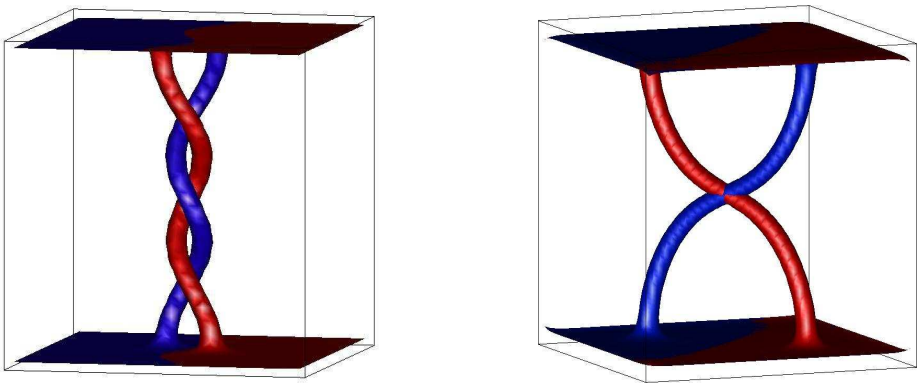

Twist Cross

Figure 3.10. Two attempts at building vortex knots. In all variations of the "twist" attempted, with naturally repelling vortices, the vortices ultimately passed through each other rather than untwisting. With careful positioning, two normally repelling vortices can be attached in a "cross" arrangement to form an unstable bond. When disturbed, the point of intersection will move toward the nearest normal boundary and exit the superconductor.

3.13 Conclusion

I have developed a fast and efficient numerical method for solving the Ginsburg-Landau model of superconductivity in 2 and 3 dimensions. This method included extensive visualization and interaction. The model was used to study the interaction of superconductivity and magnetic fields with particular emphasis on vortex dynamics.

The model was then extended to include multiple condensate order parameters. This extended model was used to study potentially stable vortex knots with negative results. An interesting topological excitation was found associated when a bi-linear Josephson coupling term was included in the simulations.

Chapter 4

Classical Spin Systems

4.1 Introduction

The properties of both 2D square Ising and Edwards-Anderson spin glass model have been studied for many years. The Ising model

$$H = -\sum_{<i,j>} S_i S_j \tag{4.1}$$

with nearest neighbor interactions was solved by Onsanger using transfer matrix methods. The 3D model is considered to fall into a class of NP complete problems that are unsolvable [84], and therefore must be attacked with approximate methods.

The nearest neighbor Edwards-Anderson spin glass energy is

$$H = -\sum_{<i,j>} J_{ij} S_i S_j \tag{4.2}$$

where J_{ij} has some random distribution. The two most common distributions are the bimodal where $J = \pm 1$ and the continuous where J has a distribution that normally is taken to be Gaussian. These models are also unsolved, but a number of methods have been developed to study their properties. The ground state of large systems [85] can be calculated quickly and efficiently making $T = 0$ investigations possible. Sampling methods such as Monti Carlo run into problems due to the slow dynamics below T_c. However improved methods such as tempering [86] have been developed which have enabled progress in 3D investigations [87].

The numerical transfer matrix methods have also been applied to spin glasses [88][89][90], but due to the exponential growth in the memory and simulation time with the width of the system, the size of systems must be limited. As long as Moore's law

continues to hold however, one can expect to add a site to the width of the calculation every couple of years. I have developed efficient algorithms for solving finite size spin glass systems using the transfer matrix method and applied them to Ising an Edwards-Anderson spin systems.

4.2 Transfer matrix applied to spin systems.

Calculating the partition function,

$$Z = \sum_C e^{-E_C \beta} \tag{4.3}$$

where C goes over all configurations, is in principle straight forward. In practice, it is difficult due to the the number of configurations. Each spin in the system doubles the number of terms in the sum giving a total of 2^M configurations M is the number of spins.

The transfer matrix method as applied to spin systems is a method for reducing the number of additions that need to be performed to calculate Z. There is quite a bit of flexibility in defining a transfer matrix, therefore I will describe one implementation while pointing out where degrees of freedom exist. Referring to figure 4.1, the transfer matrix $T(A, B)$ is defined such that it includes all the terms of the partition function sum for all intra-yellow bonds and the bonds between the yellow spins and the spin cuts. The contribution from the bonds between the spins in each cut must be accounted for, but care must be taken not to count them twice. I choose to include the bonds in cut A in $T(A, B)$, but not the bonds in cut B. The bonds in cut B will be accounted for in another transfer matrix.

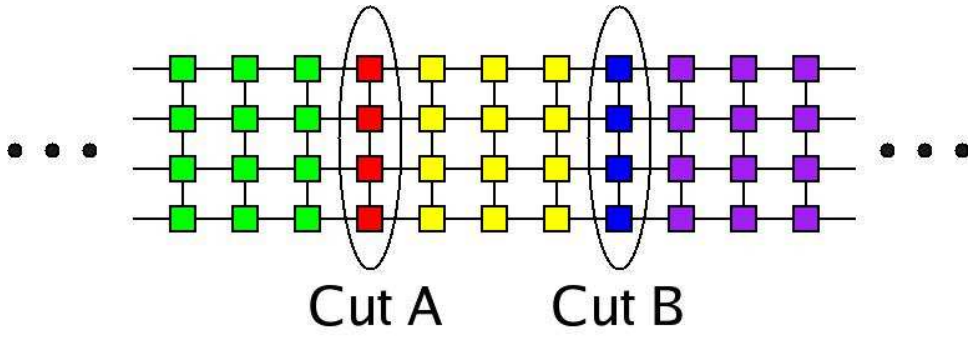

Figure 4.1. The colored squares represent spin sites. The connections between the sites represent bonds. The spins in the cuts must completely separate the spins on either side of the cut such that no direct bond connects sites on one side of the cut to the other side of the cut. Since this system has only nearest neighbor bonds, the cut need only be one spin wide. If however the bonds to next nearest neighbor were also included, the cut would need to be two spins wide.

In this example each cut contains four spins for a total of 16 states. The rows of $T(A, B)$ are indexed by the states of cut A while the columns are indexed by the states of cut B. (The exponential cost has not been completely eliminated but only reduced. This is the major weakness of the transfer matrix method and places practical limits on the cut size.) An entry of the transfer matrix is defined as

$$T_{ij}(A, B) = \sum_{C'} e^{-E_{C'}\beta} \tag{4.4}$$

where the energy only includes the bonds listed above, the sites in cut A are in state i, the sites in cut B are in state j, and the index C' goes over all configurations of the "yellow" sites between the two cuts.

Now assume that I have the matrix $T(A,B)$ and the matrix $T(B,C)$, where C is another cut line further to the right, and I want the matrix $T(A,C)$. Following the standard derivation, first consider the matrix

$$R(j) = T(A,B)|j><j|T(B,C) \tag{4.5}$$

where j selects a single state of B. An entry of B is

$$R_{ik}(j) = \sum_{C'} e^{-E_{C'}\beta} \sum_{C''} e^{-E_{C''}\beta} = \sum_{C'} \sum_{C''} e^{(-E_{C'}-E_{C''})\beta} \tag{4.6}$$

where the index C'' goes over all configuration of sites between cut B and cut C. The nested sum now goes over all configurations of spins between A and C with the spins of cut B in state j. If I then sum over all all states of B, I find I have $T(A,C)$ by definition. Performing the sum gives

$$\begin{aligned} T(A,C) &= \sum_j T(A,B)|j><j|T(B,C) \\ &= T(A,B) \sum_j |j><j|T(B,C) \\ &= T(A,B)T(B,C) \end{aligned} \tag{4.7}$$

which is just simple matrix multiplication.

If the system is open on the ends, the last transfer matrix will need to include the energy for the bonds in the final cut. The partition function is found by summing over all the combined configurations of the starting cut and the ending cut. In term of the final matrix, this becomes

$$Z = \sum_i \sum_j T_{ij}(Start, End) =< \Omega|T(Start, End)|\Omega > \tag{4.8}$$

where $|\Omega>$ is a vector of all 1s.

For periodic boundary conditions, the starting and ending cut are the same and no special handling of the last matrix is necessary. After the final transfer matrix multiplication, only the diagonal terms contribute. The partition function in this case is just given by

$$Z = \sum_i T_{ii}(Start, Start) = Tr[T(Start, Start)] \tag{4.9}$$

It is customary to define the incremental transfer matrix to have a step of one row with no intervening sites. This is cheaper since calculating all the intervening "yellow" spins becomes unnecessary. The original cost went as 2^M. The cost of the transfer matrix goes as

$$2^{N*3} \times L \tag{4.10}$$

Where N width of the cut and L is the length of the system.

4.3 One spin at a time

One degree of freedom in defining the transfer matrix (not mentioned in the previous section) is how the cuts are defined. There is no requirement that the cuts go straight across or that they are non-overlapping. Referring to figure 4.2, the transfer matrix is defined such that only one site is added and one site is removed. The transfer matrix still needs to include all configurations for each cut, but now the cuts are not longer independent. Any entry in the new $T(A, B)$ that conflicts with the shared sites

must be zero. (I have not been able to find a reference of this method of transfer matrix calculation, bit it seems likely to have been done before. The performance matches 2^N best case perfromance mentioned by A. P. Young)

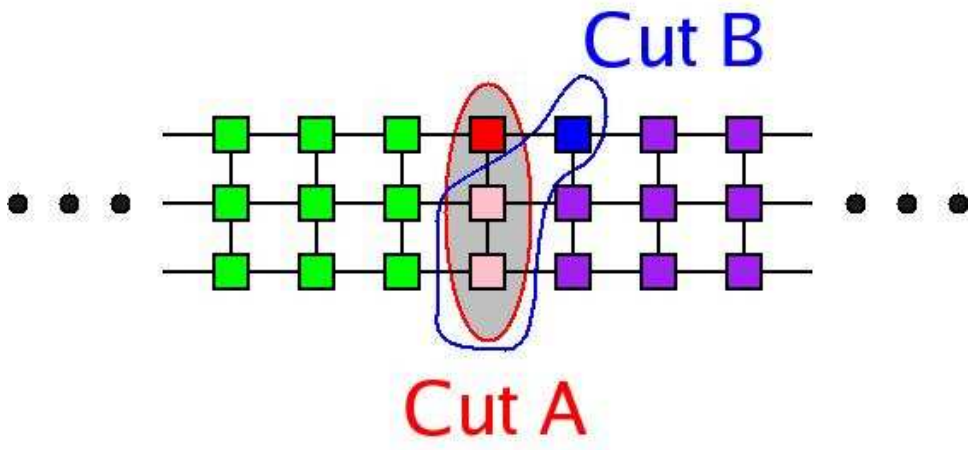

Figure 4.2. The colored squares represent spin sites. The connections between the sites represent bonds. The spin cuts in this case overlap. The red site is unique to cut A, the blue site is unique to cut B, and the pink sites are shared. Both sites meet the bond cut requirement between the green and purple sites.

The new matrix is defined as: (1)the bonds used to calculate $T(A, B)$ are only the ones that connect to the "Red" site. (2)The configurations of the cut are indexed as a binary number where and up spin is a one and a down spin is a zero. (3)The most most significant bit of cut A is the "Red" site.(4)The least significant bit of cut B is the "Blue" site. Assuming no external field, the new one step transfer matrix is

$$T(A,B) = \begin{pmatrix} a & b & 0 & 0 & 0 & 0 & 0 & 0 \\ 0 & 0 & c & d & 0 & 0 & 0 & 0 \\ 0 & 0 & 0 & 0 & e & f & 0 & 0 \\ 0 & 0 & 0 & 0 & 0 & 0 & g & h \\ h & g & 0 & 0 & 0 & 0 & 0 & 0 \\ 0 & 0 & f & e & 0 & 0 & 0 & 0 \\ 0 & 0 & 0 & 0 & d & c & 0 & 0 \\ 0 & 0 & 0 & 0 & 0 & 0 & b & a \end{pmatrix} \tag{4.11}$$

where $a - h$ are Boltzmann terms based on the bond energies. Because of the bonds chosen and the ordering of states, there is a symmetry associated with inversion of all spins that becomes obvious. This symmetry will cause the eigen vectors to be either odd or even. Since all non-zero entries must be positive, one would expect an even eigen vector to always have the largest eigen value. Long range order however requires that the largest odd and even eigen vector become degenerate. This paradox is resolved by noting that long range order does not occur in systems with finite width.

This overlapping of spin cuts turns out to be a big win in the cost of calculations.

The cost of using this sparse transfer matrix to calculate Z goes as

$$2^{N*2} \times L \times N \tag{4.12}$$

Note the exponent associated with the matrix multiplications has been decreased by N with only an additional scaling term of N. This may not seem like a lot, but this can be a factor of several thousand when N starts getting big.

So far, I have only considered calculating the partition function completely. When the system being considered lacks long range order, as one dimensional systems do, it may be acceptable to calculate only a few columns of the final transfer matrix [90]. This is equivalent to limiting the number of starting and stopping configurations. When this is done, the cost of the partition function calculation goes as

$$2^N \times L \times N \times W \tag{4.13}$$

where W is the number of rows of the transfer matrix calculated.

As noted above, the eigen vectors of the one step transfer matrix can separated into even and odd sets. The transfer matrix does not mix the two sets. This creates the possibility of calculating the even an odd parts of the transfer matrix product separately. The odd transfer matrix becomes

$$T_{odd}(A,B) = \begin{pmatrix} a & b & 0 & 0 \\ 0 & 0 & c & d \\ 0 & 0 & -f & -e \\ -h & -g & 0 & 0 \end{pmatrix} \tag{4.14}$$

where $T_{even}(A, B)$ would differ only in that all entries would be positive. This optimization cuts the cost of partition function calculation in half. This optimization does not work with any applied field that breaks inversion symmetry, therefore I have not used this optimization in calculations.

4.4 Finite T computations

In the algorithm that performs the calculation, none of the transfer matrices are ever actually stored. The heart of the algorithm is a subroutine that takes as input a vector of size 2^N "real" floating point values, the bond strength and Zeeman splitting energy. It performs the matrix multiplication and returns the result in another 2^N size vector. To calculate a column of the transfer matrix, the algorithm starts with a unit vector that represents a single configuration of the initial cut, then the subroutine is called once for each spin with the appropriate bonds. This can be written as

$$|T_j >= \prod_i T(i)|j > \tag{4.15}$$

where $|T_j >$ is a column vector representing column j of the transfer matrix product. If the full calculation is desired, this is repeated for each configuration in the initial cut.

The number of spins in the spin cut is limited by computation time and computer memory. For example, a cut of 26 spins consumes one giga-byte of memory and takes about 1 second to perform a matrix multiplication on a relative modern computer (2 giga-Hertz and 2 giga-byte of DRAM). For each spin removed from the cut, the memory and time required to perform a single vector update is cut by half.

The temperature range to which this method can be applied is limited by the accuracy of the numerical representation of real numbers. The magnitude of the entries in the one step transfer matrix for the ± 1 model range from $\sim exp(-1/T)$ to $\sim exp(1/T)$ which puts the absolute range of the terms in the partition function sum to be $\sim exp(\pm M/T)$. As T gets small, the terms closer to $exp(+M/T)$ will dominate.

The lower bound in T is determined by the observable that is being calculated. For example, the calculation of entropy

$$S = ln(Z) + \frac{T}{Z}\frac{dZ}{dT} \tag{4.16}$$

involves a single derivative. Finite difference is the obvious choice for calculating derivatives, unfortunately this involves subtracting two large numbers to produce a small number greatly reduces the usable number of bits of precision. Specific heat,

$$Cv = 2\frac{T}{Z^2}\frac{dZ}{dT} + \frac{T^2}{Z}\frac{d^2Z}{dT^2} \tag{4.17}$$

requires a second derivative which requires performing the subtraction twice. The specific heat calculation on small systems ,$N = 10$ and $L = 100$, seem to be valid down to $T \approx .5$ in units of J. Fortunately this is below the transition temperatures for both ordered and glassy spin systems.

4.5 Partition function polynomial and $T = 0$ calculations

Another way to view the partition function is to think of it as a polynomial

$$Z = \sum_i A_i e^{-E_i\beta} \tag{4.18}$$

where E_i is the ith energy above the ground state. A_i is the degeneracy of ith energy level. In order to put the degeneracy on the same footing as $E\beta$, assume $a_i = ln(A_i)$. The partition function becomes

$$Z = \sum_i e^{(a_i - E_i\beta)}. \tag{4.19}$$

For systems such as the ferromagnetic, antiferromagnetic or ± 1 models, the number of terms will be on the order of the number of spins in the system. The coefficients a_i is the log of the density of states. There have been some attempts to calculate this polynomial for small systems using non-transfer matrix methods [91][92] and an interesting truncated transfer matrix method by Morgenstern and Binder[89]

Calculating the polynomial is conceptually simple if one assumes a polynomial data type that includes the operations of poly-add and poly-scale. Poly-add adds two polynomials to produce a new polynomial. Poly scale multiplies a polynomial by $e^{(a-E\beta)}$. It is also useful to include a clipping option to only keep a fixed number of the lowest energy terms. This new data type replaces the real data type in the algorithm described above. This method is not without its cost however. It takes on the order of six minutes to calculate the full polynomial for a 10 by 10 spin system with this new method where it takes only 3.5 seconds to perform a real calculation for a single T. On the other hand it only takes 8 seconds to calculate the ground state term.

There are several advantages of this method over the "real" method. The most obvious being that once the complete polynomial has been calculated, the partition function is known for all temperatures. The $T = 0$ entropy is given by the log of the degeneracy

of the ground state and approaches the approaches the published bulk value[101],0.078. The fact the Z becomes very large can easily be dealt with by factoring out the largest term

$$Z = e^{(a_x - E_x\beta)} \sum_i e^{(a_i - E_i\beta - (a_x - E_x\beta))}. \tag{4.20}$$

where the xth term is the largest. Each term in the sum is now less than or equal to one, and the large exponential factored out will cancel when an observable is calculated.

4.6 2D Ising phase transition

The 2D Ising phase ferromagnetic phase transition has been solved and is well understood, but it still can be enlightening to consider this case however.

As mentioned before, the largest contribution to the partition function comes from the term with the largest value of $(a_x - E_x\beta)$. For large systems and finite T, there will be many samples around the largest term that also contribute. In this case, it is reasonable to consider the case where a is a continuous function of E. The partition function then becomes

$$Z = \sum_i e^{(a_i - E_i\beta)} \approx \frac{1}{4} \int dE e^{(a(E) - E\beta)} \tag{4.21}$$

where the 1/4 scaling is required because the discrete energy levels occur in steps of four (in units of J). The function $a(E)$ can be thought of as a log of the density of states. The value of E where $(a(E) - E\beta)$ is maximum for a given temperature is found by the

standard method

$$\frac{d}{dE}(a(E) - E\beta) = \frac{da(E)}{dE} - \beta = 0. \tag{4.22}$$

Solving for the inverse temperature gives

$$\beta = \frac{da(E)}{dE} \tag{4.23}$$

where $T = 1/\beta$. As long as the second derivative of $a(E)$ is less than zero, to first approximation the energies around the maximum will contribute to observable calculations with a Gaussian weighting.

Figure 4.3 is a graph of $a(E)$ for a 12 by 70 site ferromagnetic Ising system. For a system with a smooth, convex $a(E)$, the specific heat can be approximated by

$$Cv \approx \frac{-\left(\frac{da(E)}{dE}\right)^2}{\frac{d^2a(E)}{dE^2}} \approx -\left(T^2\frac{d^2a(E)}{dE^2}\right)^{-1}. \tag{4.24}$$

Near the center of the graph, one can see how the curvature approaches zero. This will cause the specific heat to diverge indicating a second order phase transition.

The specific heat calculated using equation 4.17 for a range of system configurations is shown in figure 4.4.

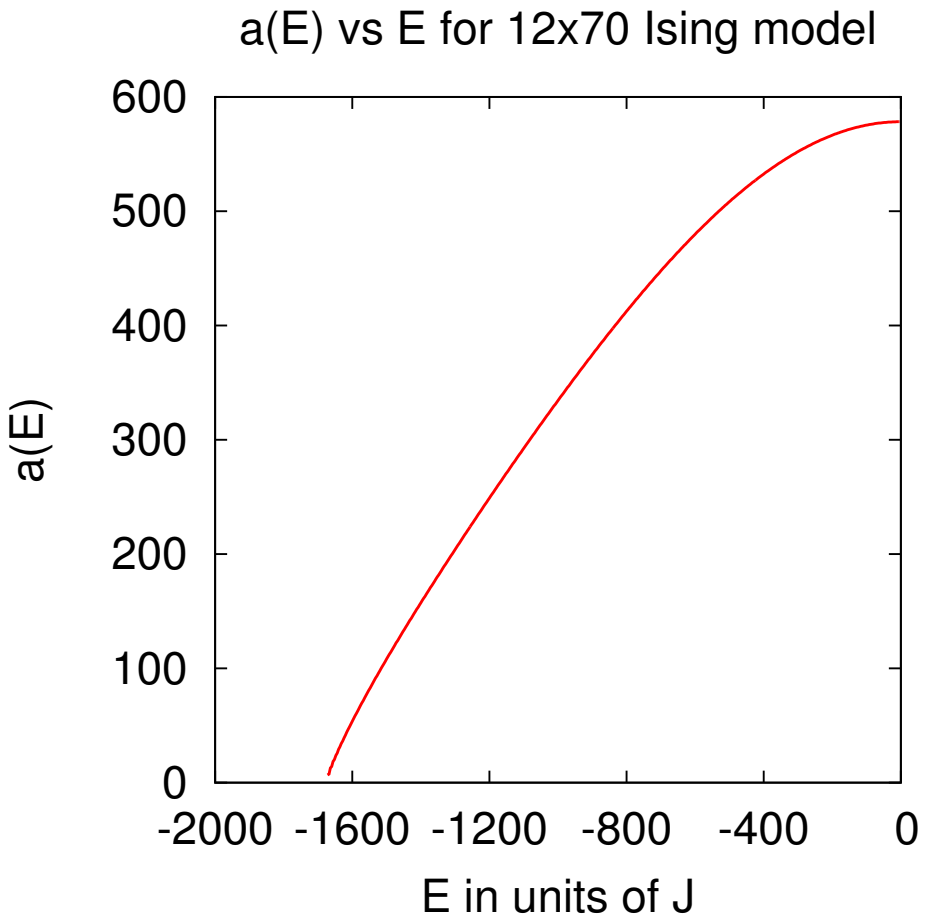

Figure 4.3. The log of the density of states (E) for a 12 by 70 ferromagnetic Ising model. The density of states is symmetric around $E = 0$ so only the states corresponding to positive temperatures are calculated. The curvature flatting is an indication of a second order phase transition.

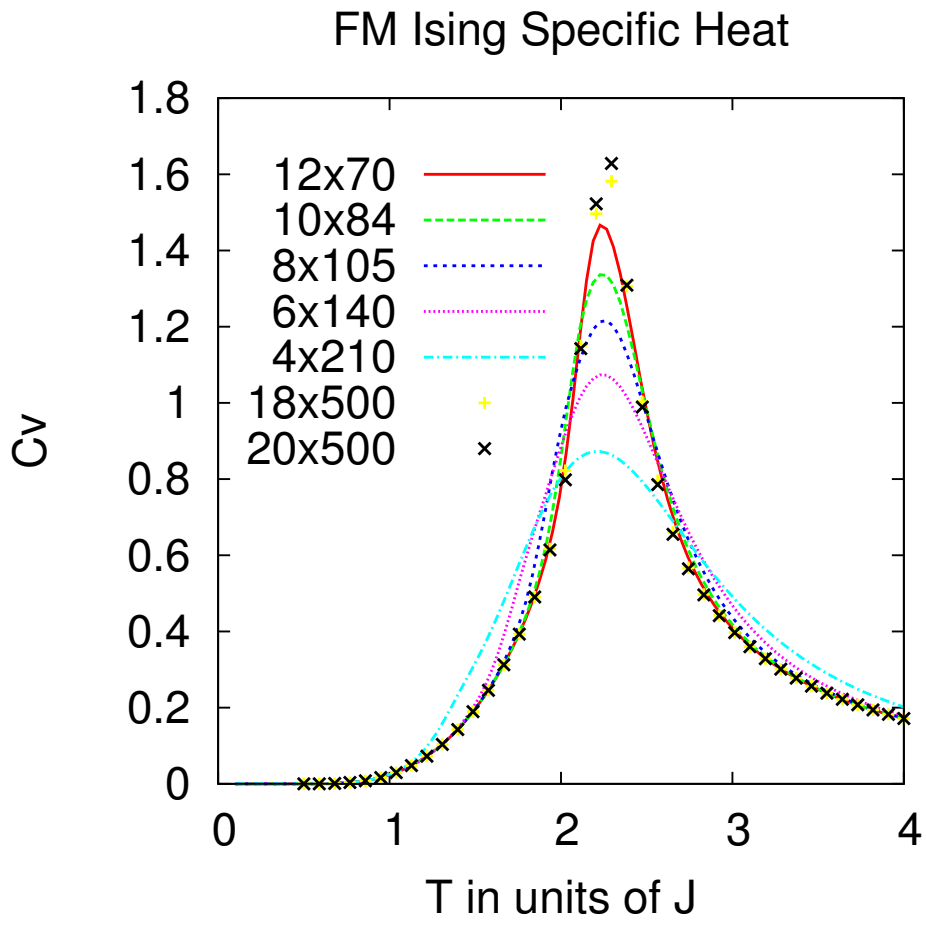

Figure 4.4. The specific heat for a range of system configurations showing approaching divergence as the geometry of the system goes from one dimensional to two dimensional. The systems represented by lines were produced from full partition function polynomial calculations. The systems represented by points were produced from real calculations of one row from the transfer matrix.

4.7 Spin Glass

Glassy systems in general are characterized by taking a long time to reach thermodynamic equilibrium, and in most cases this time becomes infinite. This is is generally attributed to the presence of energy barriers between local energy minimum which prevent the thermal excited exploration of configuration space.

4.8 Trapping local energy minimum

An example without quenched disorder, consider a magnetic that is modeled by the classical, rectangular, two dimensional, ferromagnetic Ising model with nearest neighbor interactions. The Hamiltonian is

$$H = -\sum_{<i,j>} J_{ij} S_i S_j \tag{4.25}$$

where the sum goes over all nearest neighbors, $J_{ij} = 1$, and $S_\alpha = \pm 1$. The ground state is known to be all $S_\alpha = 1$ or all $S_\alpha = -1$. If this system is suddenly quenched from a temperature well above T_c to a temperature well below T_c , one expects to find that the magnetization is defined by

$$m = \frac{1}{M} \sum_i S_i =< S > \tag{4.26}$$

where M is the total number of spins, to approach ± 1. If one assumes one spin at a time transitions and the absence of system spanning domain walls, it is possible go from a disordered state to one of the ground states making only transitions which reduce the

total energy or are energetically neutral. Therefore there is no energy barrier to reaching the ground state.

To add quenched disorder, one only needs to periodically reduce the interaction in rows and columns of connections to create squares of sites with uniform intra-square interactions of $J = 1$, connected by inter-square interactions of $J' = 1 - \delta$. As long as $0 < \delta < 1$, the ground state does not change. When this system is quenched, these weakened connections create energy barriers to domain wall motion. This can be demonstrated by considering the a square with $m = -1$ that is surrounded by squares with $m = 1$. In order to switch the center square, the system will need to overcome a minimum energy barrier of $\delta/2$ times the number of spins on the parameter of the square. This minimum energy barrier is crossed by moving a diagonal phase boundary from corner to corner.

4.9 Frustration

The other key feature of spin glasses is frustration. A closed path of bonds is considered frustrated if path product

$$F = \prod_{ij} J_{ij} \tag{4.27}$$

is negative. The product is over all connections in the path. In any frustrated path, there is at least one frustrated bond (not in its low energy state). In the two dimensional, square, nearest neighbor, Edwards-Anderson model the minimum structurally frustrated path is the 4 site square or F-placket. Structurally unfrustrated plackets will be refereed to as U-plackets [93]. The Edwards-Anderson model is like the Ising model except that

$J_{ij} = \pm 1$ with some random distribution.

The F-placket has some properties similar to the winding number associated with vortices in type II superconductors. A positive sign of path product, F, indicates that an even number of F-plackets are enclosed while a negative sign indicates that an odd number are enclosed. This can easily be demonstrated by starting with a arbitrary path where F has a definite sign. When the path is increased to enclose another placket, one to three edges are removed and one to three edges are added such that the total is 4 edges. If the sign of F changes, then the sign of the path product for the edges removed must be different from the sign of the path product of edges added. Therefore the path product for the added placket must be negative indicating it is an F-placket. To complete the argument, start with a single placket and add packets to for any arbitrary path.

This placket parity forces F-plackets to form pairs connected by a path of doubly frustrated U-plackets. While U-plackets are not structurally frustrated, they still can have an even number of frustrated bonds. Figure 4.5 illustrates the ground state of a system containing four F-plackets. The energy of the system is minimum when the number of doubly frustrated U-plackets needed to connect all F-plackets in the system is minimized.

This pair formation is also responsible for the presence of quenched disorder in Edwards-Anderson models. If the pairing had instead been horizontal in figure 4.5 such that the upper two F-plackets were paired and the lower two were paired, there would be a energy barrier that would have to be crossed to transition to the ground state.

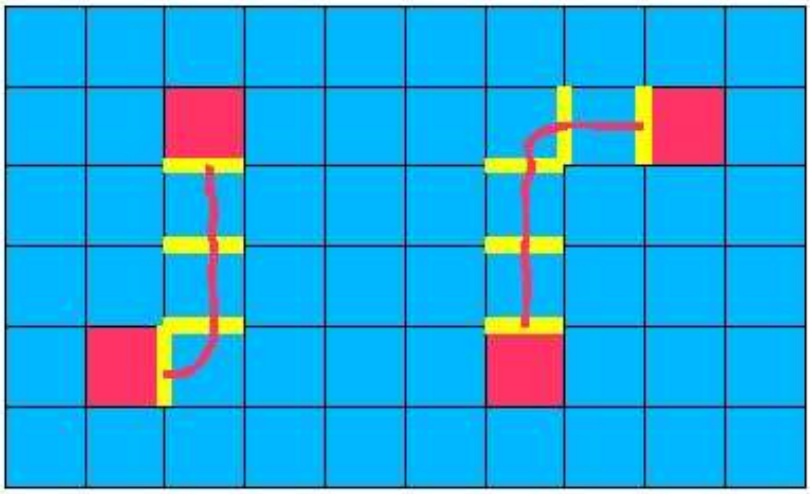

Figure 4.5. A graphical representation of one of the ground states of a spin system containing four structurally frustrated F-plackets. The red squares represent F-plackets. The blue squares represent structurally unfrustrated U-plackets. The black lines are unfrustrated bonds. The yellow bars are frustrated bonds. In any configuration of spins, there will always be a path that starts in a F-placket crosses only frustrated bonds, and ends in an F-placket (or in the case of open boundaries, exits that system). The total taxi cab length of these paths will be minimized in the ground state.

4.10 2D ± 1 glass simulations

The spin glass transition is not an equilibrium transition like the Ising ferromagnetic transition. It is instead a transition from a paramagnetic state to a quenched state where the system gets trapped in a local energy minimum. Below the transition temperature T_G, the system dynamics become very slow. The dynamics generally considered to become logarithmic in time reflecting a $1/f$ distribution of energy barriers. The number of energy minima grows exponentially with the size of the system making sampling methods such as Monti Carlo difficult. Multi-temperature methods have shown some success [].

The transfer matrix method avoids the local trapping problems by considering all possible configurations. So by design, it captures the equilibrium statistics that would only be accessible as time approaches infinity. The density of states function for a ± 1 system does not show any flattening that would indicate a phase transition. See figure 4.6. The The function $a(E)$ is much closer to an ellipse. As expected, the equilibrium specific heat does not show a divergent behavior. See figure 4.7

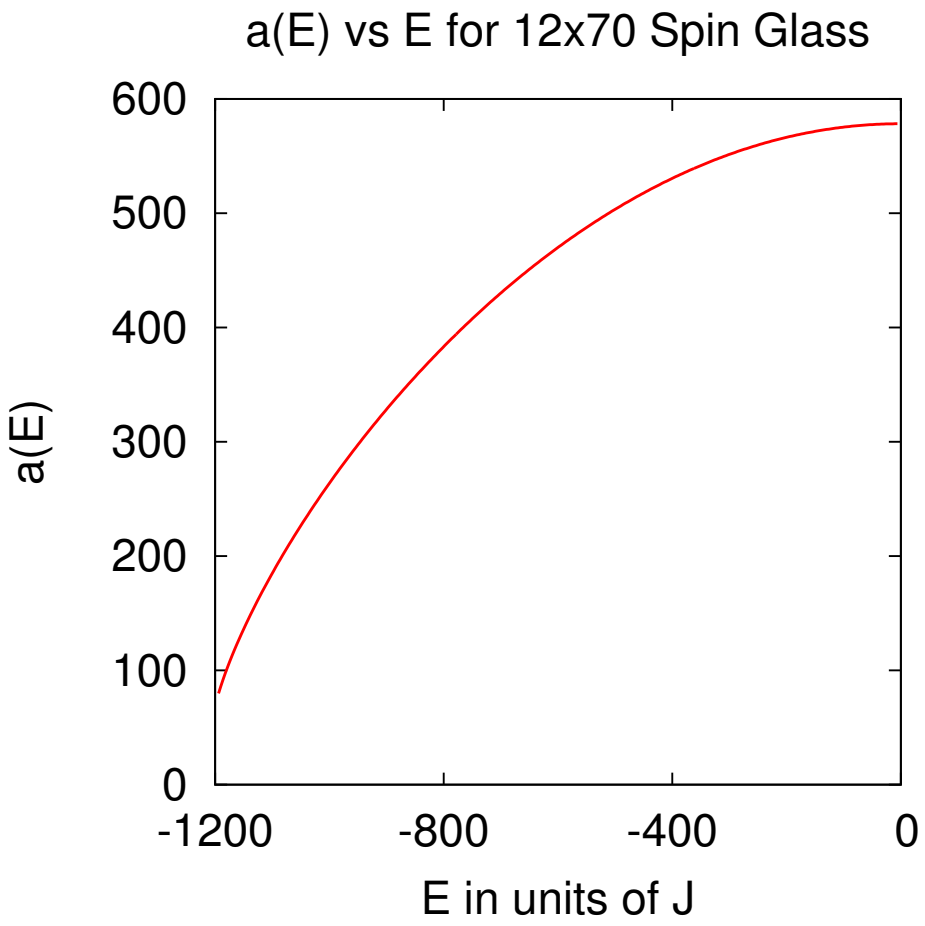

Figure 4.6. The log of the density of states (E) for a 12 by 70 ± 1 spin glass model. The density of states is symmetric around $E = 0$ so only the states corresponding to positive temperatures are calculated. The graph is quite elliptical with no flat area associated with a phase transition.

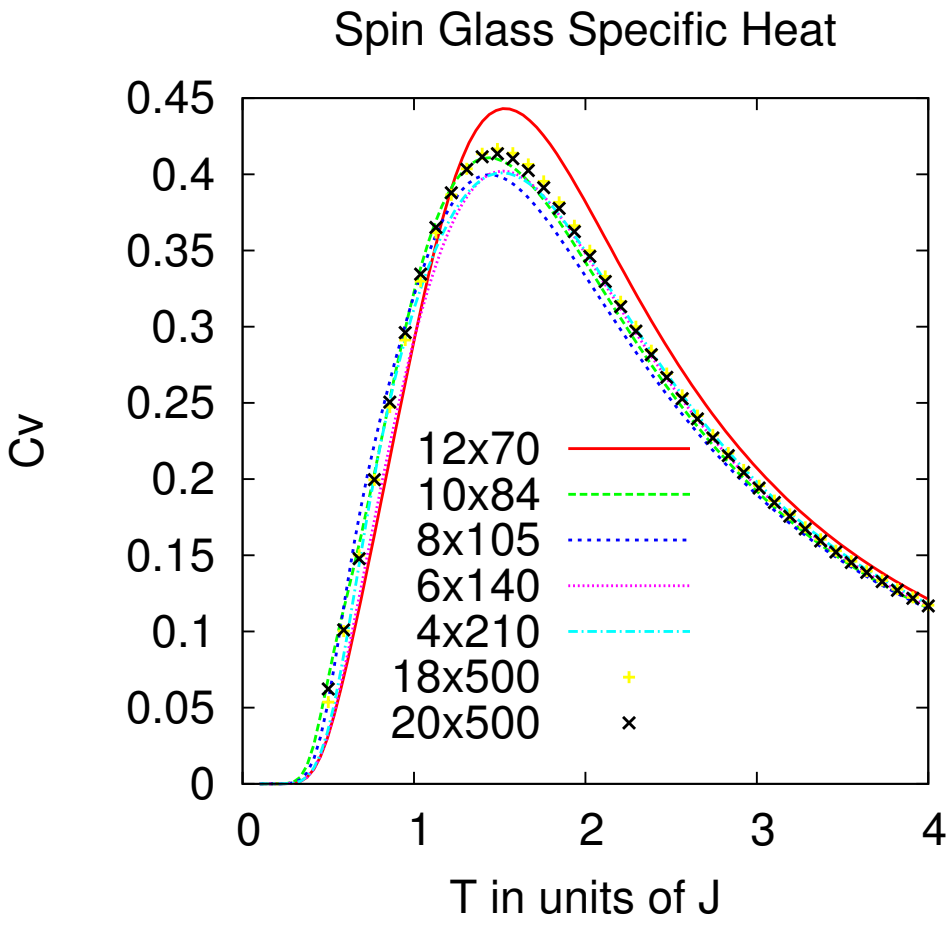

Figure 4.7. The specific heat for a range of system configurations shows no divergence behavior. The variations between simulations seems to be due more to the the particular disorder in the bonds than the system size. The systems represented by lines were produced from full partition function polynomial calculations. The systems represented by points were produced from real calculations of one row from the transfer matrix.

4.11 2D continuous bond distribution glass simulation

When the bonds in a spin glass have a continuous distribution, each state has a degeneracy of 2. This causes the partition function polynomial to have 2^{M-1} unique terms making a complete calculation intractable. One possibility to get around this limitation is to use energy binning to force degeneracy for nearly degenerate states. This has shown some promise, but I have yet to quantify the error.

The lack of degeneracy creates the possibility of calculating exact ground and excited states. By fixing one spin in the system, each term of the polynomial is associated with a unique configuration which can be tracked. The ground state has been verified using the Spin Server provided online by the Institut fr Informatik. The ground state and first three excited states for a 10 by 10 spin system with Gaussian bond distribution is shown below. In the ground state, up spins are indicated by "+" and down spins by a "−". In the excited states, an "=" sign indicates a ground state matching spin and an "∗" indicates a flipped spin. The large number of flipped spins in the third excited state illustrates how a local minimum can be a large distance (as measured in number of differing spins) from the ground state.

Ground	$E = 0.048$	$E = 0.124$	$E = 0.163$
$-+--+----+$	==========	==========	==******==
$--++-----+$	==========	==========	==*******=
$-+++--+--+$	==**======	==========	====*****=
$+++++++-++$	==========	==========	==********
$+++-------++$	==========	==========	==********
$+--+--++-+$	==========	==**======	====*****=
$-+---+---+$	==========	==**======	====**====
$++-+-++-++$	==========	==========	==========
$---+-+++++$	==========	==========	==========
$++-+----+--$	==========	==========	=====***==

Another way to analyze is to analyze the behavior is to consider the spin-spin correlation verses distance at finite temperatures. As the transfer matrix product is created by incorporating more spins through matrix multiplication

$$T_{running} = \prod_{s=0-i} T_s \tag{4.28}$$

the current product matrix quickly assumes a very singular form

$$T_{running} = \lambda_{Odd}|Odd_R >< Odd_L|\lambda_{Even}|Even_R >< Even_L| \tag{4.29}$$

with all other eigenvalues becoming tiny. At $T = 0$ it is expected that $\lambda Even \sim \lambda Odd$ as the number of spins grows large indicating long range order. At $T > T_{SG}$ it is expected that

$\lambda_{Even} >> \lambda_{Odd}$ indicating no long range order. Figure 4.8 illustrates how the eigenvalues change with distance along a long 18 spin wide strip. The quantity graphed,

$$\Gamma = log\left(\frac{\lambda_{Odd}}{sqrt\lambda_{Odd}^2 + \lambda_{Even}^2}\right) \tag{4.30}$$

indicates how correlated a states at the start of the strip are to the states at the end of the strip. At the highest temperature, $T = 0.35$, Γ shows a noisy but steady decline representing an exponential loss of correlation. Between $T = 0.25$ and $T = 0.15$, flat portions start appearing representing highly correlated regions. These correlated regions are responsible for the energy barriers that cause the slow spin glass dynamics below T_{SG}. At $T = 0.05$, the graph is mostly flat with a few noisy steps. These steps are caused by low energy excitations that span the width of the strip. At any finite temperature, these excitations will cause the loss of long range order. Domain spanning excitations will exist at some density below any finite energy.

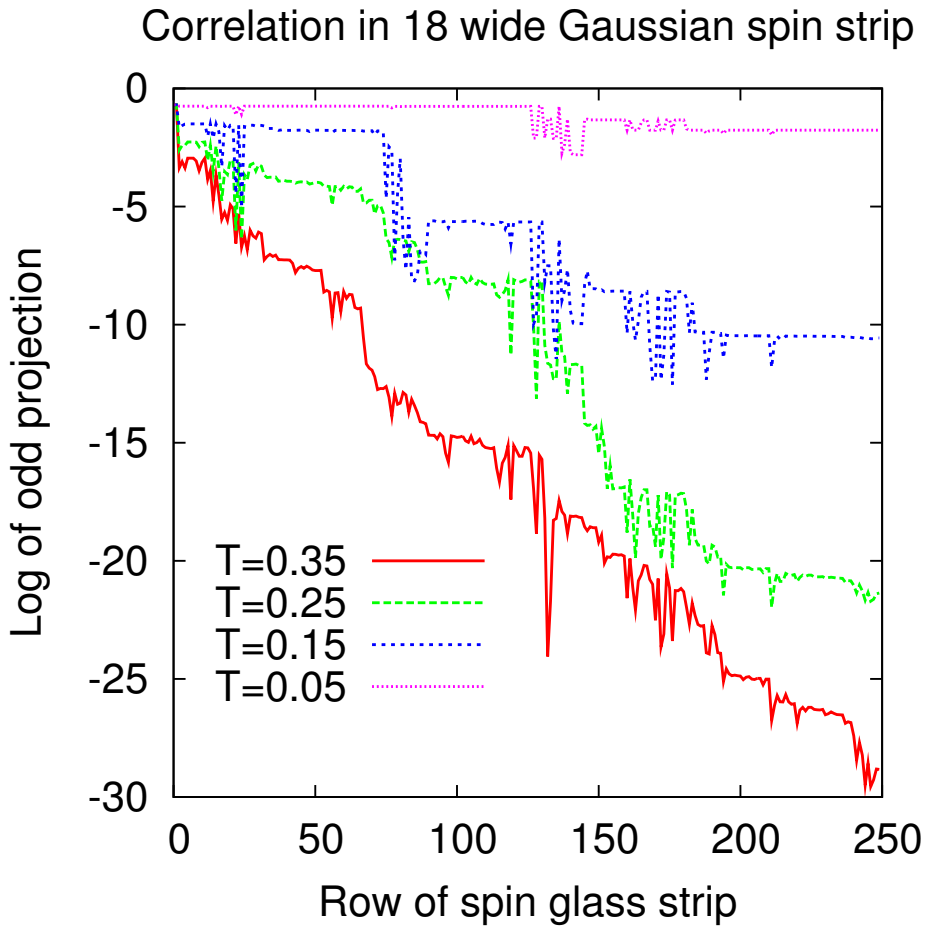

Figure 4.8. This graph indicates how Γ change as a function of the length of an open ended strip and the temperature

4.12 Conclusion

The exponential advancement of computers enables the revisiting of problems from time to time. I have developed transfer matrix algorithms for the calculation of the finite T partition function and the exact polynomial partition function. I have verified these calculations by compairing them against published results.

Bibliography

[1] V. Ginzburg, Sov. Phys. JETP **4**, 153 (1957).

[2] J. Bardeen, L. N. Cooper, and J. R. Schrieffer, Phys. Rev **108**, 1175 (1957).

[3] P. Fulde and R. A. Ferrell, Phys. Rev **135**, A550 (1964).

[4] A. I. Larkin and Y. N. Ovchinnikov, Sov. Phys. JETP. **20**, 762 (1965).

[5] R. Casalbuoni and G. Nardulli, Rev. Mod. Phys. **76**, 263 (2004).

[6] L. N. Bulaevskii, Sov. Phys. JETP **38**, 634 (1974).

[7] M. S. Nam, J. A. Symington, J. Singleton, S. J. Blundell, A. Ardavan, J. A. Perenboom, M. Kurmoo, and P. Day, J. Phys.: Condens. Matter **11**, L477 (1999).

[8] S. Manalo and U. Klein, J. Phys.: Condens. Matter **12**, L471 (2000).

[9] S. Uji, H. Shinagawa, T. Terashima, T. Yakabe, Y. Teral, M. Tokumoto, A. Kobayashi, H. Tanaka, and H. Kobayashi, Nature **410**, 908 (2001).

[10] L. Balicas, J. S. Brooks, K. Storr, S. Uji, M. Tokumoto, H. Tanaka, H. Kobayashi, A. Kobayashi, V. Barzykin, and L. P. Gor'kov, Phys. Rev. Lett. **87**, 067002 (2001).

[11] M. Houzet, A. Buzdin, L. Bulaevskii, and M. Maley, Phys. Rev. Lett. **88**, 227001 (2002).

[12] S. Uji, H. Shinagawa, C. Terakura, T. Yakabe, Y. T. M. Tokumoto, A. Kobayashi, H. Tanaka, and H. Kobayashi, Phys. Rev. B **64**, 024531 (2001).

[13] A. Bianchi, R. Movshovich, C. Capan, P. G. Pagliuso, and J. L. Sarrao, Phys. Rev. Lett. **91**, 187004 (2003).

[14] H. Won, K. Maki, S. Haas, N. Oeschler, F. Weickert, and P. Gegenwart, Phys. Rev. B **69**, 180504 (2004).

[15] V. G. Kogan, P. Miranovi/'c, L. Dobrosavljević-Grujic, W. E. Pickett, and D. K. Cristen, Phys. Rev. Lett. **79**, 741 (1997).

[16] V. G. Kogan, P. Miranovic, L. Dobrosavljevic-Grujic, W. E. Pickett, and D. K. Cristen, Phys. Rev. Lett. **79**, 741 (1997).

[17] S. Graser, T. Dahm, and N. Schopohl, Phys. Rev. B **69**, 014511 (2004).

[18] K. G. Sandeman, G. G. Lonzarich, and A. J. Schofield, Phys. Rev. Lett. **90**, 167005 (2003).

[19] I. I. Mazin, D. J. Singh, and A. Aguayo, cond-mat/0401563 .

[20] M. Uhlarz, C. Pfleiderer, and S. M. Hayden, Phys. Rev. Lett. **93**, 256404 (2004).

[21] N. L. Cooper, Phys. Rev **104**, 1189 (1956).

[22] F. London, *Superfluids* (Wiley, New York, 1950), Vol. 1.

[23] T. V. Duzer and C. Turner, *Principles of Superconductive Devices and Cricuits* (Elsevier, New York, 1981).

[24] A. J. Leggett, Rev. Mod. Phys. **47**, 331 (1975).

[25] A. P. Mackenzie and Y. Maeno, Rev. Mod. Phys. **75**, 657 (2003).

[26] B. J. Powell, J. F. Annett, and B. L. Gyorffy, J. Phys. A **36**, 9289 (2003).

[27] H. Shimahara, Phys. Rev. B. **50**, 12760 (1994).

[28] K. Koepernik and H. Eschrig, Phys. Rev. B **59**, 1743 (1999).

[29] D. J. Singh and I. I. Mazin, Phys. Rev. Lett. **88**, 187004 (2002).

[30] E. A. Yelland, S. M. Hayden, S. J. C. Yates, C. Pfleiderer, M. Uhlarz, R. Vollmer, H. v. Lhneysen, N. R. Bernhoeft, R. P. Smith, S. S. Saxena, and N. Kimura, Phys. Rev. B. **72**, 214523 (2005).

[31] H. Saji, T. Y. ya, and M. Asama, J. Phys. Soc. Jpn. **21**, 255 (1966).

[32] B. T. Matthias, A. L. Giorgi, V. O. Strobing, and J. L. Smith, Phys. Lett. **69**, L441 (1978).

[33] V. C. Rakhecha, G. P. Fletcher, S. K. Singh, J. L. Smith, and B. T. Matthias, Solid State Comm. **33**, 495 (1980).

[34] S. Teacake, H. Asoka, C. Y. Huang, and J. L. Smith, J. Phys. Soc. Jpn. **50**, 2137 (1981).

[35] F. Acker, Z. Fisk, J. L. Smith, and C. Y. Huang, J. Magn. Magn. Mater. **22**, 250 (1981).

[36] P. Monod, I. Felner, G. Ghouteau, and D. Shaltiel, J. Phys. Lett. **41**, L551 (1980).

[37] D. Shaltiel, P. Monod, and L. Felner, J. Phys. Lett. **41,**, L567 (1980).

[38] E. P. Wohlfarth and P. Rhodes, Philos.Mag. **7**, 1817 (1962).

[39] E. P. Wohlfarth, J. Magn. Magn. Mater. **20**, 77 (1980).

[40] F. Acker, R. Huguenin, M. Pelizzone, and J. L. Smith, Phys. Rev. B. **24**, 5404 (1981).

[41] C. J. Shinkel, F. Boer, and B. Hon, J. Phys. F **3**, 1463 (1973).

[42] A. P. J. van Deursen, A. R. de Vroomen, and J. L. Smith, Solid State Comm. **36**, 305 (1980).

[43] G. R. Stewart, B. T. Matthias, A. L. Giorgi, E. G. Szklarz, and J. L. Smith, Solid. State. Comm. **30**, 709 (1979).

[44] G. S. Knapp, F. Y. Fradin, and H. V. Culbert, J. Appl. Phys. **42**, 1341 (1971).

[45] P. G. Mattocks and D. Melville, J. Phys. F: Metal Phys. **8**, 1291 (1978).

[46] M. U. C. Pfleiderer, S. M. Hayden, R. Vollmer, H. v. Lohneysen, N. R. Bernhoeft, and C. G. Lonzarich, Nature **412**, 58 (2001).

[47] G. R. Stewart, J. L. Smith, and B. L. Brandt, Phys. Rev. B. **26**, 3783 (1982).

[48] D. M. Ioshpe, Mod. Phys. Lett. B **5**, 721 (1991).

[49] M. Shimizu, Proc. Phys. Soc. **86**, 147 (1965).

[50] T. Moriya and K. Ueda, Ref. Prof. Phys. **66**, 1299 (2003).

[51] T. Jarlborg, A. J. Freeman, and D. D. Koelling, J. Magn. Magn. Mater. **23**, 291 (1981).

[52] T. Jarlborg and A. J. Freeman, Phys. Rev. B. **22**, 2332 (1980).

[53] R. A. de Groot, D. D. Koelling, and F. M. Mueller, J. Phys. F: Metal Phys. **10**, L235 (1980).

[54] A. Aguayo and D. J. Singh, Phys. Rev. B **66**, 020401 (2002).

[55] A. Aguayo, I. I. Mazin, , and D. J. Singh, Phys. Rev. Lett. **92**, 147201 (2004).

[56] K. Koepernik and H. Eschrig, Phys. Rev. B **59**, 1743 (1999).

[57] J. P. Perdew and Y.Wang, Phys. Rev. B **45**, 13244 (1992).

[58] P. Blaha, K. Schwarz, G. K. H. Madsen, D. Kvasnicka, and J. Luitz, Phys. Rev. B **45**, 13244 (1992).

[59] J. P. Perdew, K. Burke, and M. Ernzerhof, Phys. Rev. Lett. **77**, 3865 (1996).

[60] J. F. Janak, Phys. Rev. B **16**, 255 (1977).

[61] K. Schwarz and P. Mohn, J.Phys. F **14**, L129 (1984).

[62] I. I. Mazin and D. J. Singh, Phys. Rev. B **69**, 020402 (2004).

[63] P. Larson, I. I. Mazin, and D. J. Singh, Phys. Rev. B **69**, 064429 (2004).

[64] T. Moriya and K. Ueda, Rep. Prog. Phys **66**, 1299 (2003).

[65] W. Gerhardt, J. S. Schilling, H. Olijnyk, and J. L. Smith, Phys. Rev. B **21**, 5814 (1983).

[66] W. E. Pickett, Phys. Rev. Lett. **48**, 1548 (1982).

[67] V. Ginzburg, , and L. Landau, Zh. Eksperim. i teor. fiz. **20**, 1064 (1950).

[68] Q. Du, Comput. Math. Appl. **27**, 119 (1994).

[69] A. Dorsey, Phys. Rev. B. **46**, 8376 (1992).

[70] J. A. Abrikosov, Sov. Phys. JETP 6, 1174 (1957).

[71] M. Tinkham, *Introduction to Superconductivity* (Dover, New York, 1975).

[72] S. Tsuda, T. Yokoya, T. Kiss, Y. Takano, K. Togano, H. Kito, H. Ihara, and S. Shin, Phys. Rev. Lett. **87**, 177006 (2001).

[73] F. Giubileo, D. Roditchev, W. Sacks, R. Lamy, D. X. Thanh, , J. Klein, S. Miraglia, D. Fruchart, J. Marcus, and P. Monod, Phys. Rev. Lett. **87**, 177008 (2001).

[74] S. A. Bonev, E. Schwegler, T. Ogitsu, and G. Gali, Nature (2004).

[75] E. Babaev, Phys. Rev. Let. **89**, 67001 (2002).

[76] Q. Du, Mathematics of Computation **67**, 965 (1998).

[77] Z. D. Wang and C. R. Hu, Phys. Rev. B **44**, 11918 (1991).

[78] R. Karamikhova, Nonlinear Analysis Theory, Methods nd Applications **30**, 1893 (1997).

[79] Q. Du, J. of Mat. Phys. **46**, 95109 (2005).

[80] R. B. Potts, Proc. Cambridge Philos. Soc. **48**, 106 (1952).

[81] N. Neinhuis, A. N. Berker, E. K. Riedel, and M. Schick, Phys. Rev. Lett. **43**, 737 (1997).

[82] Y. Duan, X. Zhang, Y. Liu, and L. Zhao, Phys. Rev. B **74**, 144508 (2006).

[83] Y. M. Cho, H. Khim, and P. Zhang, Phys. Rev. A **72**, 063603 (2005).

[84] S. Istrail, Proceedings of the 31st ACM Annual Symposium on the Theory of Computing (2000).

[85] R. G. Palmer and J. Adler, Int. J. Mod. Phys. C **10**, 667 (1999).

[86] E. Marinari and G. Parisi, Europhys. Lett. **19**, 451 (1992).

[87] H. G. Katzgraber, M. Krner, and A. P. Young, cond-mat/0602212 (2006).

[88] D. A. Huse and I. Morgenstern, Phys. Rev. B. **32**, 3032 (1985).

[89] I. Morgenstern and K. Binder, Phys. Rev. B **22**, 288 (1980).

[90] F. D. A. A. Reis, S. L. A. de Queiroz, and R. R. dos Santos, Phys. Rev. B. **60**, 6740 (1999).

[91] L. Saul and M. Kardar, Phys. Rev. E. **48**, 3221 (1993).

[92] A. Galluccio, M. Loebl, and J. Vondrak, Phys. Rev. Lett **64**, 5924 (2000).

[93] Z. F. Zhan, L. W. Lee, and J.-S. Wang, Physica A **285**, 239 (2000).

[94] f. Barahona, R. Maynard, R. Rammal, and J. Uhry, J. Phys. A. **15**, 673 (1982).

[95] T. Sakakibara, T. Tayama, A. Harita, Y. Haga, H. Shishido, R. Settai, and Y. Onuki, Inst. Phys. Jagellonian Univ. Acta Physica Polonica B **34**, 467 (2003).

[96] J. Singleton, J. A. Symington, M.-S. Nam, A. Ardavan, M. Kurmoo, and P. Day, J. Phys.: Condens. Matter **12**, L641 (2000).

[97] S. Manalo and U. Klein, J. Phys.: Cond. Matter **12**, L471 (2000).

[98] H. Shimahara, Journal of the Physical Society of Japan **68**, 3069 (1999).

[99] E. A. Yelland, S. M. Hayden, S. J. C. Yates, C. Pfleiderer, R. V. M. Uhlarz, H. v. Lohneysen, N. R. Bernhoeft, R. P. Smith, S. S. Saxena, and N. Kimura, cont-mat/0502341. .

[100] D. J. Singh, *Planewaves, Pseudopotentials and the LAPW method* (Kluwer Academic, Boston, 1994).

[101] W. E. Pickett, Phys. Rev. B **26**, 1186 (1982).